

A numerical investigation of dynamics, thermodynamics and mixed-layer processes in the Indian Ocean

JULIAN P. MCCREARY, JR.¹, PIJUSH K. KUNDU¹ and ROBERT L. MOLINARI²

¹*Oceanographic Center, Nova University, 8000 N. Ocean Drive, Dania, Florida 33004, USA*

²*Atlantic Oceanographic and Meteorological Laboratory, 4301 Rickenbacker Causeway, Miami, Florida 33149, USA*

Abstract – A 2½-layer, thermodynamic numerical model is used to study the dynamics, thermodynamics and mixed-layer physics of Indian Ocean circulation. A surface mixed layer of temperature T_m is imbedded in the upper layer of the model, and entrainment and detrainment in the mixed layer are determined by wind stirring and surface cooling. There is also detrainment w_d through the base of the upper layer that models subduction. Monthly climatological data, including air temperature T_a and specific humidity q_a , are used to force the model, and model sea surface temperature (SST), T_m , is used to determine the sensible and latent heat fluxes. With a few notable exceptions, our main-run solution compares well with observed current and SST data; this is particularly true for T_m , which typically differs from observed SST by less than 0.5–1.0°C. Our analyses focus on three topics: the relative importance of remote versus local forcing, the thermodynamic processes that determine the model SST field, and the development of meridional circulation cells.

There are a number of examples of remotely forced circulations in our main run. During the spring a northeastward countercurrent flows against the prevailing winds along the Somali coast north of 4°N, and from October through February a southwestward Somali Undercurrent is present from the tip of Somalia to 3°N; both of these flows result in part from forcing during the previous Southwest Monsoon. From March through May there is another southwestward Somali Undercurrent south of 7°N, generated primarily by the propagation of a Rossby wave from the west coast of India. The currents along the west coast of India are either strongly influenced or dominated by remote forcing from the Bay of Bengal throughout the year. A northeastward flow is well established along the east coast of India in March, long before the onset of the Southwest Monsoon; it is remotely forced either by upwelling-favorable, alongshore winds elsewhere within the Bay of Bengal or by negative wind curl in the western Bay. Finally, the Agulhas Current is strengthened considerably in a solution that includes throughflow from the Pacific Ocean.

To investigate the relative importance of thermodynamic processes, we carried out a series of test calculations with various terms dropped from the T_m -equation. There is little effect on T_m when the sensible heat flux is set to zero, or when the solar radiation field is replaced by a spatially smoothed version. When temperature advection is deleted, T_m is most strongly affected near western boundaries since isotherms are no longer shifted there by the swift currents; the annual-mean, surface-heat-flux field \bar{Q} is also changed, with \bar{Q} becoming more positive (negative) to compensate for the absence of warm (cold) currents. Without entrainment cooling, T_m never cools during the summer in the intense upwelling regions in the northern ocean, and the annual-mean heat gain through the ocean surface (the area integral of \bar{Q} over the basin) reverses to become a net heat loss. In individual tests without entrainment cooling, with $T_a = T_m$, and with q_a set to 80% of its saturated value q_s , model SST warms near the northern and southern boundaries during their respective winters by about 1°C, indicating that several processes contribute to wintertime cooling. The T_m field degrades considerably in a single test run with both $T_a = T_m$ and $q_a = 0.8q_s$, so that one or the other of these external forcing fields is required to be able to simulate SST accurately.

The annual-mean circulation has two meridional circulation cells. In the Tropical Cell, water subducts in the southern ocean, flows equatorward in the lower layer of the western-boundary current, and is entrained back into the upper layer in the open-ocean upwelling regions in the southern ocean. In the Cross-Equatorial Cell, the subducted water crosses the equator near the western boundary, where it is entrained in the regions of intense coastal upwelling in the northern ocean. The strength of the cells is directly related to the assumed magnitude of the subduction rate w_d , but their structure is not sensitive to the particular parameterization of w_d used.

CONTENTS

1.	Introduction	182
2.	The model ocean	185
2.1	Dynamic equations	185
2.2	Thermodynamic equations	186
2.3	Entrainment and detrainment	187
2.4	Basin and boundary conditions	189
2.5	Forcing, parameter choices and initial conditions	190
2.6	Numerical method	191
3.	The solution	192
3.1	The annual cycle	192
3.1.1.	May	193
3.1.2.	July	196
3.1.3.	September	201
3.1.4.	November	201
3.1.5.	January	205
3.1.6.	March	209
3.1.7.	The southern Indian Ocean	211
3.2	The annual-mean circulation	213
3.2.1.	Description of the annual-mean fields	213
3.2.2.	Meridional circulation cells	216
3.2.3.	The heat budget	218
4.	Processes	220
4.1	Solutions for modified wind forcing	220
4.1.1.	Modified winds in the Arabian Sea	220
4.1.2.	No winds in the Bay of Bengal	222
4.1.3.	No winds in the Equatorial waveguide	226
4.2	Effect of terms in the T_m equation	228
4.3	Dependence on w_d	231
4.4	The effect of throughflow	233
5.	Summary and discussion	238
6.	Acknowledgements	241
7.	References	241

1. INTRODUCTION

The Indian Ocean is unique in that its northern boundary is located primarily in the tropics. One consequence of this geography is that the northern ocean is forced by intense, annually reversing monsoon winds. These strong winds force the ocean locally, and they excite propagating signals (Kelvin and Rossby waves) that travel large distances to affect the ocean remotely (see for example LUYTEN and ROEMMICH, 1982; TSAI, O'BRIEN and LUTHER, 1992; PERIGAUD and DELECLUSE, 1992). The winds also act to cool sea surface temperature (SST) markedly, directly by heat loss

through the ocean surface and indirectly by causing upwelling of cool subsurface water, making the annual variation of SST in the Arabian Sea one of the largest in any ocean. Due to the upwelling, there is an annual-mean heat flux into the northern ocean; hence, there must be a meridional circulation cell that carries warm surface water out of, and cool subsurface water into, the region; DUING and LEETMAA (1980) in fact remark that the determination of this circulation cell should be a major goal of Indian Ocean research, a goal that has not yet been attained. There is also a flow of Pacific-Ocean water into the Indian Ocean through the Indonesian Archipelago, with a strength estimated to be 10-20 Sv (WYRTKI, 1961; FINE, 1985; FIEUX, personal communication), and the influence of this throughflow is not understood. Thus, the Indian Ocean is an ideal "laboratory" for studying a variety of phenomena, involving coastal, equatorial and subtropical ocean circulations, and the interactions between them.

In this paper we investigate the dynamics and thermodynamics of these and other phenomena using a numerical ocean model. The model is a 2½-layer system with a mixed layer imbedded within the upper layer, essentially a 2½-layer version of the MCCREARY and KUNDU (1989) model. The temperatures of the two active layers are allowed to vary, but effects due to salinity are neglected. The system includes entrainment and detrainment processes allowing the exchange of mass, momentum and heat between the various layers. It is driven by climatological wind and net solar-radiation fields, but develops its own fluxes of sensible and latent heat. As we shall see, our main-run solution compares well with observed current and SST fields, except for a few prominent discrepancies that point toward deficiencies in the model physics.

One focus of our study is to determine the relative importance of *remote vs. local forcing* in the northern Indian Ocean, particularly with regard to the coastal currents along India and Somalia, but we also comment on the remotely-forced circulation in the southern Indian Ocean generated by the Pacific-Ocean throughflow. (Throughout the text we use the term "remote" in a temporal, as well as spatial, sense. For example, there are instances in which circulations generated by winds during the Southwest Monsoon are still present during the Northeast Monsoon, and we consider these features to be remotely forced.) A second focus is to identify the *thermodynamic processes* that maintain the model's SST field. A third is to describe the *meridional circulation cells* that are present in solutions, and to determine the processes that establish them.

Several layer models of Indian-Ocean circulation similar to ours already exist. LUTHER and O'BRIEN (1985), KINDLE and THOMPSON (1989), WOODBURY, LUTHER and O'BRIEN (1989), PERIGAUD and DELECLUSE (1989) and KINDLE, HURLBURT, METZGER and WALLECRAFT (1989) utilize 1½-layer models, whereas POTEMRA, LUTHER and O'BRIEN (1991) and JENSEN (1991) use a 3½-layer system. A key dynamical difference between these systems and ours is the existence of entrainment in our model; as a consequence, the upper-layer thickness in our solutions is generally shallower than in theirs, a difference that tends to enhance the importance of locally forced processes. General circulation models (GCMs) have also been used in several Indian-Ocean studies. The solution of PHILANDER (unpublished research) has been discussed by SCHOTT (1986) with regard to its cross-equatorial western-boundary currents. ANDERSON, CARRINGTON, CORRY and GORDON (1991) contrast the Somali Current eddies present in their GCM solutions with those in the MCCREARY and KUNDU (1988) layer model, and ANDERSON and CARRINGTON (1993) compare Indian-Ocean solutions forced by different wind products. GODFREY and WEAVER (1991) and HIRST and GODFREY (1993) examine the influence of the Pacific-Ocean throughflow in their GCM solutions. SEMTNER and CHERVIN (1992) describe the Indian-Ocean circulations present in their global solution. We comment on relevant aspects of several of these studies at various places in the text.

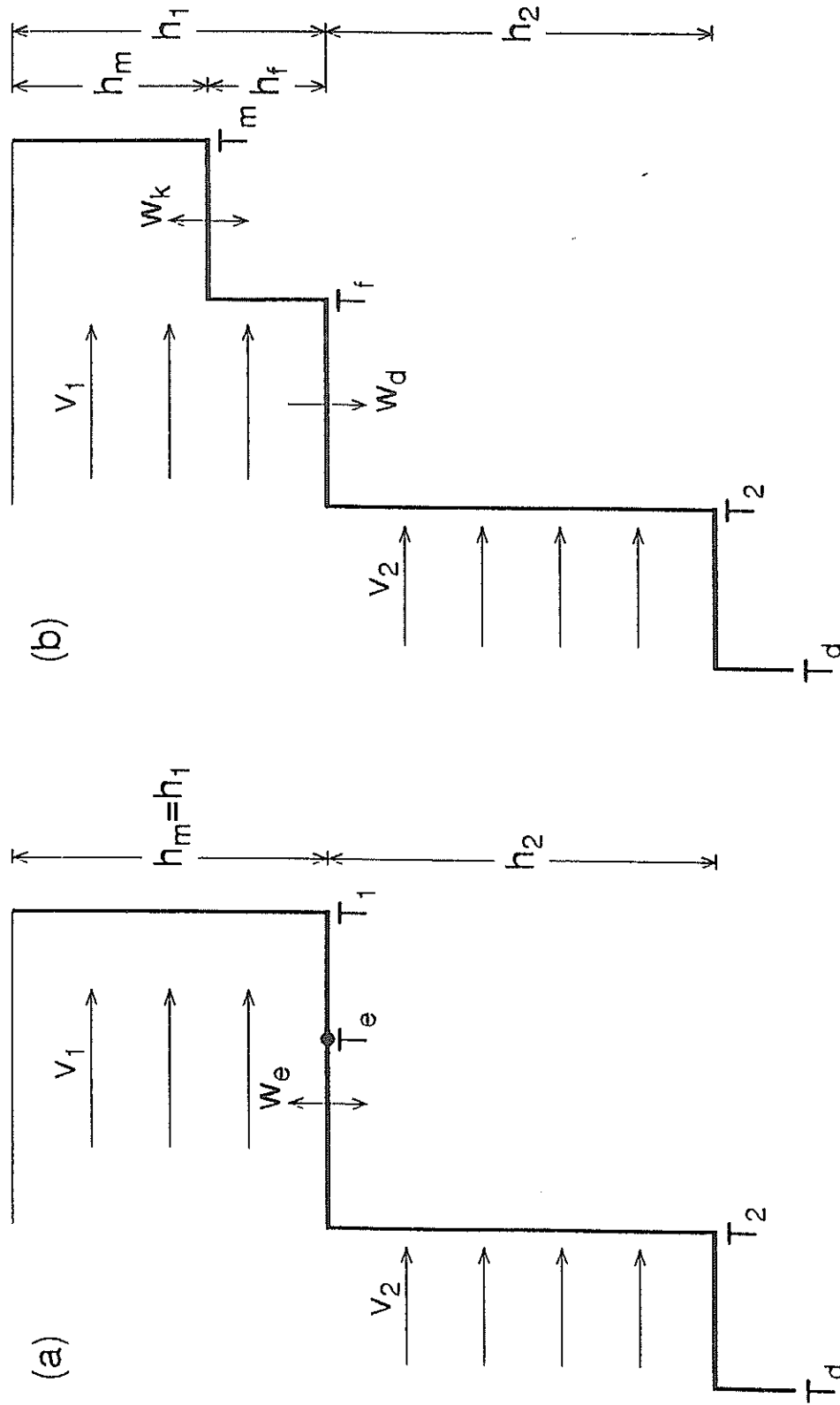


Fig. 1. A schematic diagram of the model layer structure. In Fig. 1a, the mixed layer spreads throughout the upper layer of thickness h_1 and temperature T_1 . In Fig. 1b, the upper layer consists of a mixed layer of thickness h_m and temperature T_m overlying a fossil layer of thickness h_f and temperature T_f and its mean temperature is T_1 . In both situations, the lower layer has thickness h_2 and temperature T_2 , the deep-ocean temperature is T_d , and the currents v_1 and v_2 are depth independent. The mixed layer entrains or detains at a rate w_k defined in equations (6), there is detrainment w_d through the base of the upper layer defined in (7), and the total entrainment velocity through the upper layer is w_e defined in (1). The temperature of the water entrained into the upper layer is T_e , which always has a value between T_2 and T_1 .

2. THE MODEL OCEAN

The two possible vertical structures of the model ocean are schematically illustrated in Fig. 1. In its simpler form (Fig. 1a), the surface layer is a single layer with a thickness h_1 , velocity v_1 and temperature T_1 . In its more complex form (Fig. 1b), the surface layer is split into two parts: a turbulent, well-mixed layer of thickness h_m and temperature T_m , and a nonturbulent "fossil layer" of thickness h_f and temperature T_f . This split is based on observations which show that near-surface temperature profiles have a well-mixed upper part and a staircase-like lower part, the latter being formed during periods of detrainment when the mixed layer retreats due to low winds or surface heating. The velocity field, v_1 , however, is still assumed to be slab-like, so that the shear between the mixed and fossil layers is always neglected. This omission is usually not a bad assumption, since the fossil layer is present primarily in regions of low winds where the shear is *weak* (but see the discussion in Section 5). In both cases, the lower layer of the model of thickness h_2 simulates the average velocity v_2 and temperature T_2 in the depth range of the thermocline. The temperature of the deep, inert ocean is T_d .

The mixed layer entrains ($w_K > 0$) or detrains ($w_K < 0$) water as in the KRAUS-TURNER (1967) model, in which mixing is maintained by turbulence generated at the surface by wind stirring and cooling. The fossil layer is isolated from the surface turbulence, but it can be engulfed into the mixed layer (Fig. 1a) either during periods of strong entrainment by w_K or in upwelling regions where h_1 shallows significantly. Because there is considerable entrainment into the upper layer, there must also be detrainment ($w_d < 0$) through the base of the upper layer to ensure that an upper-layer mass balance can be attained; as we shall see, this process simulates the subduction of surface-layer water into the thermocline (WOODS and BARKMANN, 1986). It is worth noting here that the entrainment velocities, w_K and w_d , are defined to be positive upwards; thus, they tend to increase (decrease) layer thicknesses when their values are positive (negative).

In writing the governing equations it is convenient to utilize the Heaviside step function, defined as $\theta(x) = 1$ if $x > 0$ and $\theta(x) = 0$ if $x < 0$. In addition, we introduce two symbols, δ and ϕ , defined by $\delta = 1$ if $h_f = 0$, $\delta = 0$ if $h_f > 0$, and $\phi = 1 - \delta$. These two symbols distinguish the two physical situations in Fig. 1: $\delta = 1$ and $\phi = 0$ for the situation in Fig. 1a, whereas $\delta = 0$ and $\phi = 1$ for that in Fig. 1b.

With these definitions, the *total* exchange of water across the base of the upper layer can be written as

$$w_e = w_d + \delta w_K \theta(w_K). \quad (1)$$

Note that w_K contributes to w_e only when $\delta = 1$, because only then does the bottom of the mixed layer coincide with the bottom of the upper layer. Moreover, w_K contributes to (1) only when it is positive, since otherwise the mixed layer retreats to form a new fossil layer.

2.1 Dynamic equations

The equations of motion for the upper layer are

$$\begin{aligned} (h_1 v_1)_t + \nabla \cdot (v_1 h_1 v_1) + f k \times h_1 v_1 + h_1 \langle \nabla p_1 \rangle &= \tau \\ + \nu \nabla^2 (h_1 v_1) + v_2 w_e \theta(w_e) + v_1 w_e \theta(-w_e) - \gamma h_1 u_1 i, \\ h_{1t} + \nabla \cdot (h_1 v_1) &= \kappa_h \nabla^2 h_1 + w_e, \end{aligned} \quad (2a)$$

and for the lower layer are

$$\begin{aligned} (h_2 v_2)_t + \nabla \cdot (v_2 h_2 v_2) + f k \times h_2 v_2 + h_2 \langle \nabla p_2 \rangle &= \\ + \nu \nabla^2 (h_2 v_2) - v_2 w_e \theta(w_e) - v_1 w_e \theta(-w_e) - \gamma h_2 u_2 i, \\ h_{2t} + \nabla \cdot (h_2 v_2) &= \kappa_h \nabla^2 h_2 - w_e + w_e. \end{aligned} \quad (2b)$$

In the above, v_i , h_i and T_i are instantaneous values of layer velocity, thickness and temperature, respectively, $\langle \nabla p_i \rangle$ is the depth-averaged pressure gradient in a layer, and the subscript $i = 1, 2$ is a layer index. The surface wind stress is τ , the Coriolis parameter is $f = 2\Omega \sin\theta$, and i and k are unit vectors in the zonal and vertical directions. There is Laplacian mixing of momentum, temperature and layer thickness with coefficients ν , κ_T and κ_h , respectively. The terms proportional to γ act to damp the u_i fields near the southern boundary (see Section 2.4). The terms involving w_e ensure that momentum and mass are conserved when water moves between the two layers. The term w_e is a correction that keeps the total mass in the system fixed to its initial value (see Section 2.3).

The depth-averaged pressure gradients in each layer are:

$$\begin{aligned}\langle \nabla p_1 \rangle &= \alpha g \nabla [h_1(T_1 - T_d) + h_2(T_2 - T_d)] - \frac{1}{2} \alpha g h_1 \nabla T_1, \\ \langle \nabla p_2 \rangle &= \alpha g \nabla [(T_2 - T_d)(h_1 + h_2)] - \alpha g (h_1 + \frac{1}{2} h_2) \nabla T_2,\end{aligned}\quad (2c)$$

where g is the acceleration of gravity, T_d is the temperature of the deep ocean, and

$$T_1 = (h_m T_m + h_f T_f) / h_1 \quad (2d)$$

is the mean value of T_m and T_f . The coefficient of thermal expansion α is assumed to have the constant value $0.00025^\circ\text{C}^{-1}$ throughout the study. See McCREARY and KUNDU (1988) for a discussion of the pressure-gradient terms.

2.2 Thermodynamic equations

The thickness and temperature of the mixed layer are determined from

$$\begin{aligned}h_{mt} + \nabla \cdot h_m \mathbf{v}_1 &= \kappa_h \nabla^2 h_m + \phi w_K + \delta(w_K + w_d), \\ T_{mt} + \mathbf{v}_1 \cdot \nabla T_m &= \kappa_T \nabla^2 T_m + Q/h_m, \\ &\quad - \phi[w_K \theta(w_K)(T_m - T_f)/h_m] - \delta[w_e \theta(w_e)(T_m - T_e)/h_m],\end{aligned}\quad (3)$$

where Q is the heat gain at the ocean surface. Note that when $h_m = h_1$ the rate of movement of water across the base of the mixed layer is $w_K + w_d$, which according to (1) equals w_e only if $w_K > 0$; it is this difference from the h_1 equation in (2a) that allows h_m to separate from h_1 when $w_K < 0$. The terms involving w_K and w_e in the T_m equation (and also the T_f and T_2 equations below) ensure that heat is conserved when mass is exchanged between layers.

The fossil layer exists only when $h_m < h_1$. In that case, its thickness and temperature are given by

$$\begin{aligned}h_f &= h_1 - h_m, \\ T_{ft} + \mathbf{v}_1 \cdot \nabla T_f &= \kappa_T \nabla^2 T_f \\ &\quad + w_K \theta(-w_K)(T_f - T_m)/h_f - w_e \theta(w_e)(T_f - T_e)/h_f.\end{aligned}\quad (4a)$$

When $h_m = h_1$, the fossil layer does not exist, and we set

$$\begin{aligned}h_f &= 0, \\ T_f &= T_m.\end{aligned}\quad (4b)$$

The temperature of the fluid entrained at the bottom of the upper layer is T_e , and it lies between T_2 and T_m (Fig. 1). This is reasonable since T_2 represents the *average* temperature in the depth range of the thermocline, whereas T_e is a typical temperature at its top. Our parameterization of T_e is discussed in Section 2.5.

The lower-layer temperature is given by

$$T_{2t} + v_2 \cdot \nabla T_2 = \kappa_T \nabla^2 T_2 + (T_2^* - T_2)/t_2 - w_e \theta(-w_e)(T_f - T_2)/h_2 - w_e \theta(w_e)(T_3 - T_2)/h_2, \quad (5)$$

where T_2^* is the initial temperature of T_2 and t_2 is a time scale. Note that T_f should be replaced by T_m in (5) when $h_m = h_1$, but that situation is taken care of by the second of equations (4b). The term proportional to $(T_e - T_2)$ causes a *cooling* of the lower layer whenever there is *entrainment* of water into the upper layer; this cooling happens because warm water of temperature $T_e > T_2$ is removed from the top of the lower layer by the entrainment, and heat conservation requires that the *average* temperature of the lower layer must decrease. The artificial heating term $(T_2^* - T_2)/t_2 \equiv Q_2/h_2$ is required to ensure that the system can approach thermal equilibrium: Q_2 is needed to *warm* T_2 in regions of very strong entrainment (such as off the Somali coast during the Southwest Monsoon) because of the cooling process just mentioned; it is also needed to *cool* T_2 in the southern Indian Ocean where there is significant detrainment (Section 3.2.3).

During periods of surface cooling ($Q < 0$), the second of equations (3) allows the possibility that $T_m < T_f$. If this occurs, T_m and T_f are both set to T_1 , an adjustment that conserves heat by virtue of (2d). During periods of entrainment, the numerical integration of equations (3) allows h_m to increase from being less than h_1 to being greater than h_1 in one time step; in that event h_m is set to h_1 , and again T_m and T_f are set to T_1 .

2.3 Entrainment and detrainment

Entrainment and detrainment due to wind stirring and cooling are determined in a manner similar to that in the KRAUS-TURNER (1967) model, except for an adjustment that prevents h_m from becoming much less than a minimum value h_{min} . The net production of turbulent kinetic energy in the layer is

$$P = mu_*^3 - \frac{1}{2} \alpha g Q h_m, \quad (6a)$$

where u_* is the friction velocity and m is an adjustable parameter. The *unadjusted* entrainment and detrainment rates are then given by

$$w'_K = \begin{cases} \frac{P}{\frac{1}{2} \alpha g h_m \Delta T}, & P > 0 \\ \frac{h_{mo} - h_m^-}{2 \Delta t}, & P \leq 0, \end{cases} \quad (6b)$$

where h_m^- is the thickness of the mixed layer evaluated at the previous time level and h_{mo} is the Monin-Obukhov depth,

$$h_{mo} = \frac{mu_*^3}{\frac{1}{2} \alpha g Q}, \quad (6c)$$

determined by setting $P=0$ in (6a). According to (6b), detrainment occurs whenever $P \leq 0$, and in that case the thickness of the mixed layer rapidly adjusts to h_{mo} in one time step of the integration Δt . In the Kraus-Turner model, ΔT is the temperature difference between T_m and the underlying layer. Just as for $T_e(y)$, it is impossible to specify ΔT precisely because the lower layer represents the thermocline region. For this reason, here we simply set ΔT to a constant value of 4°C (see Section 2.5).

The *adjusted* rate is then

$$w_K = \begin{cases} w'_K, & h' > h_{\min} \\ \frac{h_{\min} - h_m}{2\Delta t}, & h' \leq h_{\min}, \end{cases} \quad (6d)$$

where the unadjusted mixed-layer thickness is $h' \equiv h_m^- + 2\Delta t w'_K$. Note that this adjustment does not ensure that $h_m \geq h_{\min}$; for example, even after the adjustment the solution of the first of equations (3) will result in h_m being *slightly* less than h_{\min} in upwelling regions, where the term $\nabla \cdot (h_m \mathbf{v}_1)$ is positive. On the other hand, the adjustment preserves the essential properties of momentum and heat conservation.

Our parameterization of detrainment is intended to simulate the subduction process hypothesized by WOODS and BARKMANN (1986). In this scenario, the mixed layer deepens in the winter due to entrainment caused by surface cooling; it shallows in the spring due to surface heating, and at that time water in the deeper part of the layer subducts (detrains) into the thermocline. Accordingly, we represent detrainment out of the upper layer by

$$w_d = - \frac{Q\theta(Q)}{Q_0} \frac{(H_d - h_1)^2}{t_d H_d} \theta(h_1 - H_d), \quad (7)$$

where t_d is an arbitrary "detrainment" time scale, and Q_0 is a scaling parameter with a value of the order of the mean heat flux into the ocean (so that the factor involving Q is order one). Thus, the upper layer detrains wherever Q is positive *and* h_1 is thicker than a specified "detrainment depth" H_d . Although the physics parameterized in (7) are reasonable (NURSER and MARSHALL, 1991), they are not well founded observationally. In Section 4.3 we report on several test calculations which vary the strength and form of w_d .

Because the southern boundary is open (Section 2.4), the total mass in the system need not be conserved, and this is a potentially serious problem for the long integrations reported in this paper. (For example, without any correction scheme, the net volume of water in the ocean basin increased by 10% after 5 years of integration, equivalent to an average transport of about 6Sv into the basin.) The change in volume at the end of each time step is

$$\Delta V = \iint (h_1 + h_2) dx dy - \iint (H_1 + H_2) dx dy, \quad (8a)$$

where the integrals extend over the area A of the basin, and H_1 and H_2 are the initial values of h_1 and h_2 , respectively. To ensure that mass is conserved, we add a "correction" volume $\Delta v = \Delta V$ to the lower layer. This volume is confined to a small rectangular region located at the southwestern corner of the basin and is defined by the wedge-shaped thickness field

$$h_c(x, y) = \Delta h \frac{x - x_1}{x_0 - x_1} \frac{y - y_1}{y_0 - y_1} \theta[(x_1 - x)(y_1 - y)], \quad (8b)$$

where $x_0 = 35^\circ\text{E}$, $x_1 = 37.5^\circ\text{E}$, $y_0 = -29^\circ$ and $y_1 = -24^\circ$. The relation $\Delta h = -4\Delta V / [(x_1 - x_0)(y_1 - y_0)]$, which follows from the constraint $\Delta v = \int_{y_0}^{y_1} \int_{x_0}^{x_1} h_c(x, y) dx dy = -\Delta V$, then determines h_c . Accordingly, after each time step h_2 is modified by the replacement

$$h_2 \rightarrow h_2 + h_c(x, y), \quad (8c)$$

a procedure equivalent to including the additional entrainment rate

$$w_c(x, y) = \frac{1}{2\Delta t} h_c(x, y) \quad (8d)$$

in the second of equations (2b).

The effect of correction (8) is to establish a western-boundary current through the open boundary that cancels any inflow (or outflow) in the interior ocean, a physically reasonable process (see Section 3.1.7). An alternative procedure that we originally used was to remove water *uniformly* from the lower layer, that is, h_c was taken to have the constant value $-\Delta V/A$ where A is the area of the basin. The instantaneous flow fields of solutions using one or the other of these two correction schemes are quite similar. However, the weaker meridional circulation is badly distorted when w_c is taken to be uniform (the profile WC in Fig. 4 extends throughout the basin), which makes it difficult to define the meridional circulation cells that are present in solutions.

2.4 Basin and boundary conditions

The model basin is shown in any of the panels that display the solution. The thick lines in the panels all represent vertical walls. Within the basin, the ocean bottom is assumed to lie everywhere beneath the bottom of the lower layer, so that topographic features not shown in the panels do not affect model behaviour. (See WOODBURY *et al.*, 1989, for a discussion of the effects of some of these features.)

With one exception, the conditions applied at the western, northern and eastern boundaries, as well as around Madagascar, are

$$u_i = v_i = h_{in} = h_{mn} = T_{mn} = T_{fn} = T_{2n} = 0 \quad (9a)$$

where the subscript n indicates a partial derivative normal to the boundary. The exception is for the solution that includes Pacific-Ocean throughflow which utilizes modified conditions on v_i (Section 4.4). The condition $h_{in} = 0$ ensures that the horizontal mixing on h_i does not allow mass to diffuse across the boundary.

The southern boundary of the model does not coincide with any real boundary of the Indian Ocean, and we apply the zero-gradient, open boundary conditions

$$u_{iy} = v_{iy} = h_{iy} = h_{my} = T_{my} = T_{fy} = T_{2y} = 0 \quad (9b)$$

The condition $u_{iy} = 0$ allows the development of a large-scale instability along the open boundary, and a damper is applied on u_i to inhibit its growth; the damping coefficient $\gamma(y)$ is set to zero at distances greater than 300 km from the boundary, increases linearly in the interval from 300 km to 150 km, and is then constant up to the boundary. There is no corresponding damper on v_i and h_i , and so fluid can pass freely across the open boundary.

2.5 Forcing, parameter choices and initial conditions

Unless specified otherwise, the wind stress τ forcing the model is the climatology of HELLERMAN and ROSENSTEIN (1983). In all the solutions, the thermal forcing $Q(=Q_r+Q_s+Q_L)$ is calculated from the climatological fields of net solar radiation Q_r (incoming shortwave radiation minus outgoing longwave radiation), air temperature T_a , specific humidity q_a , and scalar wind V_s . These fields were derived by RAO, MOLINARI and FESTA (1989, 1991) from the climatological Comprehensive Oceanographic and Atmospheric Data Set (COADS). They were provided on a $2^\circ \times 2^\circ$ grid for each month, and linearly interpolated in space and time onto our numerical grid. The sensible heat flux Q_s and latent heat flux Q_L are both estimated from these fields using standard bulk formulae, with model surface temperature T_m (rather than observed SST) used to calculate Q_s and Q_L , as in McCREARY and KUNDU (1989). The drag coefficients for each formula are listed in Table 1. To model the observed increase of C_L with the air-sea temperature difference (BUNKER, 1976), C_L is assumed to vary linearly with $(T_m - T_a)$ for $|T_m - T_a| \leq 3^\circ\text{C}$, beyond which range it is fixed to its maximum or minimum values of .002 and .001. To simulate the effect of small-scale air turbulence, the scalar wind V_s is assumed to have a minimum value of 6 m s^{-1} .

TABLE 1. A list of parameters used in the main run.

Parameter	Notation	Value
Coefficient of thermal expansion	α	$0.00025^\circ\text{C}^{-1}$
Maximum strength of damper	γ	1 day^{-1}
Coefficient of eddy viscosity	ν	$5 \times 10^7 \text{ cm}^2 \text{ s}^{-1}$
Mixing coefficient for temperature	κ_T	$5 \times 10^7 \text{ cm}^2 \text{ s}^{-1}$
Mixing coefficient for layer thickness	κ_h	$1 \times 10^7 \text{ cm}^2 \text{ s}^{-1}$
Initial depth of upper layer	H_1	65m
Initial depth of lower layer	H_2	250m
Minimum mixed-layer depth	h_{\min}	35m
Detrainment depth	H_d	65m
Detrainment time scale	t_d	180 days
Time scale for Q_2	t_2	1440 days
Heat-flux scaling parameter	Q_o	40 W m^{-2}
Wind-stirring coefficient	m	1.0
Temperature difference in equation (6b)	ΔT	4°C
Initial temperature of lower layer	T_2^*	15°C
Temperature of deep ocean	T_d	0.0°C
Drag coefficient for Q_s	C_s	.001
Drag coefficient for Q_L	C_L	$.0015 + .00033(T_m - T_a)$
Mode-1 characteristic speed	c_1	347 cm s^{-1}
Mode-2 characteristic speed	c_2	125 cm s^{-1}
Mode-2 Rossby-wave speed at 7.5°N	$c_{r2}(7.5^\circ)$	9.9 cm s^{-1}
Mode-2 Rossby-wave speed at 15°N	$c_{r2}(15^\circ)$	2.5 cm s^{-1}
Ratio of coupling coefficients	F_2/F_1	2.7

The “main run” of our study uses the parameter values listed in Table 1. They are either physically realistic or numerically sensible choices. Although the list is long, solutions are not very sensitive to most of them. Mixing of layer thicknesses is included to smooth h_m , which otherwise develops some small-scale noise; the value of κ_h is kept as small as possible to minimize its effect on the annual-mean mass budget (Fig.5). There are no “correct” choices for the mixing parameters, m and ΔT , in equation (6a). Our choice $m=1$ is a commonly used value, but in any case solutions are not

sensitive to m because generally turbulence production P is more strongly influenced by the surface heat flux Q than by μ_*^3 . The deepening of the mixed layer during the winter is sensitive to ΔT , and the choice of $\Delta T = 4^\circ\text{C}$ ensures that h_m deepens to realistic values in the southern Indian Ocean. See MCCREARY and KUNDU (1989) for a further discussion of changes caused by varying mixed-layer parameters. Likewise, there are no correct values for the detrainment parameters, H_d and t_d , in equation (7). With $H_d = 65\text{m}$ and $t_d = 90$ days, h_1 shallows in the southern Indian Ocean from thicknesses of the order of 160m in the southern-hemisphere winter to 90m in the summer, ensuring that considerable subduction occurs there. Effects of varying H_d and t_d are discussed in Section 4.4. The time scale t_2 for the artificial heating term Q_2 is set to 1440 days; this choice is large enough to minimize the effects of Q_2 in the overall heat budget (Section 3.2.3), and yet small enough to prevent T_2 from cooling too much in the intense upwelling region off Somalia.

The background stratification is characterized by the parameters H_1 , H_2 , T_2^* and T_d , and their values in Table 1 are typical for the Indian Ocean. One important effect of these parameters is that they determine the speeds of waves present in the model. The characteristic speeds c_n for the two baroclinic modes of a linear, $2\frac{1}{2}$ -layer system are given by

$$c_{(f)} = \left[\frac{1}{2}(a_{11} + a_{22}) \pm \frac{1}{2}[(a_{11} - a_{22})^2 + 4a_{12}a_{21}]^{1/2} \right]^{-1/2}, \quad (10)$$

where $a_{11} = (a_0/H_1)(\rho_2/\rho_1)$, $a_{22} = (a_0/H_2)(\Delta\rho_{31}/\Delta\rho_{32})$, $a_{12} = -(a_0/H_1)$, $a_{21} = -(a_0/H_2)$, $a_0 = (g\Delta\rho_{21})^{-1}$, $\rho_i = \bar{\rho} - \alpha g T_i$, $\bar{\rho} = 1\text{gm cm}^{-3}$ and $\Delta\rho_{ij} = \rho_i - \rho_j$ (MCCREARY and YU, 1992). For the parameter choices in Table 1 and with $T_1 = 28^\circ\text{C}$, their values are $c_1 = 347\text{cm s}^{-1}$ and $c_2 = 125\text{cm s}^{-1}$. For future reference, the non-dispersive, propagation speed of a mode-2 Rossby wave is $c_{r2} = \beta c_2^2/f^2$; using the above value of c_2 , this speed decreases from 9.9cm s^{-1} at 7.5°N to 2.7cm s^{-1} at 15°N . The stratification also determines how efficiently each baroclinic mode couples to the wind, and the coupling coefficients are

$$F_n = \left[1 + \frac{(1 - a_{11}c_n)^2}{c_n^4 a_{12}a_{21}} \right]^{-1}. \quad (11)$$

For the above parameter choices $F_2/F_1 = 2.7$, implying that the mode-2 response generally is much stronger than the mode-1 response.

The parameterization of the entrainment temperature T_e is influential through its effect on model SST. One logical choice for T_e is to set it equal to T_2 ; however, in a test calculation with this parameterization, T_m became much colder than climatological SST in the upwelling region off Somalia during the Southwest Monsoon (MCCREARY and KUNDU, 1989). To avoid this problem, we prescribed T_e from climatological SST data as follows. We first determined the minimum value of SST that occurs along each latitude line, thereby defining a profile $\text{SST}_{\min}(y)$. Since upwelled water is expected to have a temperature slightly colder than this minimum, we then set $T_e(y) = \text{SST}_{\min}(y) - 2^\circ\text{C}$. Note that T_e is a function only of latitude; thus, this parameterization ensures that T_m never gets much cooler than climatological SST, but it does not otherwise affect its horizontal structure.

2.6 Numerical method

Solutions are found numerically on a staggered grid, with variables defined in rectangular grid boxes of dimension $\Delta x = \Delta y = 55\text{km}$. The h_1 and T_1 points are located at the center of the boxes, while u_i and v_i points are located on meridional and zonal edges of the boxes, respectively. Equations are integrated forward in time, using the leap-frog scheme with a time step $\Delta t = 1$ hour. To inhibit time-splitting instability, the fields are averaged between successive time levels every 41

time steps. Diffusive terms are evaluated at the backward time level, and all other terms at the central time level.

The main run is spun up from a state of rest beginning on April 15, a time during the transition between the monsoons when the winds are weak. To inhibit the excitation of inertial oscillations, the wind stress driving the model is ramped up from zero to the appropriate level over 5 days. The initial values of h_m and h_1 are both H_1 , that of h_2 is H_2 , those for T_m and T_f are the observed April SST field, and that of T_2 is T_2^* . The model is integrated forward in time for a period of 10 years by which time it approaches stationarity, and all figures shown are taken from year 10. The test calculations in Section 4 are all restarted from year 8 of the main run, integrated for several more years, and results are shown from year 10, 16 and 12 for the solutions in Sections 4.2, 4.3 and 4.4, respectively.

3. THE SOLUTION

In this section, we first describe the annual cycle of our main-run solution, and compare it with climatological current and SST fields (HASTENRATH and LAMB, 1979; CUTLER and SWALLOW, 1984; RAO *et al* 1989, 1991) and other observations. Sections 3.1.1-3.1.6 provide a bimonthly description of the highly variable circulations in the northern Indian Ocean beginning at the onset of the Southwest Monsoon in May. Section 3.1.7 reports on the less variable flow field in the southern Indian Ocean throughout the year. Then, in Section 3.2 we discuss the solution's annual-mean circulation, and among other things find that it contains a cross-equatorial, meridional circulation cell that extends from the northern to the southern boundaries of the basin.

3.1 The annual cycle

Figures 2a-2f provide an overview of both the main run and observed fields, showing bimonthly distributions of upper-layer thickness h_1 , mixed-layer temperature T_m and upper-layer currents v_1 for the main run, as well as climatological wind τ , ship-drift v_{obs} and SST fields prepared by RAO *et al* (1989, 1991). In addition, Figs 2a' and 2d' show lower-layer currents v_2 for the solution in May and November, and Figs 2b' and 2e' show v_2 , mixed-layer thickness h_m , entrainment velocity w_e and surface heat flux Q for the solution in July and January. The lower-layer temperature field T_2 is not shown because it remains almost everywhere close to its initial value T_2^* , the primary exception being the upwelling region off Somalia where T_2 drops to a minimum value of 8.2°C in July. It is also worth noting that $T_1 - T_2$ never becomes negative in the solution, its minimum value being 0.2°C in the southeastern ocean in September.

The current arrows in all the figures (and in all the current plots in Section 4 as well) are of the vector field $v' \equiv v/|v|^{1/2}$, which has the same direction as v but an amplitude of $|v|^{1/2}$; this modification enhances the strength of weak flows relative to stronger ones, allowing them to be more visible in each plot.

Throughout the discussion, we point out the dynamic and thermodynamic processes that account for prominent features in the solution. The structure of h_1 is particularly useful in this regard. First, regions of extremely shallow or deep h_1 are generally good indicators of a locally forced response: regions of shallow h_1 suggest either coastal upwelling or Ekman suction by wind curl in the interior ocean; regions of deep h_1 indicate either mixed-layer deepening by convective overturning ($Q < 0$) or Ekman pumping. Second, ∇h_1 is a measure of the geostrophic shear between the upper and lower layers; therefore, except in regions of strong wind where Ekman drift is strong, upper-layer currents tend to flow to the right of $-\nabla h_1$ in the northern hemisphere, and lower-layer

currents often flow to its left. Another useful indicator of dynamics is the vertical structure of the flow field: well-organized features in which the currents are *directed oppositely* in the two layers almost always indicate the presence of a remotely forced, mode-2 wave.

Although both mode-1 and mode-2 waves are always generated by the wind, there is little indication of mode-1 waves in our solutions. The primary reason for this is that the second baroclinic mode couples much more efficiently to the wind, the ratio of coupling coefficients being $F_2/F_1 = 2.7$ (Eq. 11); hence, the mode-2 response tends to mask the weaker mode-1 waves. JENSEN (1991) also notes the relatively weak amplitude of mode-1 waves in his solutions.

3.1.1. May: The winds in the Arabian Sea begin to blow from the southwest in May, and the ocean responds quickly, particularly along basin boundaries. Consistent with the classical picture of the coastal response to upwelling-favorable local winds, h_1 shallows along the coasts of Somalia and Arabia, the model Somali Current reverses to form a swift northward jet, and a weaker northward current develops off the Arabian coast (compare the middle-left and upper-right panels of Figs 2a and 2f). Similar changes take place in the ship-drift observations (lower-left panels of Figs 2a and 2f). Synoptic observations suggest further that at this early stage of the Southwest Monsoon the Somali Current retroflects just north of the equator, with part of the retroflected water recirculating south of the equator to form a closed gyre, generally known as the "Southern Gyre" (BRUCE, 1973; SWALLOW, MOLINARI, BRUCE, BROWN and EVANS, 1983), and that north of the retroflexion a second gyre, the "Great Whirl", begins to form. There are indications of a southern retroflexion and the formation of the two gyres in both the solution and the ship-drift observations.

A southward Somali Undercurrent is present in the lower layer of the solution from about 5°N to the equator (Fig. 2a'). It develops during March in response to forcing by winds within the Arabian Sea, but by May it appears to be primarily remotely forced by the radiation of Rossby waves from the coast of India (see Section 4.1.1). A similar, springtime undercurrent was observed along the Somali coast in May, 1979, that deepened and weakened to the north; at 5°N its maximum speed was 60cm s^{-1} near a depth of 175m, whereas at 9°N the flow was northward near 175m with a maximum southward current of only 10cm s^{-1} at 350m (LEETMAA, QUADFASSEL and WILSON, 1982).

A striking development along the west coast of India is the appearance of a region of shallow h_1 , an equatorward surface current, and a weak ($5\text{--}10\text{cm s}^{-1}$) poleward coastal undercurrent (Fig. 2a'). Ship-drift observations show that a southward flow appears along the west coast in March, reaches a peak strength in July and vanishes by October (lower-left panels of Figs 2a-2c; SHETYE and SHENOI, 1988). JOHANNESSEN, SUBBARAJU and BLINDHEIM (1981) reported that isotherms tilt upward toward the coast from April until September, and ANTONY (1990) noted the presence of downward-tilting isotherms at greater depths, a feature indicative of a northward coastal undercurrent. SHETYE, GOUVEIA, SHENOI, SUNDAR, MICHAEL, ALMEIDA and SANTANAM (1990) calculated the dynamic topography relative to 1000db at various locations along the coast, finding that during the Southwest Monsoon there was an equatorward coastal current and a poleward undercurrent with its core at 150m or below. The upwelling-favorable (equatorward) component of the winds along the west coast strengthens in April, reaches a peak of 0.5dyn cm^{-2} in August and weakens in October (Figs 2a-2c, SHETYE, 1984; SHETYE and SHENOI, 1988), and for this reason SHETYE *et al* (1990) suggested the currents were locally forced by these winds. As noted below and confirmed in Sections 4.1.1 and 4.1.2, a remote-forcing mechanism contributes equally to their development in the model.

The model circulation in the western Bay of Bengal also begins to respond to the strengthened winds. This response can be clearly seen in the structure of the h_1 field, which shallows along the east coast of India from 10°N to 20°N as a result of the upwelling-favorable winds there (contrast

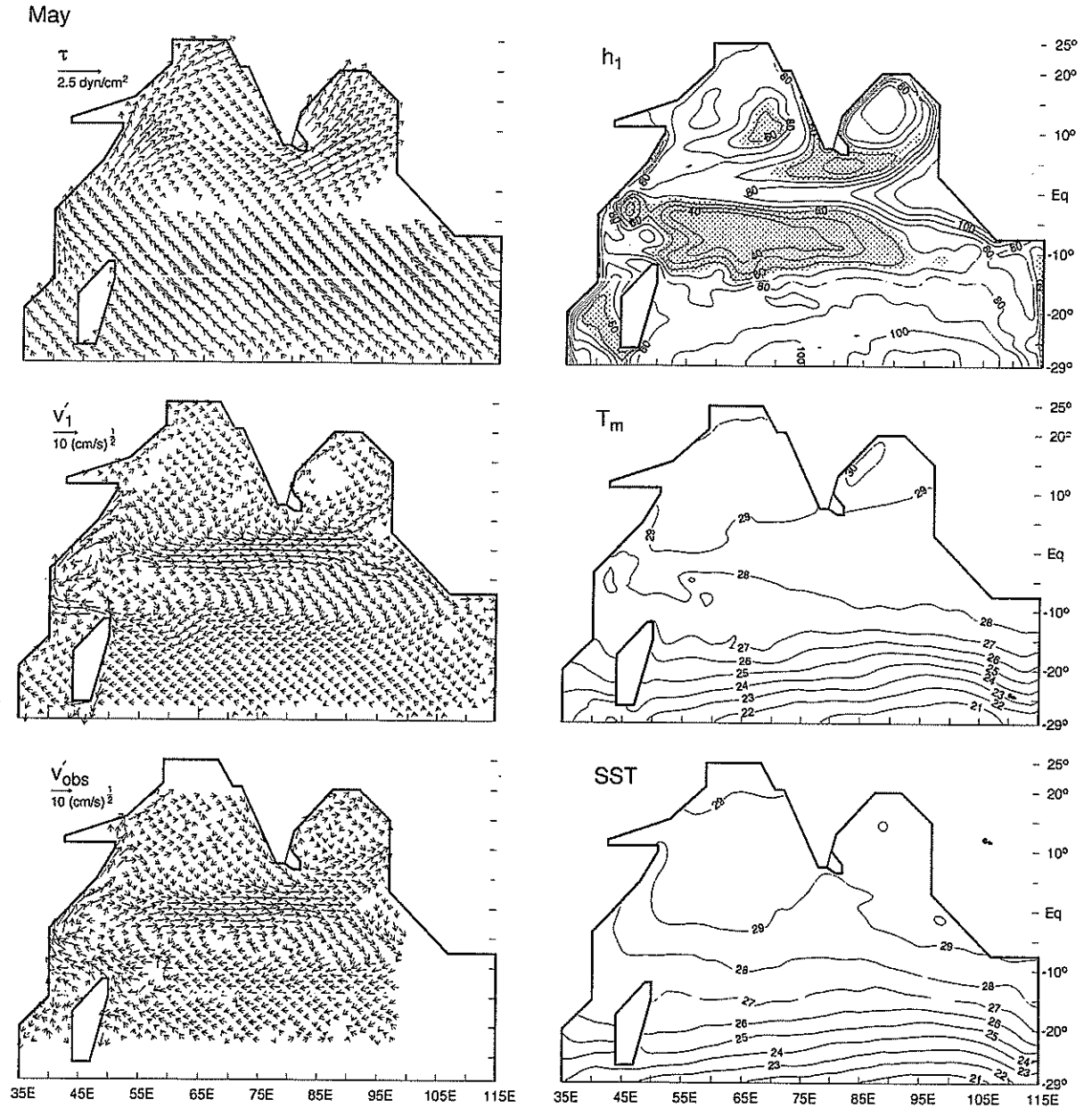


Fig.2a. Horizontal distributions in May of climatological wind stress τ , ship-drift currents v_{obs} and SST fields, as well as upper-layer thickness h_1 , upper-layer current v'_1 and mixed-layer temperature T_m fields for the main run. Data for v_{obs} are available only in the region $x \leq 99^\circ\text{E}$, $23^\circ\text{S} \leq y \leq 19^\circ\text{N}$. The contour interval for h_1 is 10m, and regions where $h_1 \leq 65\text{m}$ are shaded. The contour interval for T_m and SST is 1°C . To emphasise the weaker flows, current arrows are of the vector field $\mathbf{v}' = \mathbf{v}/|\mathbf{v}|^{1/2}$. In response to upwelling-favorable winds, h_1 shallows and northward surface currents develop along the coasts of Somalia and Arabia as well as the east coast of India. In response to local forcing and to remote forcing by the Bay-of-Bengal winds, h_1 shallows and a southward flow appears on the west coast of India. Ekman suction by positive wind curl causes h_1 to rise in a band south of India. There is eastward flow along the equator, the springtime Wyrtki jet, generated by strengthened near-equatorial westerlies.

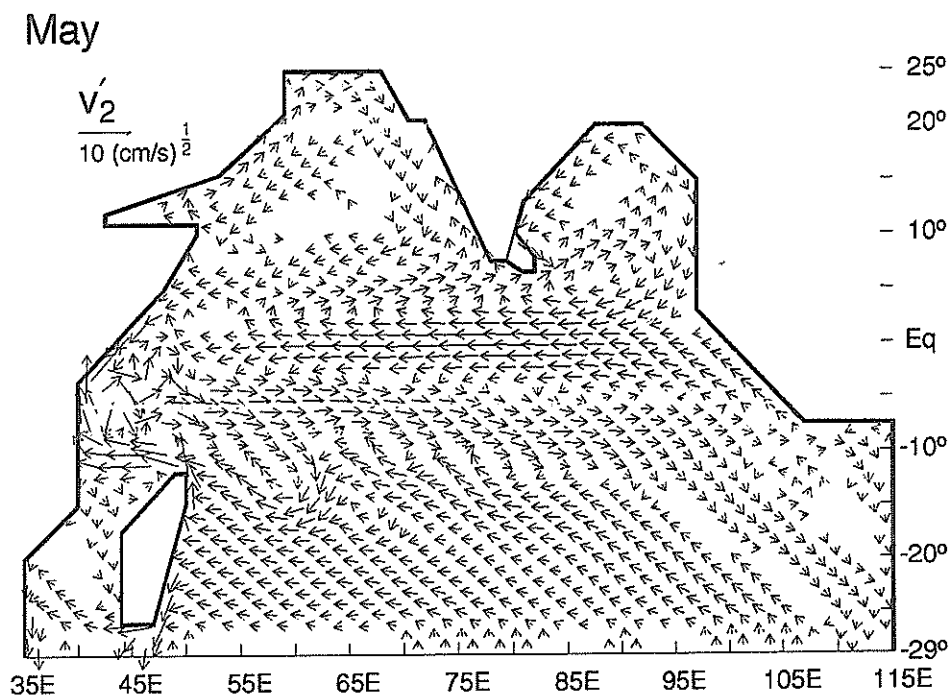


Fig.2a'. As in Fig.2a, except showing the lower-layer current v'_2 . There is a southward Somali Undercurrent from 7°N to the equator, northward and southward undercurrents along the west and east coasts of India, and westward flow along the equator.

the upper-right panels of Figs 2a and 2f). In addition, the northward coastal current, already present in March (see Section 3.1.6), strengthens to speeds of the order of 50 cm s^{-1} , and a southward coastal undercurrent develops (Fig.2a'). Consistent with the model, ship-drift observations also show a stronger, poleward coastal current in May (lower-left panels of Figs 2a and 2f). Moreover, SHETYE, SHENOI, GOUVEIA, MICHAEL, SUNDAR and NAMPOOTHORI (1991b) report that after the onset of the Southwest Monsoon of 1987, there were many indications of active upwelling along the east coast, with near-surface isopycnals tilting upward within 40km of the coast, and deeper isopycnals sloping downward suggestive of a southward undercurrent.

There is also a shallowing of h_1 in a band south of India that extends from about 65°E across the southern Bay of Bengal. This shallowing results from Ekman pumping driven by positive wind curl north of the axis of the wind maximum. This change is also reflected in the model flow field, with the westward current just south of India in March being replaced by a southward Ekman drift across the wind axis. Note that this shallow region is continuous with the one along the west coast of India. This property suggests an alternate forcing mechanism for the west-coast upwelling: remote forcing by winds in the Bay of Bengal and south of India via the northward propagation of the raised thermocline along the west coast of India as a packet of Kelvin waves (see Sections 4.1.1 and 4.1.2).

There is an eastward current along the equator, the model's springtime WYRTKI (1973) jet. It has speeds approaching 80 cm s^{-1} , somewhat greater than the value of about 50 cm s^{-1} determined from ship-drift observations and surface drifting-buoy data (MOLINARI, OLSON and REVERDIN, 1990). This jet, forced by the westerly component of the near-equatorial winds, appears first in the central and eastern ocean in April and expands westward in May, as in the observations (MOLINARI *et al*, 1990). The westward expansion is no doubt partly a locally forced response, since the forcing

region itself (the region of westerly winds) also expands westward at this time; however, Rossby-wave propagation likely contributes to the phenomenon as well.

The equatorial jet splits in the eastern ocean, forming poleward currents along the eastern boundary that reverse the eastern-boundary currents present in March; in particular, northward flow now exists everywhere along the eastern boundary of the Bay of Bengal. The flow field is associated with a pattern of increased h_1 along the equator in the eastern ocean, where h_1 reaches a maximum thickness greater than 110m as compared to only 75m in March, and the corresponding lower-layer currents (Fig.2a') are directed oppositely to the upper-layer currents. All these characteristics indicate that this response results from a downwelling, mode-2 equatorial Kelvin wave, together with a packet of reflected coastal Kelvin waves and Rossby waves.

Model SST is uniformly warm in the northern ocean, surface heating having eliminated all traces of the wintertime cooling in the northern Arabian Sea and Bay of Bengal (contrast the middle-right panels of Figs 2e, 2f and 2a). Isotherms at this time begin to bend northward along the Somali coast. The w_e field (not shown) is zero there, so this feature is not caused by upwelling which does not begin until June. Rather, the bending results primarily from the alongshore advection of cool water from the south by the Somali Current: it is absent in a test run in which advection is dropped from the T_m equation. The observed SST pattern is strikingly similar to model SST, showing a similar northward bending along Somalia and little indication of significant upwelling (lower-right panel of Fig.2a; HASTENRATH and LAMB, 1979).

3.1.2. July: The Southwest Monsoon reaches its peak strength in July. In response, the model Somali Current strengthens to speeds approaching 300cm s^{-1} , close to those observed during synoptic cruises (SWALLOW *et al.*, 1983), but somewhat larger than average speeds obtained from ship-drift observations and buoy data (MOLINARI *et al.*, 1990). Consistent with synoptic observations, the Southern Gyre strengthens and is centered farther north near 4°N ; however, the Great Whirl near 9°N does not become well developed in the solution. We have not carried out any diagnostic calculations to determine why there is no Great Whirl in this solution. It is known, however, that details of the structure and time development of the highly nonlinear eddy field in the Somali Current region are very sensitive to model parameters (MCCREARY and KUNDU, 1988; PERIGAUD and DELECLUSE, 1989; ANDERSON *et al.*, 1991), and in fact a Great Whirl *does* develop in one of our test runs (see Section 4.3 and Fig.12).

The southward Somali Undercurrent has now vanished, being replaced by a northward flow everywhere north of about 1°N (upper-left panel of Fig.2b'). This reversal is forced by the intense coastal upwelling between 5°N and 10°N (lower-left panel of Fig.2b'), the system generating the northward lower-layer current in order to provide a source for the upwelled water (MCCREARY and KUNDU, 1989). Current-meter observations at 5°N indicate that, although the southward Somali Undercurrent does vanish at this time, it does not reverse (QUADFASSEL and SCHOTT, 1983). A likely reason for this difference is that the reversal in our solution results from the model's limited vertical resolution. The undercurrent might not reverse in a system with deeper layers unaffected by the upwelling process (for example, as in the JENSEN, 1991, model).

The upper-layer thickness h_1 increases markedly in the interior of the Arabian Sea to more than 120m, primarily because of Ekman convergence associated with the strong, negative wind curl southeast of the wind axis. Similarly, h_1 shallows west of the wind axis (within 300-400km of the Arabian coast) as a result of Ekman divergence. These changes in the depth of the pycnocline are well known, and the role of Ekman pumping in their generation has been noted in several prior modelling studies (SMITH and BOTTERO, 1977; LUTHER and O'BRIEN, 1985; MCCREARY and KUNDU, 1988, 1989; BAUER, HITCHCOCK and OLSON, 1991). Consistent with geostrophy, the upper-layer currents circulate about the region of large h_1 , flowing to the east and south at speeds of the order of 25cm s^{-1} .

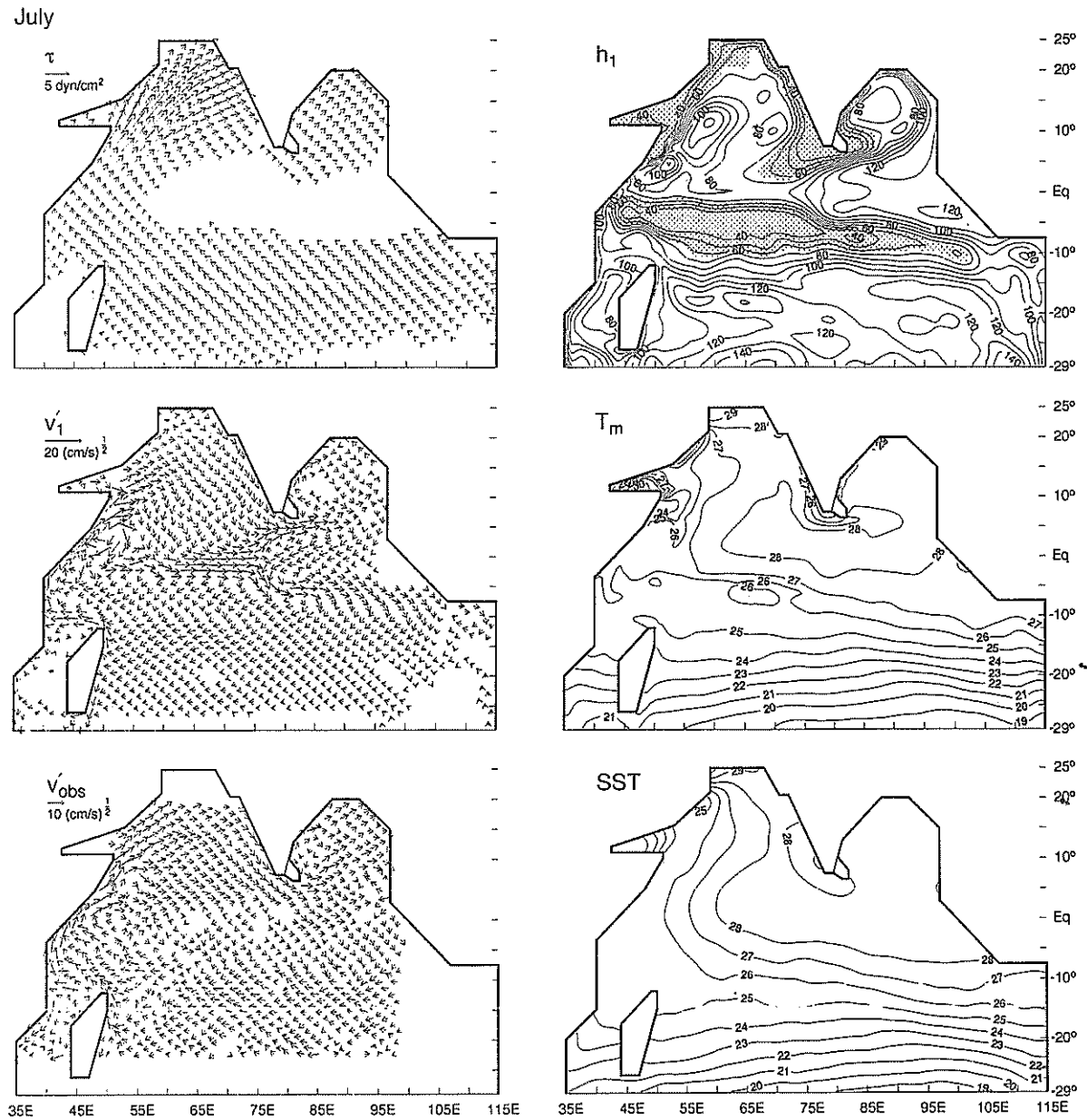


Fig.2b. As in Fig.2a, except in July. In response to the strong Southwest-Monsoon winds, h_1 shallows everywhere along the boundaries of the Arabian Sea, and deepens in the central Arabian Sea. In the Bay of Bengal, h_1 tilts upward from north to south along the east coast of India, h_1 is deep in the eastern Bay, and regions of shallow and deep h_1 "meet" along the northeast coast of India. There is a strong eastward current southeast of India, the Indian Monsoon Current, in both the solution and the ship-drift observations. In contrast to the observations, Arabian-Sea water crosses the equator to flow westward south of the equator, and there is a westward current along the equator in the eastern basin. Model SST cools markedly in upwelling regions off Somalia, Arabia and the coasts of India; a similar cooling is not apparent in climatological SST because of the averaging procedure.

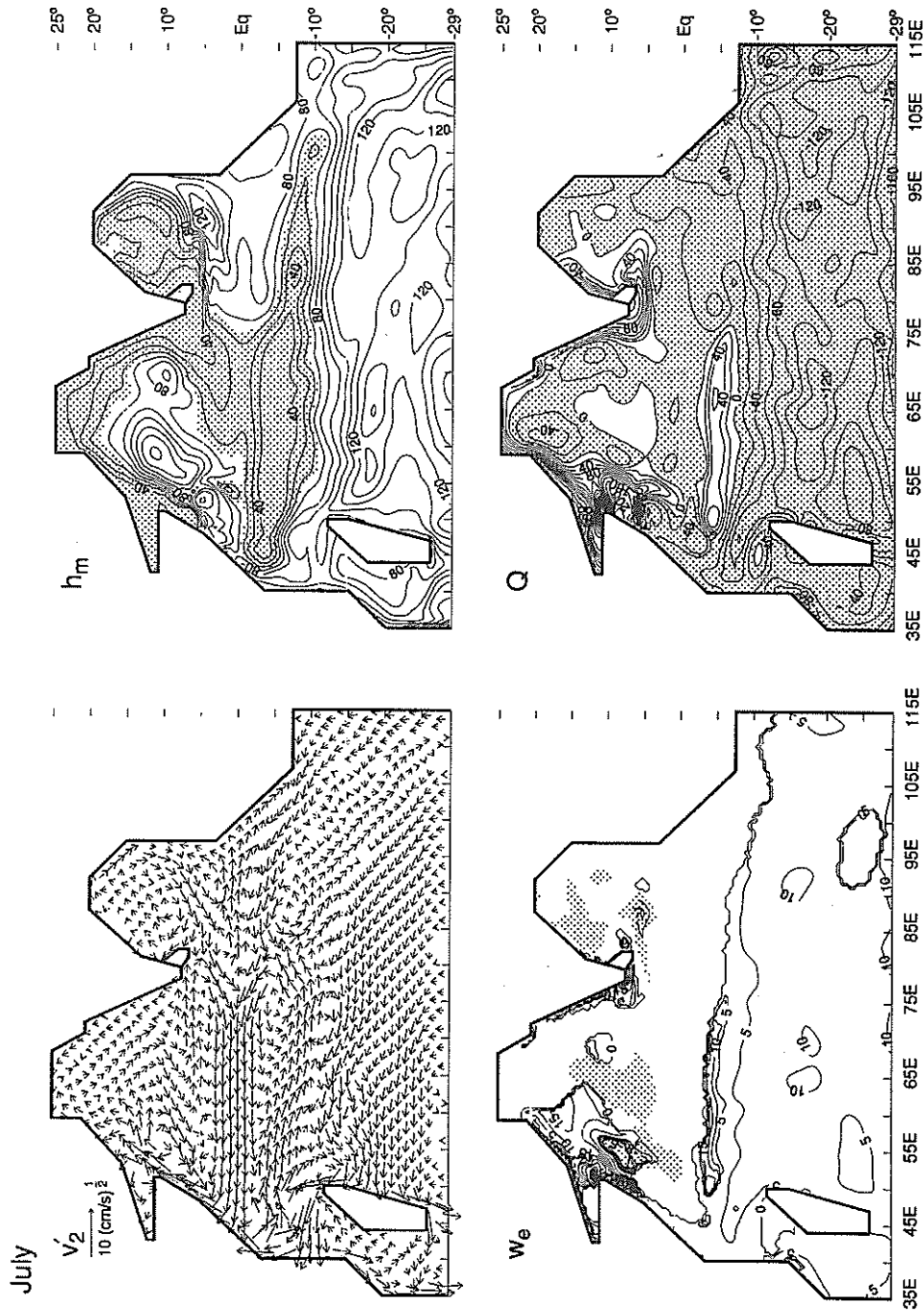


Fig. 2b'. As in Fig. 2b except showing the lower-layer current v_2 , mixed-layer thickness h_m , entrainment rate w_e , and net surface heat flux Q for the main run. Contour intervals for h_m and Q are 10m and 20 W m^{-2} , respectively; regions where $h_m \leq 65 \text{ m}$ and $Q \leq 0$ are shaded. Contour intervals for w_e are $5 \times 10^{-4} \text{ cm s}^{-1}$ when $w_e > 0$, $10^{-4} \text{ cm s}^{-1}$ when $w_e < 0$, there is no zero contour, and the maximum value of w_e off Somalia is $4.6 \times 10^{-2} \text{ cm s}^{-1}$. To indicate the areas where w_e is very nearly zero, the $w_e = 10^{-7} \text{ cm s}^{-1}$ contour is included and regions where $w_e \leq 10^{-7} \text{ cm s}^{-1}$ are shaded. There is strong upwelling off Somalia, Arabia and the west coast of India, h_m shallows to 35m in these regions, and Q is large and positive as a result of the upwelling of cool, subsurface water. The Somali Undercurrent reverses to flow northward, in order to provide a source of water for the upwelling off Somalia.

The region of shallow h_1 along the west coast of India has intensified and broadened since May. In fact, the front where h_1 shallows markedly is no longer coastally trapped, but is propagating offshore. A comparison of h_1 fields in subsequent months shows that this region continues to propagate westward throughout the year, with a considerably faster speed in the south than in the north; indeed, the relative minimum of h_1 in the central Arabian Sea (near 65°E , 10°N) results from the offshore propagation of the *previous* year's shallow region (compare successive h_1 panels of Fig. 2). Moreover, throughout the year the currents associated with this band of low h_1 tend to flow in opposite directions in the two layers (Figs 2a', 2b', 2d' and 2e'; this property is actually least apparent in Fig. 2b' because local forcing is so strong during the Southwest Monsoon). These features suggest that the band is a packet of mode-2, mid-latitude Rossby waves, and propagation speeds estimated from the solutions are close to those for these Rossby waves (see Section 2.5 and Table 1). In support of this propagation, ANTONY and UNNIKRISHNAN (1992) report the offshore movement of the west-coast upwelling front from July to September, and ANTONY, SHENOI, KRISHNA, MURTY, RAO, MURTY and SASTRY (1992) note the existence of reversing current bands in the Arabian Sea.

Changes that have occurred in the Bay of Bengal are most visible in the structure of h_1 , which shows further shallowing along the east coast of India and deepening along the eastern boundary of the Bay. Interestingly, the regions of shallowing and deepening "meet" along the east coast of India near 18°N , and geostrophically balanced coastal currents converge toward this point. This convergence indicates a "competition" between two opposing, driving mechanisms: local forcing by the winds, and remote forcing from the equator (see Section 4.1.3). A similar convergence was present in the observations reported by SHETYE *et al* (1991b), which indicated an abrupt end of the upwelling regime in the northern Bay: at the top of the Bay (near 20°N) there was little evidence of upwelling, with isopycnals sloping downward toward the coast, indicative of southwestward flow throughout the upper 500m.

The h_1 field now tilts upward to the south along the east coast of India, in contrast to the uniform shallowing present there in May. This tilt indicates that there is a southward pressure-gradient force in the upper layer which tends to balance the alongshore wind stress, a tilt that can only be established via the propagation of Kelvin waves along the coast. Note that the region of shallow h_1 (the 40m contour) wraps completely around the tip of India, another indication that the circulation on the west coast is to a large extent remotely forced. Like its shallow- h_1 counterpart along the west coast of India, the deepening along the eastern boundary of the Bay of Bengal propagates westward throughout the year at speeds consistent with those of a mode-2 Rossby wave (compare successive h_1 panels of Figs 2a-2e).

The near-equatorial circulation in the eastern Indian Ocean is more complex than it was in May, now consisting of *three* distinct currents. One of them is a strong, eastward jet just south of India that extends east and somewhat north into the Bay of Bengal near 5°N , the model Indian Monsoon Current, and a similar flow is also present in the ship-drift observations. The other two currents are a westward flow near the equator and a second eastward current located near 5°S , but there is little indication in the ship-drift data to support their existence. Two physical processes, both of which began in April and May, contribute to these near-equatorial changes. One is local forcing by wind curl, a process which is strongest in the southwestern Bay of Bengal (Section 4.1.2). This forcing causes h_1 to shallow north of the wind axis (as in May) and to deepen south of it; consistent with geostrophy, an eastward current is generated in the region where $h_{1y} < 0$, and a westward current is produced along the southern portion of the region of deeper h_1 where $h_{1y} > 0$. The other process is the westward propagation of the region of increased h_1 as a packet of equatorially trapped Rossby waves, which affects the currents more in the central and eastern Bay (Sections 4.1.2 and 4.1.3).

Note that the lower-layer currents associated with this signal are directed counter to the upper-layer currents (Fig. 2b'), identifying it to be a mode-2 wave. The leading edge of this feature is located near 85°E, 80°E, 75°E and 70°E in May, June, July and August respectively, yielding a propagation speed of only 21 cm s⁻¹ (compare successive v_1' panels of Figs 2a, 2b and 2c). This speed is considerably slower than that of a mode-2, first-meridional mode, equatorially trapped Rossby wave, namely $c_2/3=42$ cm s⁻¹, probably because the disturbance is slowed by the westward equatorial jet farther to the west.

Equatorially trapped Rossby waves like the one just described are a common feature in Indian-Ocean models, and there is observational support for their existence. In his analysis of current-meter data from Gan Island at 73°E, McPHADEN (1982) concluded that phase associated with semi-annual variations propagated *upward*, a certain indicator of the presence of a *downward*-propagating free wave. LUYTEN and ROEMMICH (1982) reported both upward and westward phase propagation along the equator in their equatorial current-meter array located from 47°E to 62°E, and concluded that a downward-propagating, first-meridional-mode, Rossby wave was present in their data. The equatorially trapped Rossby waves in our model do not exhibit vertical propagation because the model's vertical resolution is too limited; however, Rossby waves do begin to exhibit this property in an Indian-Ocean model with an additional layer (JENSEN, personal communication).

The near-equatorial currents in the western Indian Ocean differ considerably from the observations. In our solution, Arabian-Sea water flows across the equator to feed the Equatorial Countercurrent located just south of the equator. (A similar flow field is present in the GCM solution of ANDERSON *et al.*, 1991; see their Fig. 14.) In contrast, the ship-drift data indicates that this water flows eastward across the Arabian Sea near 5°N in the Indian Monsoon Current. Possible reasons for this discrepancy are discussed in Section 5.

Model SST has cooled markedly off Somalia, Arabia and near the southern tip of India. The plots of h_1 , h_m and w_e (Figs 2b and 2b') demonstrate that this cooling results from upwelling, in which h_1 shallows to the minimum thickness $h_{\min}=35$ m and generates entrainment w_e via the adjustment (6d). Most of the upwelling occurs adjacent to the coast via coastal Ekman divergence, but some happens in the open ocean west of the wind axis because of Ekman suction (SMITH and BOTTERO, 1977). The regions of lowest SST do not appear in our climatological SST field (lower-right panel of Fig. 2b). However, these regions *are* present in the climatology of HASTENRATH and LAMB (1979) apparently as a result of their using a smaller averaging grid (1°x1° rather than 2°x2°); they also exist in synoptic data.

Interestingly, the surface heat flux Q (lower-right panel of Fig. 2b') is *large and positive* in the upwelling regions where T_m has lowered considerably, a property consistent with estimates of Q using observed SST (RAO *et al.*, 1989, 1991; HASTENRATH and LAMB, 1979). One reason for this pattern is that the saturation specific humidity at the sea surface q_s drops with decreasing SST, thereby lowering the latent-heat loss Q_L from the ocean. The other reason is that the solar radiation is intensified near the Arabian coast because of reduced cloudiness (RAO *et al.*, 1989, 1991).

The mixed-layer topography h_m is shallow along the boundaries of the Arabian Sea and in the western Bay of Bengal; it is deep in the Arabian Sea south of the axis of maximum wind strength, and in the southern Bay of Bengal near 2°N (upper-right panel of Fig. 2b'). These large-scale features of h_m compare favorably with the climatological data (RAO *et al.*, 1989, 1991). There is a relative minimum of h_m in the central Arabian Sea that results from Rossby-wave propagation of the shallow- h_1 region from the Indian coast, as discussed above. Another relative minimum in the western Arabian Sea (near 52.5°E, 6°N) results from the offshore advection of cool SST around the flank of the Southern Gyre; as a consequence, Q is positive there and both w_K and w_e are negative (lower panels of Fig. 2b').

3.1.3. September: The southwest Monsoon is weakening in September, but except for a few notable differences the flow field is still much like the one in July. One obvious difference is that SST warms off Somalia, Arabia and the southern tip of India because of weakened upwelling (middle- and lower-right panels of Fig.2c). In the Arabian Sea, the model Southern Gyre moved northward along the Somali coast during August. In September, there is only a rather poorly formed gyre centered near 10°N , visible in both the h_1 and v_1 fields. Synoptic observations suggest that this northward movement often occurs in the real ocean, and the Southern Gyre eventually coalesces with the Great Whirl (EVANS and BROWN, 1981).

As in July, a strong eastward current south of India and Sri Lanka is present in both the model and ship-drift observations, and this flow extends across the interior of the Bay of Bengal. In addition, the solution still has southward flow in the southern Arabian Sea, whereas the observations show the eastward-flowing Indian Monsoon Current. The northward current along the east coast of India is now absent or reversed (south of about 12°N), and as a result the flow in the western Bay appears more disorganized than it did in July (middle- and lower-left panels of Fig.2c; SHETYE and SHENOL, 1988). The disappearance of this current is reflected in the structure of h_1 , which no longer shallows anywhere toward the east coast of India (isolines bend southward toward the east coast in the shaded region north of Sri Lanka). The reason for this change since July is that the alongshore wind has weakened roughly by a factor of 2, and hence the upward slope of h_1 southward along the coast is less. As a consequence, the remotely forced signal from the equator overwhelms the locally forced response (Section 4.1.3).

3.1.4. November: The Southwest Monsoon collapses in October, and at that time the strongest winds anywhere in the northern ocean are westerlies located near and just north of the equator from about 60 to 90°E . In November northeasterly winds appear in the Arabian Sea and the Bay of Bengal, marking the beginning of the Northeast Monsoon. The northeasterlies are not yet strong enough, nor have they been blowing long enough, to modify the circulation in any obvious manner. Note, for example, that north of 5°N both the model and observed Somali Currents have weakened from their September strengths, but are still flowing northward directly into the wind. Much of the Somali Current now bends offshore south of 5°N producing a circulation pattern like that associated with the Southern Gyre in May (middle- and lower-left panels of Fig.2d). SCHOTT and FIEUX (1985) report a similar reformation based on synoptic observations.

There is now a southward Somali Undercurrent extending from the tip of Somalia down to 3°N that is fed by a westward flow across the interior of the northwestern Arabian Sea (Fig.2d'). This flow appeared in October with the weakening of the Southwest Monsoon winds, and it lasts through February. It is evident that it is a geostrophically balanced current circulating about a band of deep h_1 in a direction opposite to that of the upper-layer currents (a mode-2 response), and this close relationship between v_2' and h_1 holds throughout its existence. In fact, a measure of the strength of the undercurrent is the value of $|\nabla h_1|$ near the coast, which is strongest in November and December, but has essentially disappeared by March (compare the upper-right panels of Figs 2c-2f). The band of high h_1 was generated by Ekman pumping during the Southwest Monsoon off the Somali coast, and it propagated westward as a Rossby wave with the weakening of the winds. Thus, this fall Somali Undercurrent is really a remnant from the previous summer. Local forcing by the northeasterly winds does help to strengthen this flow in December and January, but negative wind curl north of the wind axis weakens the current in February and reverses it in March (Section 4.1.1). Consistent with our solution, ANDERSON *et al* (1991) noted that a Somali Undercurrent was present in their solution during November, but they did not discuss its cause. Current-meter observations at 5°N indicate that southwestward, subsurface flow reappears considerably earlier in August (QUADFASSEL and SCHOTT, 1983), a difference possibly resulting from our model's limited vertical resolution.

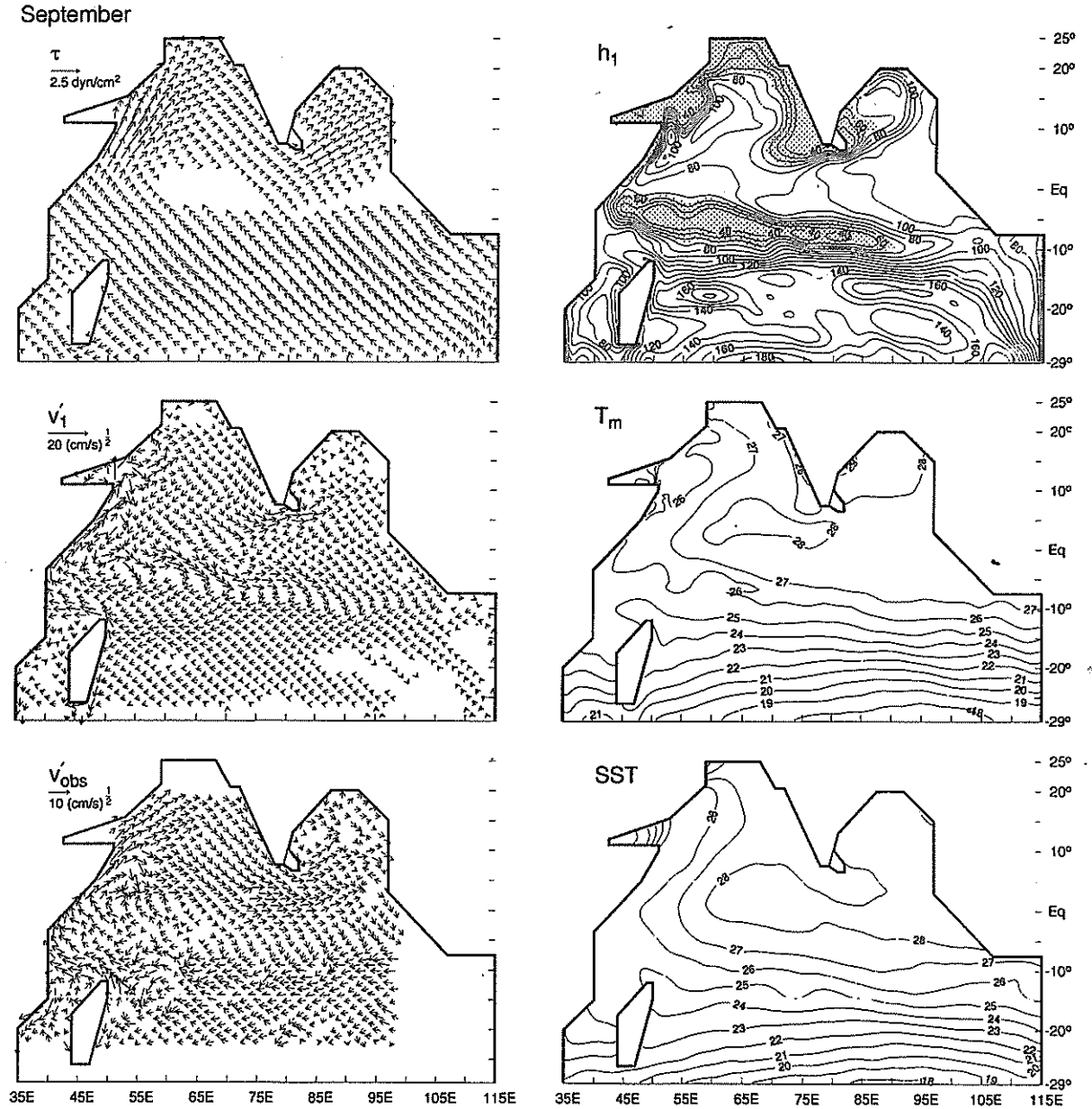


Fig.2c. As in Fig.2a, except in September. The circulation is generally similar to that in July. The model Southern Gyre has moved northward along the Somali coast, and only a weak gyre remains near 12°N . In response to the weakened alongshore winds, the tilt of h_1 along the east coast of India is much less and the northward coastal current there vanishes. Weakened upwelling leads to SST warming off Somalia, Arabia and the Indian Ocean.

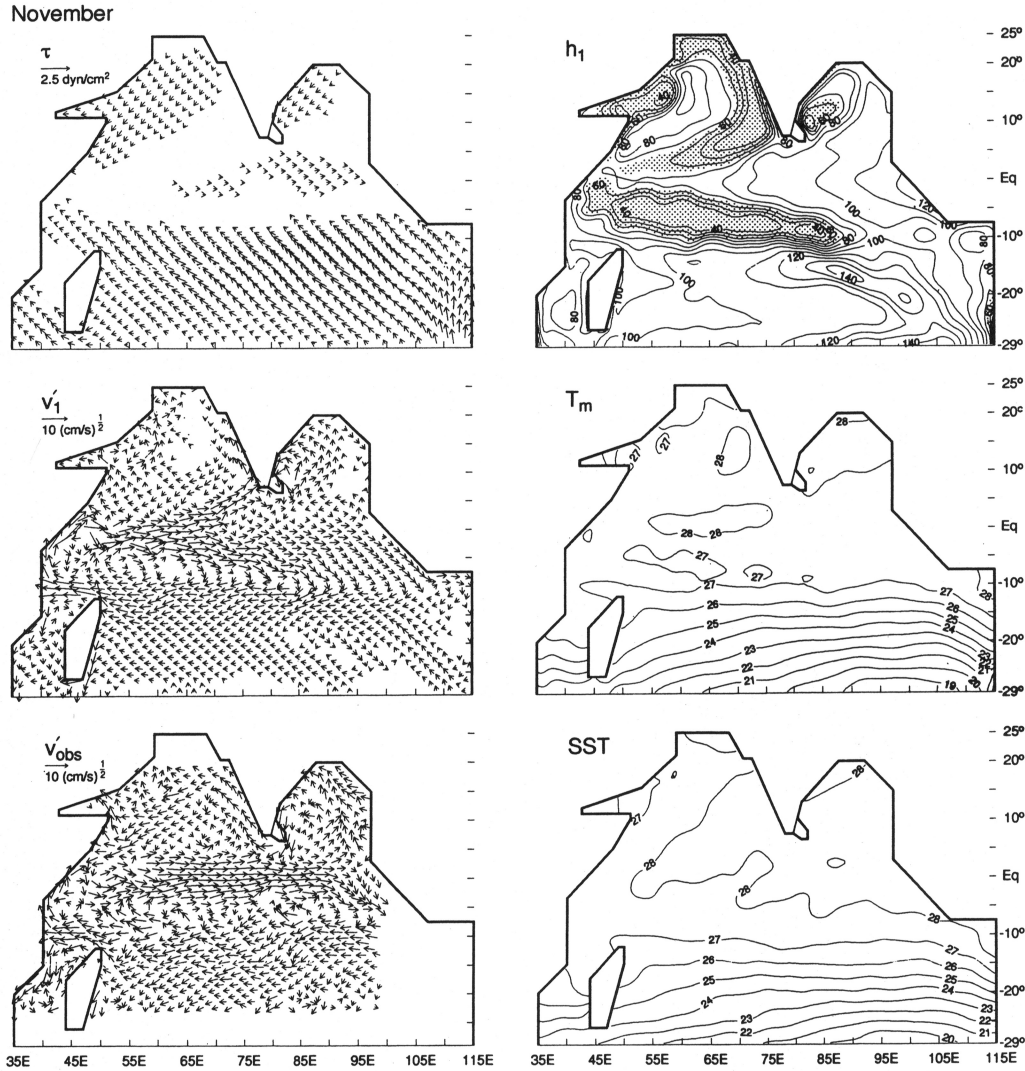


Fig.2d. As in Fig.2a, except in November. The collapse of the Southwest-Monsoon winds in the Bay of Bengal results in h_1 deepening along both coasts of India. As a consequence, there are southward and northward currents on the east and west coasts of India, respectively, and the model Indian Monsoon Current flows northwestward to intersect the west coast of India. There is no fall Wyrtki jet, a major failing of the model.

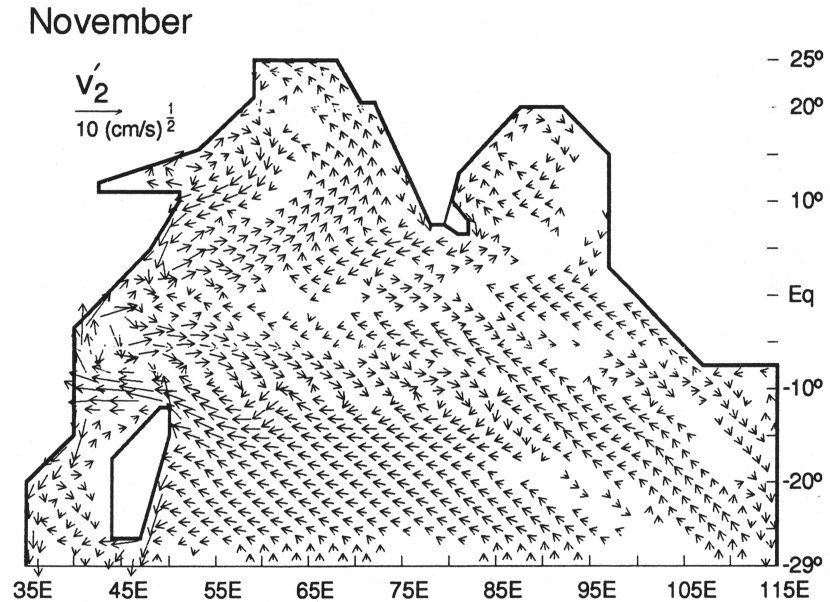


Fig. 2d'. As in Fig. 2d, except showing the lower-layer current v'_2 for the main run. There is a southward Somali Undercurrent from the tip of Somalia to 2.5°N , circulating about a band of high h_1 (upper-right panel of Fig. 2d). There is a southward undercurrent along the west coast of India.

Another remarkable change in the solution is that a northward surface current and a southward undercurrent (Fig. 2d') are now present along the west coast of India as far north as 20°N , and these currents are obviously not forced by the local winds which are very weak. In addition, a southward surface current now exists everywhere along the east coast of India, intensifying to the south. Both of these changes result from the collapse of the winds in the Bay of Bengal as follows (also see Section 4.1.2). The absence of upwelling-favorable alongshore winds leads to the tilt of h_1 vanishing completely along the east coast of India via the propagation of coastal Kelvin waves. As a result, h_1 deepens everywhere along the east coast to its value in the north, with h_1 increasing at the tip of India from its September value of 35m to 85m. This deepening propagates poleward along the west coast as a packet of coastal Kelvin waves, generating the geostrophically balanced, northward, coastal flow.

Consistent with the solution, ship-drift observations along the east coast of India show southward flow from September through January, reaching a peak strength in November and with current speeds decreasing northward along the coast (Figs 2c-2e; SHETYE and SHENOI, 1988). Along the west coast, ship drifts show a northward current from November through January (SHETYE and SHENOI, 1988; RAO *et al.*, 1989, 1991), and satellite images reveal that the current develops first in the south and then spreads northward (SHENOI, GOUVEIA, SHETYE and RAO, 1992). Near-surface isotherms slope downward toward the west coast at this time (JOHANNESSEN *et al.*, 1981), and dynamic-height calculations indicate a poleward surface current and an equatorward coastal undercurrent at 300db (SHETYE, GOUVEIA, SHENOI, MICHAEL, SUNDAR, ALMEIDA and SANTANAM, 1991a). JOHANNESSEN *et al.* (1981) suggested that salinity variations

caused by river runoff were the driving mechanism for these west-coast flows. SHETYE and SHENOI (1988) and SHETYE *et al* (1991a) proposed an alternate thermohaline process, suggesting that the observed northward salinity increase across the interior of the Arabian Sea generates a poleward sea-level drop that drives the coastal currents, a process illustrated in the theoretical study of MCCREARY, SHETYE and KUNDU (1986). Our model demonstrates that remote forcing from the east coast of India may be a more important mechanism for the west coast circulation.

The eastward current south of India in September, the model Indian Monsoon Current, now flows to the northeast to intersect the tip of India. The reason for this change is also the deepening of h_1 at the tip of India, which weakens (or reverses) the geostrophically balanced, eastward current. A weakening, and even reversal, of the Indian Monsoon Current is also present in the ship-drift observations, and there is a suggestion of a northeastward current into the west coast of India (lower-left panel of Fig. 2d).

In response to strengthened, near-equatorial westerlies, the westward equatorial current present in the solution in September weakens in October, but it does not reverse. By November there is eastward flow along the equator, but it is mostly confined to the western ocean near 60°E. This behavior contrasts with the ship-drift observations which show a strong eastward current everywhere along the equator during both October and November, the fall Wyrtki jet (lower-left panel of Fig. 2d). This discrepancy is a major failing of the model, and possible reasons for it are discussed in Section 5.

3.1.5. January: The Northeast Monsoon reaches its peak strength in January. In the Arabian Sea the winds are strongest off Somalia near the equator, and in response a strong, southward coastal current develops in the upper layer along most of the Somali coast across the equator to 2.5°S. Interestingly, the western-boundary flow in the lower layer remains northward up to about 2.5°N, forming a cross-equatorial, coastal undercurrent that persists through February (upper-left panel of Fig. 2e'). This feature is consistent with the current-meter data reported by SCHOTT (1986) and SCHOTT, SWALLOW and FIEUX (1990), which also show that a northward undercurrent is present below about 100m during the winter, but in contrast to our solution the observed flow does not weaken until April. Unfortunately, we have been unable to diagnose the cause of the model undercurrent. A plausible explanation is that it results from the inertial overshoot of the western-boundary current, but a close look at the v_2 field (closer than allowed by Fig. 2e') reveals that most of the flow bends offshore just south of the equator. Moreover, the three test calculations in Section 4.1 that neglect the Arabian-Sea winds also provide few clues into its dynamics: the undercurrent remains in all three tests, preventing a conclusion as to whether the flow is primarily remotely or locally forced. It is likely that this undercurrent has more than a single cause in the model.

A prominent feature of the h_1 field in the southern Arabian Sea is a band of shallow h_1 that extends across the basin at roughly 5°N. This band is partly a remnant of the region of shallow h_1 generated along the west coast of India during the Southwest Monsoon, which subsequently has propagated westward as a Rossby wave (see Sections 3.1.1 and 4.1.1). It is also being locally forced by Ekman pumping, which tends to move water from southeast to northwest of the wind axis. The region of low h_1 centered near 53°E, 3°N, results primarily from this latter process; note that the upper-layer flow circulates about this region, and that there are suggestions of a similar circulation in the ship-drift data. An indication of the strength of the Ekman suction in this low- h_1 band is the existence of entrainment, showing that h_1 has shallowed to h_{\min} (h_1 , h_m and w_e panels in Figs 2e and 2e'). Two other features are a band of high h_1 located just north of the low- h_1 band, and a region of shallow h_1 at the mouth of the Gulf of Aden (near 53°E, 12°N). Both of them are remnants from the Southwest Monsoon (Section 4.1.1) that are deepening through Ekman convergence.

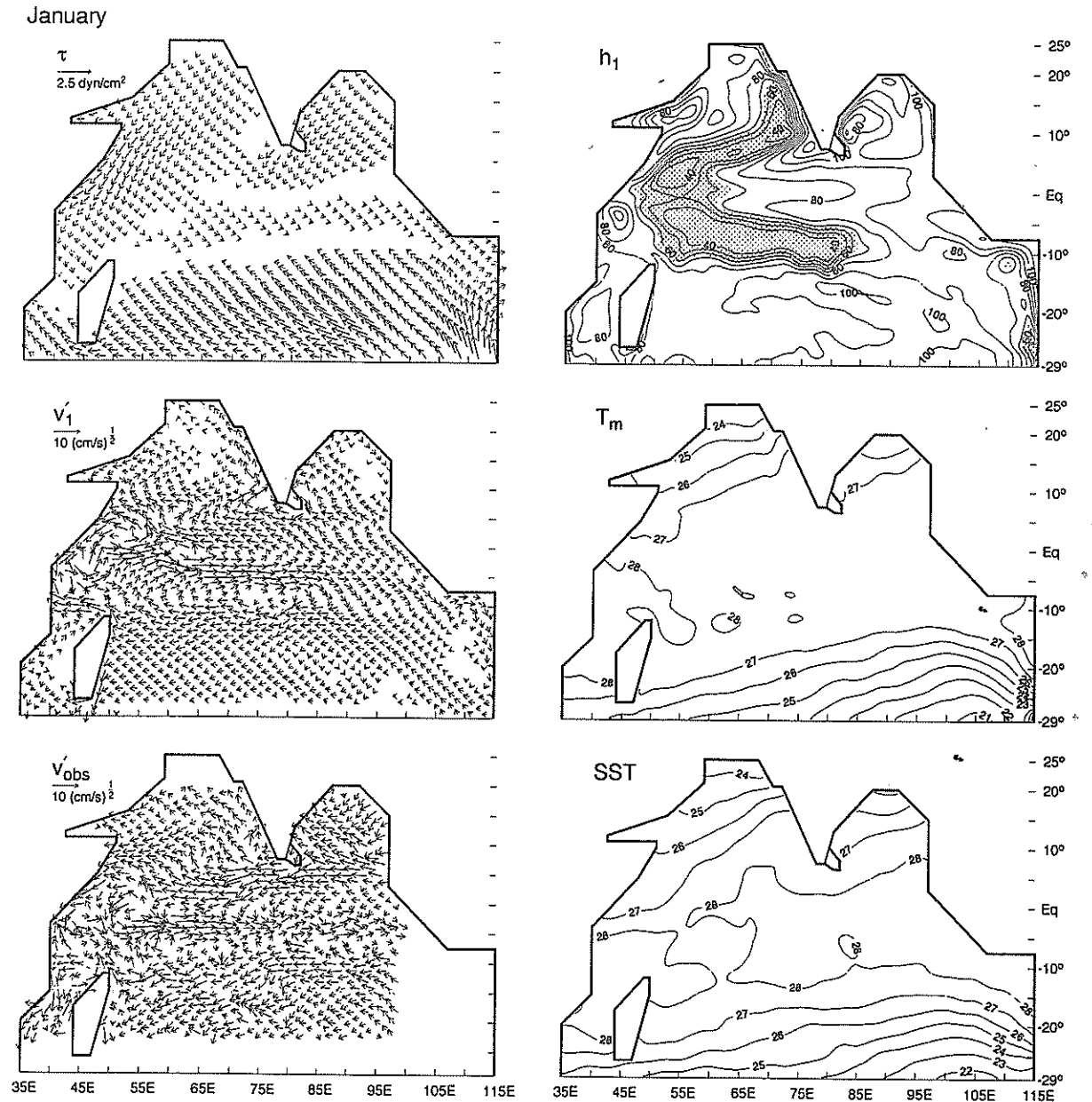


Fig. 2e. As in Fig. 2a, except in January. In response to the local winds the Somali Current flows southward south of about 9°N . Alternating bands of low and high h_1 , and associated geostrophic currents, stretch across the interior of the Arabian Sea. The h_1 field is particularly shallow offshore of Somalia due to Ekman pumping, and the upper-layer current circulates cyclonically about this feature. The northward current along the west coast of India is stronger and broader than in November. There is a countercurrent along the east coast of India north of about 15°N . There is now westward flow nearly everywhere along and north of the equator in both the model and ship-drift observations. SST is cool in the northern Arabian Sea and Bay of Bengal, primarily as a result of latent-heat loss through the ocean surface.

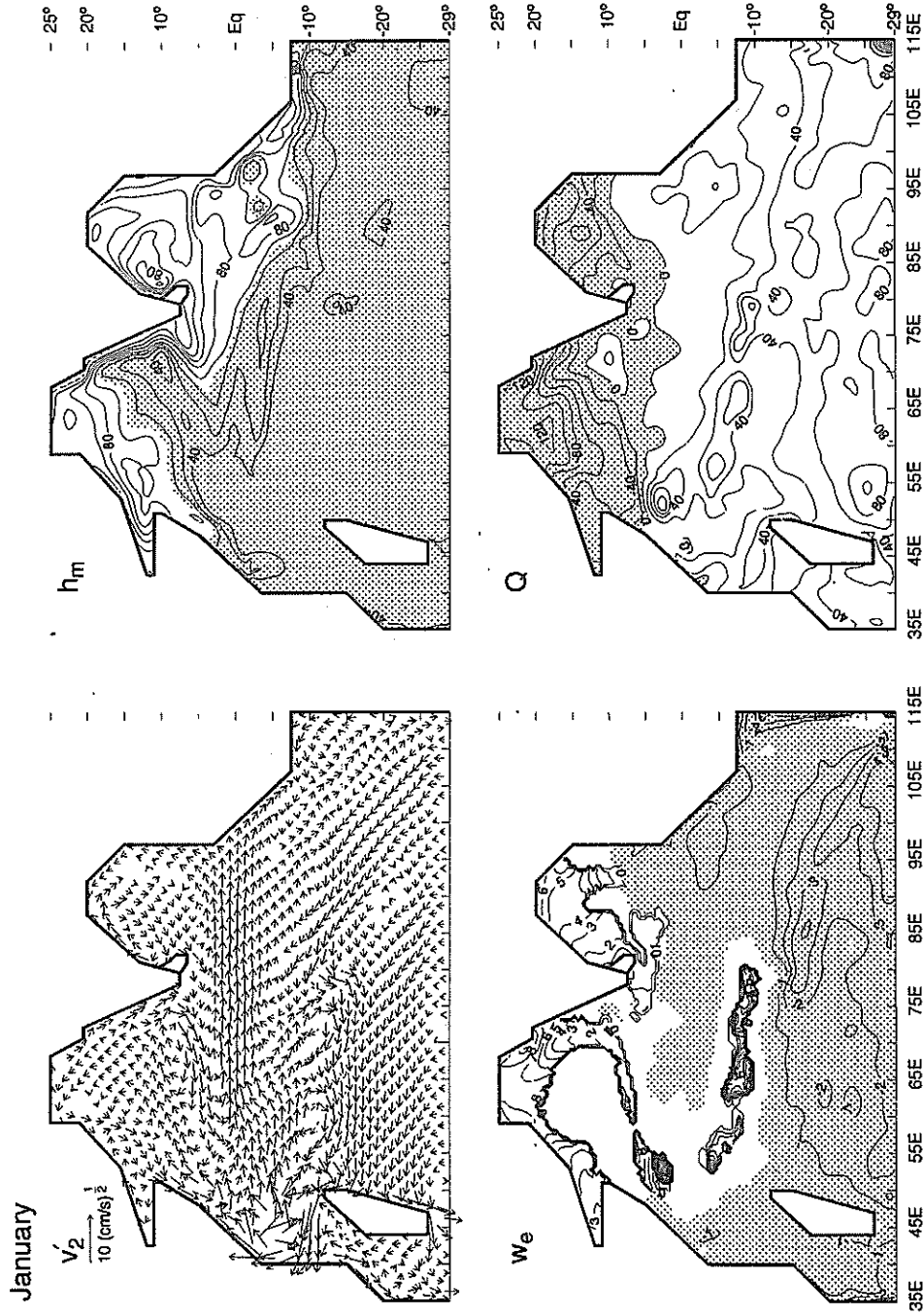


Fig.2e'. As in Fig.2b', except for January and the contour interval for w_e is $10^{-4} \text{ cm s}^{-1}$ for both positive and negative w_e . The maximum value of w_e offshore of Somalia is $2.4 \times 10^{-3} \text{ cm s}^{-1}$. The Somali Undercurrent flows southward from the tip of Somalia to 2.5°N , and there is a northward western-boundary undercurrent that crosses the equator. The southward undercurrent along the west coast of India is stronger and broader than it was in November. There is an eastward Equatorial Undercurrent. Because the winds of the Northeast Monsoon are cool and dry, Q is large and negative in the northern Arabian Sea and Bay of Bengal, there is entrainment by convective overturning, and the mixed layer deepens to 100m or more.

There is a distinctive westward current across the interior of the Arabian Sea from about 7°N to 10°N located between the bands of shallow and deep h_1 where $h_{1y} > 0$, and a similar westward flow is present in the ship-drift observations (lower-left panel of Fig. 2e). This current reaches the Somali Coast near 8°N , and most of it bends southward to provide part of the water for the southward-flowing Somali Current; the rest circulates about the western edge of the high- h_1 band to form a weak northward, coastal countercurrent. This countercurrent was already present in November, a consequence of forcing during the Southwest Monsoon; it is now weaker because of the strong northeasterly winds, but reappears in the spring (see Sections 3.1.5 and 4.1.1). ANDERSON *et al* (1991) report a similar countercurrent in their GCM solution (see their Fig. 13a), commenting that it is the last vestige of the Great Whirl that formed 6 months earlier.

The northward current and southward undercurrent along the west coast of India are both stronger than they were in November. Note that the thickness of the upper layer has now increased to 110 m or more along the west coast, even though the local alongshore winds are still very weak, supporting the notion that the coastal circulation is remotely forced by the corresponding increase in h_1 along the east coast of India. Both currents are also broader than in November, especially to the south, as a result of offshore propagation of mode-2 Rossby waves (the lower-layer flow is directed oppositely to the surface current), and a similar broadening occurs in the observations (SHETYE *et al*, 1991a).

In the Bay of Bengal, the wind axis has shifted southeastward to intersect Sri Lanka, and so there is now negative wind curl throughout the western Bay. As a consequence, Ekman pumping acts to deepen h_1 there, particularly in the region of shallow h_1 in the southwestern Bay (compare h_1 panels of Figs 2d and 2e). North of 15°N the current along the east coast of India reverses to flow northward into the wind, and there are indications of this countercurrent in the ship-drift data. The countercurrent strengthens in the spring, and its possible causes are discussed in Sections 3.1.6, 4.1.2 and 4.1.3.

There are now westward surface flows nearly everywhere along and north of the equator in the solution, the model North Equatorial Current, and similar currents are also present in the ship-drift data. There is an eastward undercurrent centered on the equator that extends to the eastern boundary of the basin, where it divides to flow north and south (Fig. 2e'). The existence of these currents is reflected in the structure of h_1 , which rises in a narrow band centered somewhat north of the equator. These features are even more pronounced in February (not shown) and still occur in March (Fig. 2f). Three processes contribute to these changes. The most influential process in the southern Bay of Bengal is local forcing by Ekman pumping; it causes h_1 to shallow south of the wind axis and to deepen north of it so that $h_{1y} > 0$, thereby generating a westward upper-layer current (see Section 4.2). The important process in the southwestern Arabian Sea is the westward radiation of downwelling, mode-2, Rossby waves from the west coast of India, which also generates a region where $h_{1y} > 0$ along its southern edge. The third process is remote forcing via an upwelling-favorable, mode-2, equatorial Kelvin wave and its reflection from the eastern boundary as a packet of Rossby waves, although at this time the effects of this wave packet are most clearly identifiable in the structure of the lower-layer flow field. This Kelvin wave is generated by the strengthened easterly component of the winds in the western and central oceans: the system responds by piling up upper-layer water in the western ocean, and the radiation of the Kelvin wave establishes a westward equatorial current that is the source for the additional upper-layer water.

The northeasterly winds carry cool, dry, continental air over the northern Arabian Sea and Bay of Bengal, and hence there is a large latent-heat loss from the ocean in these regions (lower-right panel of Fig. 2e'; Section 4.2). In response, mixed-layer temperatures T_m drop nearly to their lowest seasonal values (which occur in February), reaching minima of about 23°C in the northern Arabian

Sea and 25.5°C in the northern Bay of Bengal. Generally, model SST compares well with climatological data in the Arabian Sea, but not in the northern Bay of Bengal which actually cools further to a minimum <24°C (lower-right panel of Fig.2e; HASTENRATH and LAMB 1979). Another discrepancy is that the amplitude of the cooling in the model Q field is considerably larger than estimates of Q using climatological SST (HASTENRATH and LAMB, 1979; RAO *et al.*, 1989, 1991). The implication is that SST is not cooling rapidly enough in the model, possibly for the reason discussed next.

Also in response to the surface cooling, h_m (and h_l) deepens considerably in the northern Arabian Sea and Bay of Bengal through entrainment caused by convective mixing (w_e , h_m and Q panels in Fig.2e'). Consistent with the solution, the analysis of RAO *et al.* (1989, 1991) also shows wintertime, mixed-layer depths of the order of 100m there. There is, however, little indication of such thick mixed layers in synoptic observations from the Bay of Bengal. Instead, there is a fresh, surface layer caused by intense rainfall and river runoff from earlier in the year, and there can be temperature inversions across this layer of the order of 2°C (SHETYE, personal communication; SPRINTALL and TOMCZAK, 1992). (Apparently, these temperature inversions "trick" the algorithm used by RAO *et al.*, 1989, 1991, into estimating mixed-layer depths that are too large.) The resulting large density difference across the base of the mixed layer inhibits entrainment, thereby preventing the mixed layer from deepening rapidly. The fact that the mixed layer is too thick in the solution may be the cause for the insufficient cooling noted in the previous paragraph (at least in the northern Bay of Bengal): in a model that includes salinity, the mixed layer would be thinner and T_m would be able to cool more rapidly.

3.1.6. March: The Northeast Monsoon has weakened considerably by this time, and most of the circulations in the northern ocean are remnants of flows that were generated earlier. There are still northeasterly winds off Somalia and a southward flow extending from about 5°N across the equator to 2.5°S. The bands of low and high h_l are associated with the same westward current near 8°N as they were in January. The model North Equatorial Current is a second, and stronger, westward flow across the Arabian Sea; consistent with the ship-drift observations, it is centered near 3°N and splits at Africa to flow along the Somali Coast. This flow is primarily caused by the propagation of a region of deep h_l from the coast of India via mode-2 Rossby waves (the second of the three processes discussed in Section 3.1.5); as a consequence, there is now a region where $h_{ly} > 0$ along the southern edge of this region all across the Arabian Sea (compare the h_l panels of Figs 2e and 2f). The westward equatorial jet established by the propagation of the downwelling Kelvin wave (the third process discussed in Section 3.1.5) also contributes, as evidenced by the shallowing of h_l in the eastern, equatorial ocean. Note that both of these processes have acted to eliminate the region of low h_l (near 53°E, 3°N) and the associated cyclonic circulation about it that was present in January.

North of about 4°N the model Somali Current now flows *northward* directly into the wind. In agreement with the model, LEETMAA *et al.*, (1982) reported that during March and April of 1979 the Somali Current was flowing northeastwards north of 4°N. The existence of this countercurrent is corroborated in the ship-drift observations (lower-left panel of Fig.2f). Moreover, a similar countercurrent also developed in the ANDERSON *et al.* (1991) solution (see their Fig.13c). QUADFASSEL and SCHOTT (1983) suggested that the observed countercurrent was forced by local wind curl, and test calculations reported in Section 4.1.1 indicate that this process does contribute to the model countercurrent. However, the tests also show that remote forcing from the previous Southwest Monsoon is an important driving mechanism; thus, the countercurrent in March is in part the same one that was present in November and January, stronger now because the retarding winds of the Northeast Monsoon have weakened.

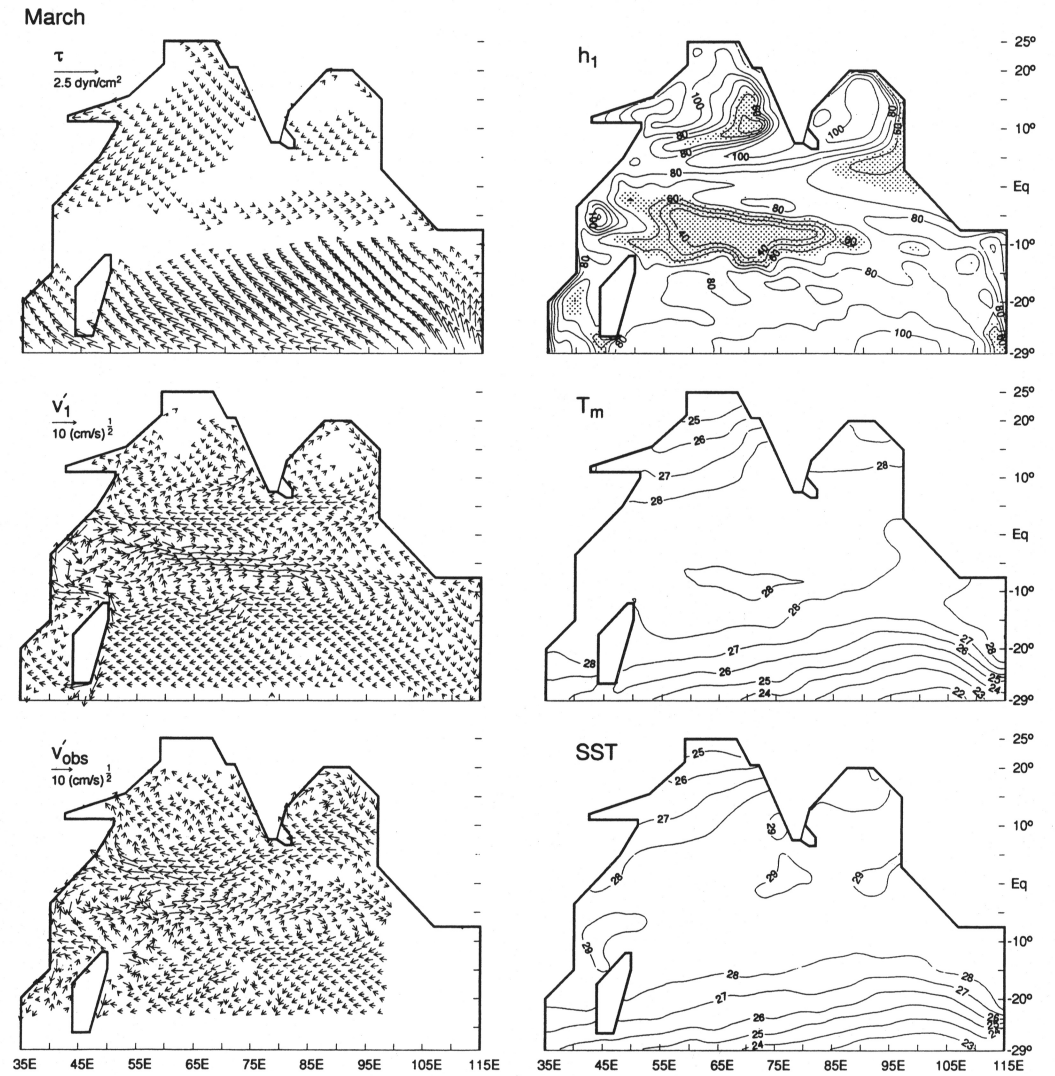


Fig.2f. As in Fig.2a, except for March. There is a westward current across the Arabian Sea at 3°N that splits at the Somali coast. North of 5°N the model Somali Current flows northward against the wind, and a similar countercurrent is present in the ship-drift observations. The region of low h_1 in the southwestern corner of the Bay of Bengal in January is nearly gone, a result of Ekman pumping.

The alongshore current flows northward everywhere along the west coast of India.

The model flow field near the west coast of India is similar to, but weaker than, that in January, consisting of a northeastward current into the coast near 10°N that turns to flow primarily northward. In contrast, the ship-drift currents have reversed from January to flow southward along the coast, apparently in response to the upwelling-favorable local winds. Indeed, there are indications of active upwelling along this coast as early as February and March (RAO, CHERIAN, VARMA and VARADACHARI, 1974; SHETYE, 1984). The reason for this discrepancy between modelled and observed flows is unclear. A likely possibility is that at this time the upper layer is too thick ($>100\text{m}$) to enable a shallow, locally forced coastal jet to be resolved.

Ekman pumping has led to the virtual disappearance of the region of low h_1 in the southwestern corner of the Bay of Bengal (near 72.5°E , 11°N), as well as the cyclonic circulation about it. Traces of the cyclonic circulation present in January persists, the weak northeastward current through the center of the Bay being an example. A similar northeastward current was present in the satellite images reported by LEGECKIS (1987). Both the solution and the ship-drift observations indicate that a northward current extends all along the east coast of India, and this flow lasts until August (Figs 2a, 2b and 2f; SHETYE and SHENOI, 1988; SHETYE, GOUVEIA, SHENOI, SUNDAR, MICHAEL and NAMPOOTHORI, 1992). As discussed in Section 3.1.1, by May this current is certainly influenced by the local, upwelling-favorable, alongshore winds. However, the fact that it first appears in January (Section 3.1.5) and is well established in March, long before the onset of the Southwest Monsoon, indicates that remote forcing is responsible for its initial development. The structure of the h_1 field, with a region of low h_1 extending from the equator around the perimeter of the Bay, suggests that remote forcing from the equator is an important process (see Section 3.1.5). SHETYE *et al* (1992) proposed the alternate idea that its dynamics are those of a classical western-boundary current, in which the current is remotely driven by negative wind curl in the western Bay via the westward propagation of Rossby waves. A third possibility is remote forcing by alongshore winds elsewhere in the Bay. In Sections 4.1.2 and 4.1.3 we discuss the relative importance of these three processes, and demonstrate that the first process does not account for the reversal.

As in January, there is still an eastward, lower-layer current along the equator (not shown). Only in January, February and March does the solution have a structure with surface westward flow and subsurface eastward flow, as in the "classical" Equatorial Undercurrent (EUC). Its dynamics, however, are very different from those of the permanent undercurrents in the Pacific and Atlantic Oceans, being a transient response associated with the propagation of mode-2, equatorially trapped waves (see Section 3.1.5). Another indication of its different dynamics is the absence of equatorial upwelling, a key property of the permanent undercurrents in the other oceans. There is observational support for the existence of an Indian-Ocean EUC only during the spring. For instance, SWALLOW (1967) reported the existence of a shallow EUC in March, 1964, at 58°E and 67.5°N , but by April the surface-layer flow reversed (the springtime Wyrtki jet) and the "classical" EUC vanished. Similarly, at Gan Island near 73°E KNOX (1976) reported an EUC with westward surface flow only in March, 1973, but no such EUC occurred in the spring of 1974.

3.1.7. The southern Indian Ocean: Both the winds and the currents in the southern Indian Ocean are much less variable than in the northern ocean, a consequence of the absence of reversing monsoon winds. Both the model and observed circulations consist of a basin-wide cyclonic gyre (the Tropical Gyre) driven by wind curl over the interior ocean associated with the southern-hemisphere trades (WOODBURY *et al*, 1989). The gyre is comprised of a broad southward flow in the ocean interior, westward flow south of about 10°S (the South Equatorial Current), northward western-boundary currents off Africa (the East African Coastal Current) and Madagascar, and usually an eastward current just south of the equator (the Equatorial Countercurrent). A

comparison of all the current panels of Fig. 2 shows that, except for the Equatorial Countercurrent, the structure of the Tropical Gyre does not vary much throughout the year, with its center (defined, say, by the line where the zonal flow vanishes) shifting meridionally by only a few degrees. (See WOODBURY *et al.*, 1989, and PERIGAUD and DELECLUSE, 1992 for detailed discussions of the variability that is present in the southern ocean.) The Equatorial Countercurrent is more variable because the near-equatorial ocean also responds rapidly and intensely to the equatorial, zonal wind field. The Equatorial Countercurrent is always present in the solution, but it is absent in the ship-drift and buoy (MOLINARI *et al.*, 1990) data from July through September, at which time the Tropical Gyre is closed north of the equator by the Indian Monsoon Current. Possible reasons for this discrepancy are discussed in Section 5.

Consistent with the ship-drift climatology (Fig. 2) and other observations (SWALLOW, FIEUX and SCHOTT, 1988; SCHOTT, FIEUX, KINDLE, SWALLOW and ZANTOPP, 1988), the model South Equatorial Current splits at the coast of Madagascar near 18°S. South of 18°S the circulation forms the anticyclonic Subtropical Gyre, only the northern portion of which is visible in the current plots. Much of the southward-flowing branch of the Madagascar coastal current (the East Madagascar Current) flows out of the basin through the open boundary, but some of it also flows to the African Coast to leave the basin in the model Agulhas Current, the two flows being western-boundary currents for the Subtropical Gyre. The model Agulhas Current tends to be weaker than observed throughout the year, and it even reverses north of about 25°S from February through May (Figs 2a and 2f). As we shall see in Section 4.4, when Pacific-Ocean throughflow is included southward flow is strengthened enough to overcome this deficiency, suggesting that the throughflow may in fact be an important remote-forcing mechanism of the real Agulhas Current.

It should be noted that there is no Leeuwin Current in our solution, and the reason for its absence is unclear. One possibility is that the solution has no throughflow from the Pacific Ocean; however, that hypothesis is not supported by our solution with throughflow which develops only a weak Leeuwin Current (Section 4.4). A second possibility is the lack of salinity effects in the model. In the McCREARY *et al.* (1986) model, the Leeuwin Current is a thermohaline flow driven by the poleward decrease in SST across the southern Indian Ocean: this decrease causes a poleward drop in the near-surface dynamic height field (HASTENRATH and GREISCHAR, 1989; GODFREY and RIDGWAY, 1985), which is associated with an eastward geostrophic flow that bends southward at the Australian coast to form the Leeuwin Current. In the real ocean, the dynamic-height drop is strengthened by a poleward increase in sea-surface salinity. A third possibility, if the McCREARY *et al.* (1986) explanation is correct, is simply that our model domain does not extend far enough south into the region where the dynamic-height field drops significantly.

Modelled and observed SST fields in the southern Indian Ocean are in remarkably good agreement throughout the year, generally differing by less than 0.5–1.0°C. Because there are no upwelling regions in the solution south of about 15°S, T_m is determined almost entirely by the surface heat fluxes (lower-right panels of Figs 2b' and 2e'), being warmest in February and coolest in September. In contrast, there is a broad area of upwelling in the interior ocean from 2.5°S–14°S forced by negative wind curl, and h_1 shallows to less than 40m there during every month of the year. This upwelling is considerably weaker than the maximum off Somalia (with maximum values of the order of $3 \times 10^{-3} \text{ cm s}^{-1}$ as compared to $46 \times 10^{-3} \text{ cm s}^{-1}$ off Somalia in July), and so it has a smaller effect on T_m , primarily acting to distort the isotherms away from climatological values (compare, for example, the middle- and lower-right panels in Fig. 2b). In agreement with the solution, a region of shallow h_1 does exist from 2.5°S to 14°S in climatological maps of the 20°-isotherm depth (RAO *et al.*, 1989, 1991), but there is no evidence in the climatological SST field of significant upwelling.

The mixed layer deepens rapidly as a result of entrainment induced by convective overturning

during the southern-hemisphere winter when $Q < 0$ and w'_K in equations (6) is positive. An indication of the strength of this entrainment is that $h_m = h_l$ over much of the southern Indian Ocean from June through August (see the h_l , w_e and h_m panels in Figs 2b and 2b'), so that the model is in a state like that in Fig. 1b. Another indication is that h_l deepens markedly in the south at this time, reaching a maximum thickness $> 180\text{m}$ in September (upper-right panel in Fig. 2c). A similar deepening also occurs in the climatological observations, with the mixed layer attaining thickness of 130–140m in August and September RAO *et al* (1989, 1991).

The mixed layer shallows during the southern-hemisphere summer when $Q > 0$ and $w'_K < 0$, and from November through February it is at its minimum thickness of 35m throughout most of the southern Indian Ocean (contrast the h_l and h_m panels in Figs 2e and 2e'). According to (7), at this time water detrains from the upper layer (see the w_e panel of Fig. 2e'), and by February and March h_l has shallowed to less than 100m over most of the southern Indian Ocean. As discussed next, this is a crucial process in the model that allows the solution to develop meridional circulation cells.

3.2 The annual-mean circulation

3.2.1. Description of the annual-mean fields: Figures 3 and 3' show the annual-mean fields for the main run. In the northern ocean the mean wind stress is dominated by the stronger forcing of the Southwest Monsoon, and the upper-layer circulation reflects this property, with the currents off Somalia and the east coast of India flowing northward. In the southern ocean the prominent flow is the clockwise Tropical Gyre. Note that its northern branch (the Equatorial Countercurrent) extends north of the equator in the upper layer, particularly in the central ocean. This northern part is driven by wind curl in the northern ocean, rather than by the southern-hemisphere trades, and therefore dynamically is not really part of the Tropical Gyre. Note also that the Equatorial Countercurrent is located farther to the south in the lower layer (compare the v'_1 and v'_2 panels in Figs 3 and 3'). In fact, it is dynamically interesting that there is *any* mean flow at all in the lower layer: in a linear model without entrainment and detrainment processes, the mean circulation is necessarily a Sverdrup flow confined to the upper layer. (See GODFREY, 1989, for a discussion of the Sverdrup circulation in the Indian Ocean.) The importance of entrainment in generating the lower-layer Equatorial Countercurrent is apparent in that it exists only in a region where w_e is large (compare the upper- and lower-left panels in Fig. 3').

The \bar{w}_e field is large and positive along the coasts of Somalia, Arabia and near the tip of India because of summertime upwelling, weakly positive in the northern Arabian Sea and Bay of Bengal as a result of wintertime convection, and negative near 10°N in the Arabian Sea because of the deepening of h_l during the Southwest Monsoon by Ekman pumping. (Curiously, there is little indication in the \bar{T}_m , \bar{h}_m and \bar{h}_l fields of the summertime upwelling events in the northern ocean, apparently because of their relatively short duration.) The \bar{w}_e field is also positive in the interior ocean from 2.5°S to 14°S where Ekman suction raises h_l to its minimum value of 35m throughout the year. It is *negative* nearly everywhere south of 15°S , so that entrainment during the southern-hemisphere winter (Fig. 2b') is more than compensated by summertime subduction (Fig. 2e').

Prominent features in the model's annual-mean heat flux \bar{Q} field are: intensified heating near the coasts of Somalia, Arabia and India, a band of heating extending across the western ocean near 5°S , and cooling in the southeastern ocean. Similar features are also present in other numerical solutions (SEMTNER and CHERVIN, 1992; HIRST and GODFREY, 1992) as well as in estimates of \bar{Q} that use observed SST (HASTENRATH and LAMB, 1979; ESBENSEN and KUSHMIR, 1981; HSUNG, 1985; OBERHUBER, 1988). In the other \bar{Q} fields, however, the $\bar{Q} < 0$ region is confined south of 10°S , it extends farther westward, and there is no heating adjacent to the west coast of

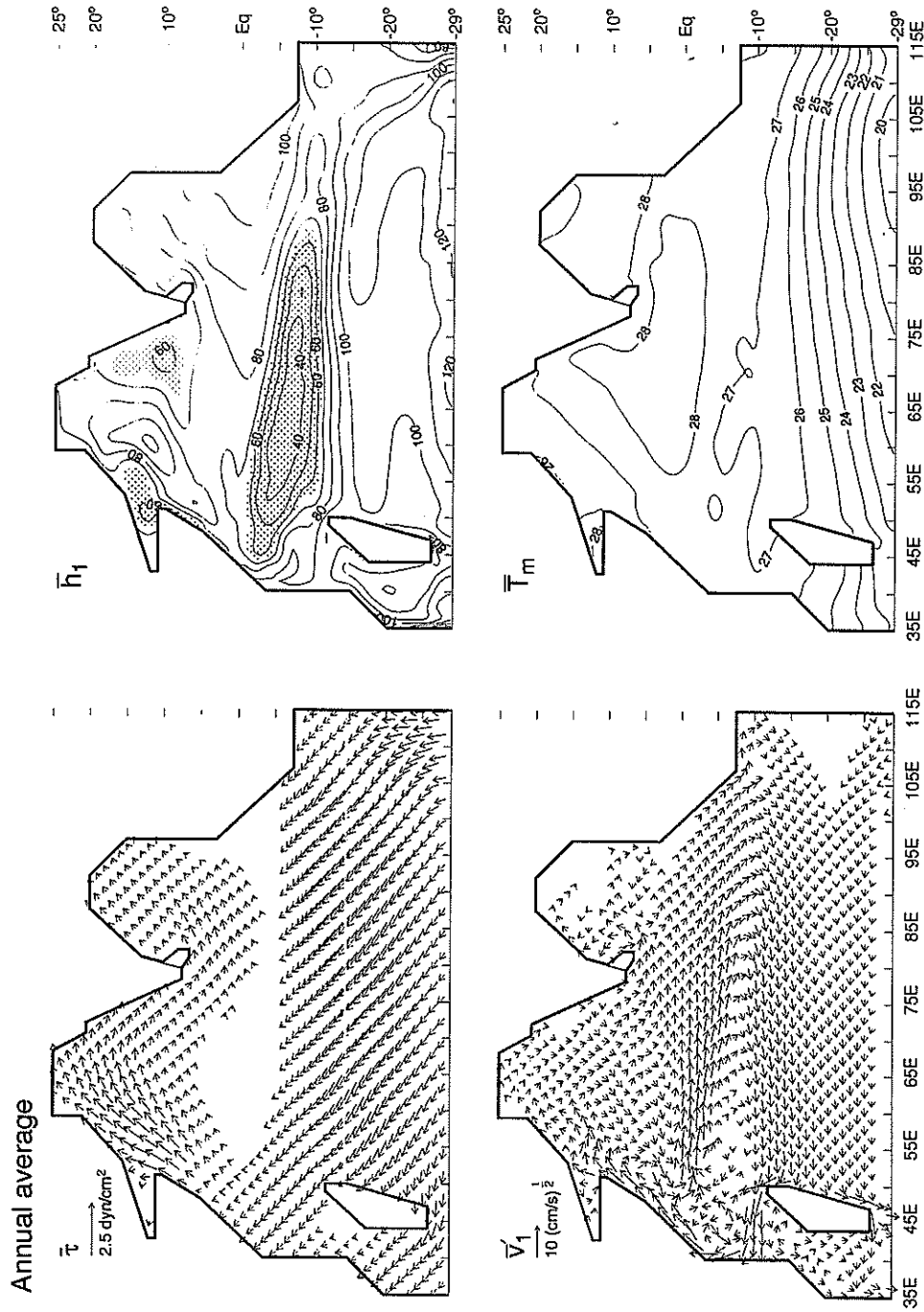


Fig.3. As in Fig.2a, except for annual-mean fields. The mean wind field is dominated by the Southwest Monsoon, and the upper-layer circulation in the northern ocean reflects this property. The flow in the southern ocean is dominated by the Tropical Gyre, and the northern portion of the anticyclonic Subtropical Gyre is present south of 18°S. The upper-layer thickness \bar{h}_1 is shallow in a region from 2.5°S to 15°S because of Ekman suction by negative wind curl.

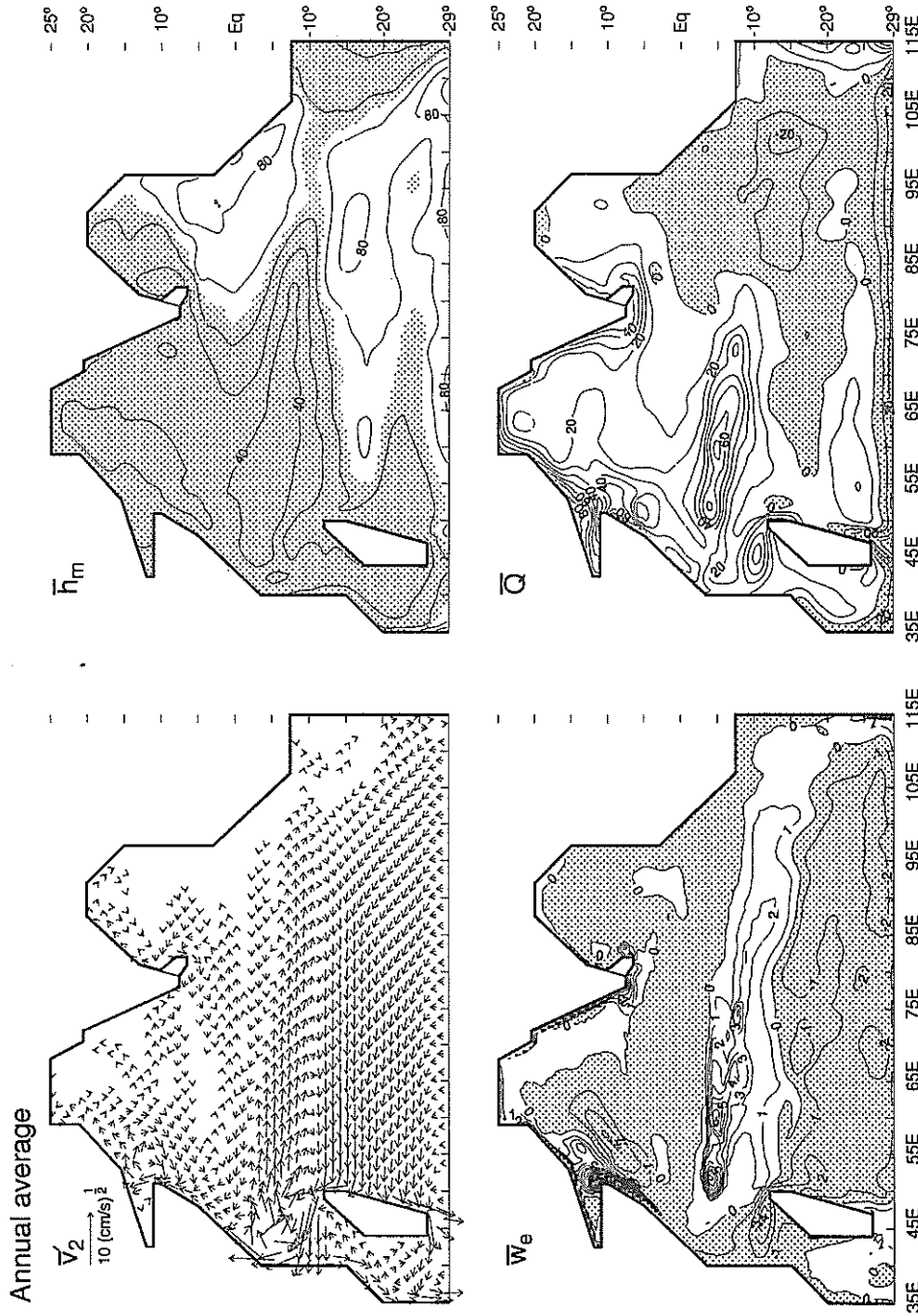


Fig. 3'. As in Fig. 2b', except for the annual-mean fields. The contour interval for \bar{w}_e is $10^{-4} \text{ cm s}^{-1}$, and that for \bar{Q} is 10 W m^{-2} . The northern branch of the Tropical Gyre does not extend as far north in the lower layer as it does in the upper layer. Entrainment is large in the upwelling region off Somalia where \bar{w}_e reaches a maximum value of $6.6 \times 10^{-3} \text{ cm s}^{-1}$, along the west coast of India, and in a broad band from about 2.5°S to 15°S . There is detrainment in the central Arabian Sea and in the southern Indian Ocean south of 15°S . The surface heat flux \bar{Q} is positive in upwelling regions where $w_e > 0$, and positive northwest of Madagascar as a result of advection; it is negative in the Agulhas and East Madagascar Currents because of advection, and negative along the southern boundary because of diffusion.

Australia. In addition, only the numerical solutions have the band of heating near 5°S: in the HASTENRATH and LAMB (1979), HSUNG (1985) and OBERHUBER (1988) analyses, the band exists but it lies on the equator; in the ESBENSEN and KUSHMIR (1981) study, there is no band at all. Another property of the solution's \bar{Q} field is that negative regions are not sufficiently strong to cancel the positive regions elsewhere and so there is a net heat gain of $3.2 \times 10^{14} \text{ W}$ over the entire basin (an average heat flux of 8.6 W m^{-2}). This net heat input is reasonably close to values estimated from satellite measurements ($6 \times 10^{14} \text{ W}$; HASTENRATH, 1982) and from hydrographic data along 32°S ($5 \times 10^{14} \text{ W}$; TOOLE and RAYMER, 1985), but the uncertainties in these estimates are large.

What processes account for the horizontal structure of \bar{Q} ? Test calculations discussed at the end of Section 4.2 answer this question. (Also see Section 4.4 for a discussion of how the Pacific throughflow affects \bar{Q} .) For the moment, we note that its structure is not similar to any of the atmospheric forcing fields (RAO *et al.*, 1989, 1991), and that there is an obvious close relationship between \bar{Q} and \bar{w}_e (Fig. 3'), indicating the importance of entrainment cooling in determining \bar{Q} .

3.2.2. Meridional circulation cells: What is the source of water for the upwelling in the northern ocean? Where does the upwelled water go? To help answer these questions, Fig. 4 shows plots of spatially integrated terms from the continuity equations in (2) averaged over the tenth year of the integration. Let q be any of the terms with q set to 0 over land, and x_e , x_w and $y_n = 25^\circ \text{N}$ be the locations of the eastern, western and northern boundaries of the basin. Then, except for the profile $-WE_y$, the profiles are defined by $\int_{y_n}^{y_n} \int_{x_e}^{x_w} q \, dx dy \equiv Q(y)$. The zonal integrations filter out the strong horizontal gyres, allowing the weaker meridional circulations associated with the movement of water between layers to be more evident. Profile WC is the correction for mass imbalance and is zero except near the southern boundary. The horizontal diffusion terms, D_1 and D_2 , are small throughout the domain, so basically the upwelling WE balances advection V_1 . The lower-layer transport $V_2(y)$ is not shown because it is very similar to two of the other curves: essentially $V_2(y) = -(V_1 + WC) = WE$ except for small differences resulting from D_1 and D_2 . For convenience, a scaled version of the profile $-WE_y \equiv \int_{x_w}^{x_e} \bar{w}_e \, dx$ is also included to illustrate more clearly the locations of upwelling and downwelling regions. (The profiles in Fig. 4 are collectively equivalent to a plot of the zonally integrated transport streamfunction that exists in continuously stratified models, for example, as in Fig. 10 of PHILANDER, HURLIN and SIEGEL, 1987).

Profile $-WE_y$ indicates that there is a net upwelling in the northern ocean and in the southern ocean from 2.5°S to 14°S; virtually all downwelling occurs south of 14°S, with only a very weak detrainment region near the equator. The upper-layer transport V_1 becomes increasingly southward (negative) away from the northern boundary (except in the weak downwelling region near the equator) as the upper layer "absorbs" the entrained water in the northern ocean, reaching a peak value of 11 Sv near 14°S. Farther to the south the magnitude of V_1 decreases because of detrainment (subduction) of water into the lower layer, consequently V_1 reverses sign at 27°S. The fields V_1 , $V_2 (= -V_1)$, and $-WE_y$ define two closed, *meridional circulation cells* that extend from the northern boundary of the basin to 27°S. The *Tropical Cell* is confined to the southern hemisphere from 2.5°S to 24°S and has a strength of $WE(14^\circ \text{S}) - WE(2.5^\circ \text{S}) = 6.5 \text{ Sv}$. The *Cross-Equatorial Cell* is closed by upwelling in the northern ocean and has a strength of $WE(6^\circ \text{N}) = 5 \text{ Sv}$.

The *mean* circulation pattern taken by water parcels in the solution is more complex than suggested by the two-dimensional profiles of Fig. 4. Consider again the \bar{w}_e , \bar{v}_1 and \bar{v}_2 panels in Figs 3 and 3'. Water subducted in the southern ocean moves westward in the South Equatorial Current and northward in the East African Coastal Current. Just south of the equator, the part of

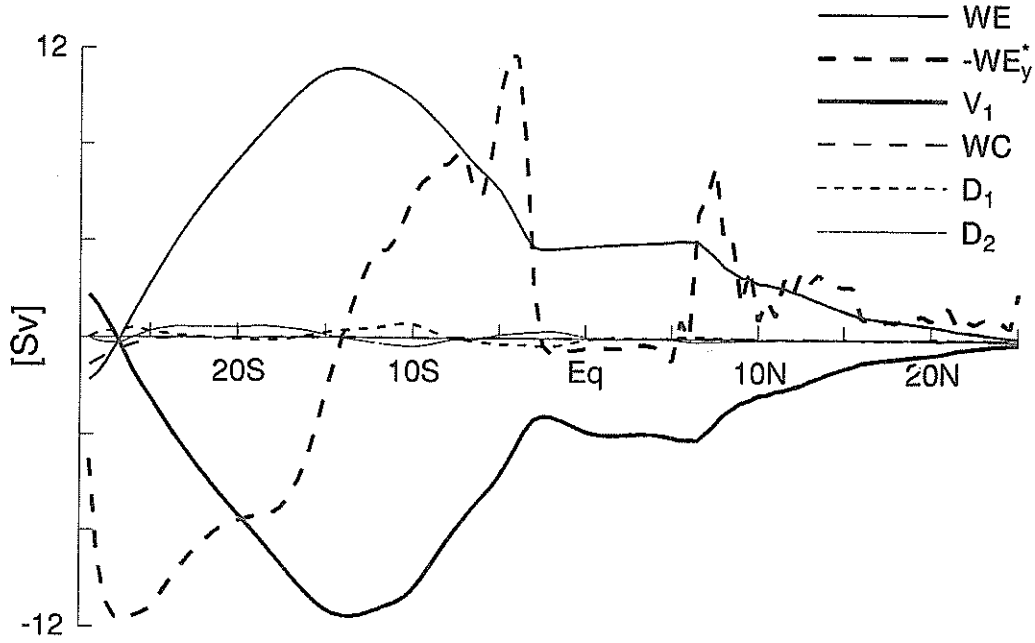


Fig.4. Meridional profiles of spatially integrated terms from the continuity equations in (2a) and (2b) averaged over the tenth year of the integration. The curves labelled WE, V_1 , D_1 and WC are area integrals of the quantities \bar{w}_e , $\nabla \cdot \bar{h}_1 \bar{v}_1$, $\kappa_h \nabla^2 \bar{h}_1$ and w_e , respectively. The quantity $V_1(y) = \int_{x_e}^{x_w} \bar{h}_1 \bar{v}_1 dx$ is the total upper-layer transport across a latitude line. The profiles $D_1 = \int_{x_e}^{x_w} \kappa_h \bar{h}_{1y} dy$ vanish at 29°S as a consequence of the boundary conditions on h_1 and h_2 . The profile $-WE_y^* = \phi(WE)_y = \phi \int_{x_e}^{x_w} \bar{w}_e dx$ where $\phi=10^8\text{cm}$ is a scale factor. Integrals of \bar{h}_{1t} and \bar{h}_{2t} are not shown because they are negligible.

this lower-layer current that participates in the Tropical Cell bends offshore to flow eastward in the Equatorial Countercurrent, where it is entrained back into the upper layer. The rest crosses the equator near the western boundary to participate in the Cross-Equatorial Cell, and is eventually upwelled off Somalia and Arabia. There is also a westward equatorial flow west of about 65°E that supplies some of the water for the Arabian-Sea upwelling. The upwelled water flows southward in the interior Arabian Sea by a circuitous path to join the Equatorial Countercurrent, eventually returning to the southern Indian Ocean in the Tropical Gyre. The source of water for the upwelling off the tip India is less clear; the v_2' plot suggests that much of this upwelled water arises from a westward lower-layer flow around the tip of India and that the source of this current is a weak eastward current along the equator. It is worth pointing out here that the actual *time-dependent* trajectories taken by water particles can differ considerably from the paths suggested by the mean flow; in this regard, note that in July *all* the lower-layer water for the Somali upwelling comes from an eastward Equatorial Undercurrent, and an additional source of fluid for the upwelling along India is an eastward flow across the Arabian Sea near 6°N (Fig.2b').

Finally, note that there is a net upper-layer inflow of $V_1(29^\circ\text{S}) = 1.8\text{Sv}$ across the open southern boundary. The prominent cross-boundary flows in Fig.3 are the southward-flowing Agulhas and East Madagascar Currents, but evidently this outflow is more than compensated by a slower, nearly uniform, inflow everywhere else along the boundary. This upper-layer inflow is not completely balanced by lower-layer outflow [$V_2(29^\circ\text{S}) = -0.7\text{Sv}$], and so the entrainment correction term w_e is required to remove the additional fluid [$WC(29^\circ\text{S}) = -1.1\text{Sv}$]. Recall that in a test run without w_e mass was added to the upper layer at a rate of 6Sv , whereas with w_e water needs to be removed at a rate of only 1.1Sv ; the likely reason for this improvement is the wedge shape of the correction volume, which correctly tends to generate a geostrophically balanced flow out of the basin.

3.2.3. The heat budget: As noted in Section 3.2.1, there is a net annual heat gain through the ocean surface of $3.2 \times 10^{14}\text{W}$. How does the system get rid of this heat? We define the heat in each layer to be $h_i T_i$, and it follows from the equations of motion that

$$\begin{aligned} (h_1 T_1)_t + \nabla \cdot (h_1 \mathbf{v}_1 T_1) &= Q + [w_e \theta(-w_e) T_f + w_e \theta(w_e) T_e] \\ &+ \{ \kappa_T h_m \nabla^2 T_m + \kappa_T h_f \nabla^2 T_f + \kappa_h T_1 \nabla^2 h_1 \}, \\ (h_2 T_2)_t + \nabla \cdot (h_2 \mathbf{v}_2 T_2) &= Q_2 - [w_e \theta(-w_e) T_f + w_e \theta(w_e) T_e] + w_e T_2 \\ &+ \{ \kappa_T h_2 \nabla^2 T_2 + \kappa_h T_2 \nabla^2 h_2 \}. \end{aligned} \quad (12)$$

Figure 5 shows plots of annually averaged terms from equations (12) that are zonally and meridionally integrated as for the profiles in Fig.4. Not surprisingly, the upper-layer terms, VT_1 and WET_1 , are similar in structure to their counterparts in Fig.5, differing only because they include the extra factor T_1 in their integrands.

North of 10°S the profile QA_1 increases monotonically southward, indicating that the upper layer is being heated along every latitude line in this region (that is, $-QA_{1y} = \int_{x_e}^{x_w} Q \, dx$ is positive).

Entrainment introduces additional heat into the upper layer wherever $-(WET_1)_y > 0$, namely, in the northern ocean north of 6°N and the southern ocean from 3°S to 14°S . In the northern ocean these sources are balanced by a southward transport of heat VT_1 in the Cross-Equatorial Cell. Upper-layer heat is removed via subduction south of 14°S where $-(WET_1)_y < 0$. Note that at the southern boundary $QA_1(29^\circ\text{S}) = 3.2 \times 10^{14}\text{W}$, the total heat gain through the ocean surface, is primarily balanced by the subduction term $WET_1(29^\circ\text{S}) = 4.0 \times 10^{14}\text{W}$, rather than by southward advection in the western-boundary currents as might be expected.

The lower-layer heat budget north of 10°S is primarily a balance between the heat loss caused by entrainment WET_2 and northward advection VT_2 . Recall from the discussion after equations (5) that Q_2 acts to warm T_2 in upwelling regions. This warming can be significant, reaching a maximum of 72W m^{-2} in the cold wedge off Somalia in July. The warming can be seen in the profile QA_2 , which is slightly positive near 10°N ; its effect on QA_2 is small because the area over which $Q_2 > 0$ is small. South of 10°S the artificial heating term Q_2 becomes increasingly negative because the subduction there adds upper-layer water to the lower layer with a temperature considerably warmer than T_2 . Indeed, the total amount of heat removed by Q_2 over the entire basin is $QA_2(29^\circ\text{S}) = -2.6 \times 10^{14}\text{W}$, an amount comparable to the heat gain through the ocean surface. Note that the entrainment correction w_e also results in a significant heat loss of $WCT(29^\circ\text{S}) = -0.8 \times 10^{14}\text{W}$.

This result, that most of the heat input through the ocean surface is removed by the artificial terms Q_2 and $w_e T_2$, is an unpleasant aspect of the model's heat budget. It occurs because the model

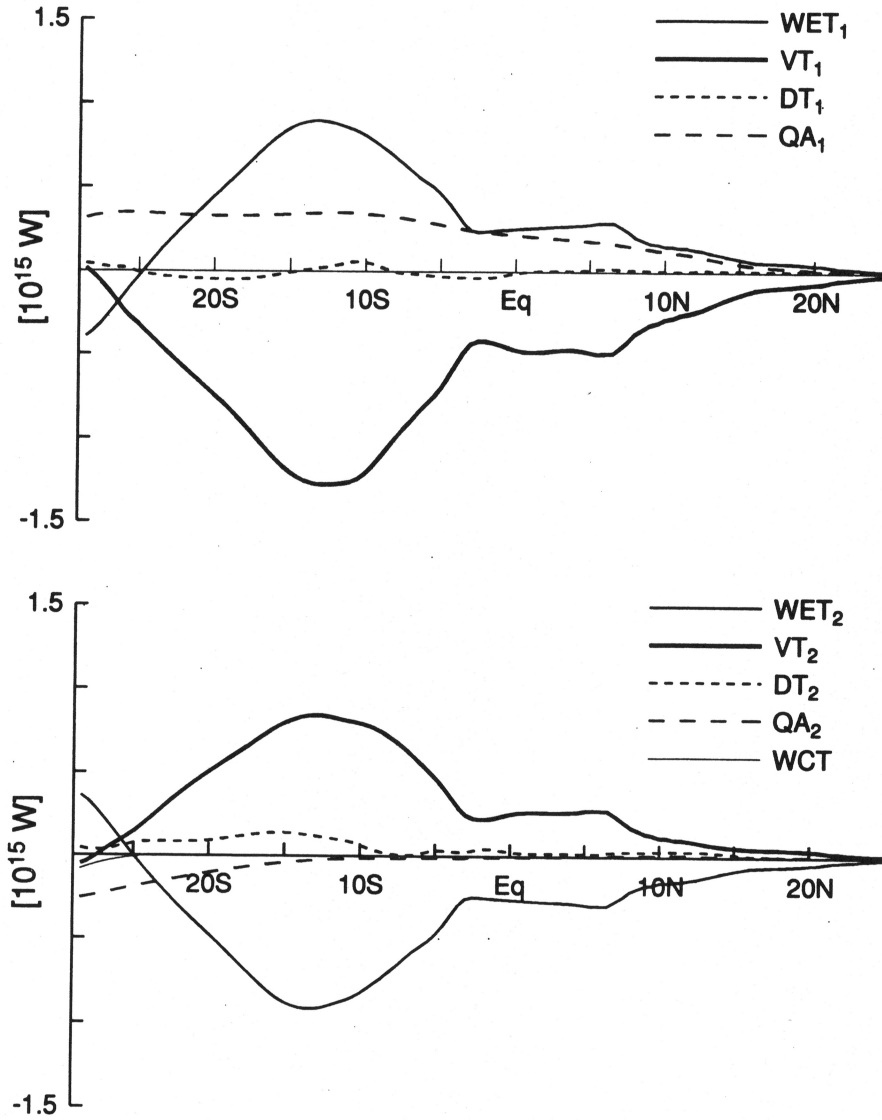


Fig.5. Meridional profiles of spatially integrated terms from the heat equations (12) averaged over the tenth year of the integration. The profiles are area integrals of the terms, as defined in the text. The curves labelled VT_i , QA_1 , QA_2 , WCT , WET_i and DT_i are integrals of the quantities $\nabla \cdot (h_i v_i T_i)$, Q , Q_2 , $w_e T_2$, the terms in square brackets in (12), and the terms in curly brackets, respectively. The quantity $VT_i = \int_{x_e}^{x_w} h_i v_i T_i dx$ is the total heat transport across a latitude line, and $WET_2 = -WET_1$.

basin does not extend far enough to the south. In a larger basin, detrainment could be parameterized to occur in a region where the subducted water has a temperature close to T_2 , and in that case the magnitude of Q_2 would be much smaller. Moreover, with detrainment located farther south the Agulhas Current would carry warm waters farther southward where they would be cooled through the surface, eventually ensuring that the net heat flux through the ocean surface approaches zero.

4. PROCESSES

In Section 3 we noted many of the important dynamic, thermodynamic and mixed-layer processes at work in the main run. Here we report a number of test calculations that helped to isolate these and other processes. Indeed, many of the conclusions reported in Section 3 were predicated on results from these tests. Section 4.1 investigates the relative importance of local and remote forcing in the northern Indian Ocean by modifying the wind field that forces the solution. Section 4.2 examines the processes that maintain the model's SST and surface heat-flux fields by eliminating various terms from the equation for T_m . Section 4.3 explores the sensitivity of solutions to alternate parameterizations of the subduction rate w_d . Finally, Section 4.4 reports on the circulation changes that result from including the Pacific-Ocean throughflow.

4.1 Solutions for modified wind forcing

In this section we discuss solutions for which the wind stress τ is eliminated in each of the three regions: the Arabian Sea defined to be the region $y > 0^\circ$, $x < 79^\circ\text{E}$, the Bay of Bengal in the region $y > 0^\circ$, $x > 79^\circ\text{E}$, and the equatorial waveguide from $5^\circ\text{S} < y < 5^\circ\text{N}$. Edges of the wind regions (at 5°S , 5°N , 0° and 79°E) are smoothed by cosine tapers centered on the edges with widths of 5° in y and 2.5° in x . Truncation of the wind field in this manner introduces erroneous wind curl near the edges which can generate false currents; however, the effects of truncation are identifiable, and generally they do not significantly influence the particular region of interest. Although τ is set to zero in the various regions, the scalar wind V_s and the friction velocity u_* are not; thus, thermodynamic and mixed-layer processes remain relatively unchanged in these tests.

4.1.1. Modified winds in the Arabian Sea: Figure 6a shows the upper-layer current and thickness fields in July, when the Arabian-Sea winds are neglected throughout the year. As expected, the circulations in the western and central portions of the Arabian Sea are very different from those in the main run (Fig. 2b), the most obvious difference being the lack of a northward Somali Current in Fig. 6a. In addition, the eastward and southeastward flows across the interior of the Sea, as well as the region of deep h_1 centered near 60°E , 10°N , are absent, confirming the cause of these features to be forcing by the local winds, namely, offshore Ekman drift from the coast and Ekman pumping in the interior ocean. Note that h_1 still deepens off Somalia in a region centered near 53°N , 10°N , but only from 80m to 100m; $h_m = h_1$ and $w_e > 0$ in this region, indicating that this deepening results from entrainment induced by wind stirring (a process which is not much altered from the main run since u_* is not set to zero in the test). In contrast, the main-run and test solutions are strikingly similar near the west coast of India; as in the main run, h_1 is still shallow along the west coast, and isolines still bend farther offshore in the south. This agreement demonstrates that remote forcing by the winds in the Bay of Bengal is an influential process in the west-coast upwelling, a conclusion supported further by the test calculation in Section 4.1.2. However, the region of cool SST extends only to 12°N along the coast in the test run (not shown), whereas in the main run it extends to 17°N , implying that forcing by the local winds does enhance the model upwelling, consistent with the observations summarized in Section 3.1.1.

Figure 6b shows the January response when the Arabian-Sea winds are neglected. As in the main run (Fig. 2e), there are still regions of shallow and deep h_1 near the Indian Coast, confirming that neither of these features are locally driven by the Arabian-Sea winds. Indeed, the shallow region was remotely forced during the previous Southwest Monsoon by winds in the Bay of Bengal (Fig. 6a), and subsequently propagated offshore as a Rossby wave. In contrast, the main run and test solutions differ considerably in the western Arabian Sea, for example, with h_1 being nearly flat north of 5°N in Fig. 6b. As discussed next, these differences result from the lack of both the Northeast and Southwest Monsoon winds in the test run.

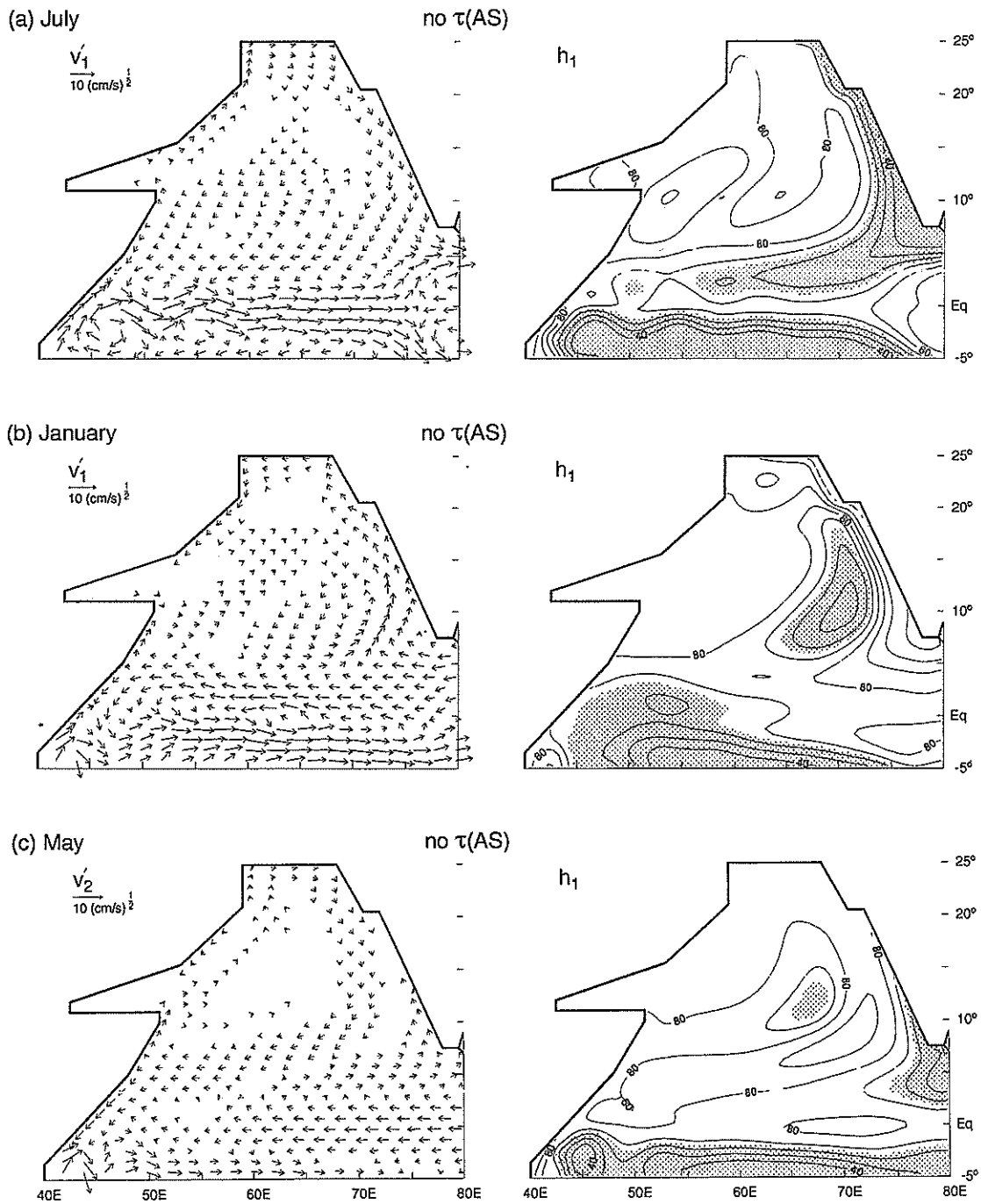


Fig.6. Horizontal distributions of upper-layer current v'_1 , lower-layer current v'_2 (lower-left panel), and upper-layer thickness h_1 fields when forcing by winds in the Arabian Sea (the region $x < 79^\circ\text{E}$, $y > 0^\circ$) is neglected. The solution is shown during July (upper panels, Fig.6a), January (middle panels, Fig.6b) and May (lower panels, Fig.6c). The contour interval for h_1 is 10m, regions where $h_1 \leq 65\text{m}$ are shaded, and current arrows are of the vector field $\mathbf{v}' = \mathbf{v}/|\mathbf{v}|^{1/2}$. In Fig.6a, as in the main run (Fig.2b) h_1 shallows along the west coast of India. In Fig.6b, regions of low and high h_1 in the eastern Arabian Sea are similar to those in the main run (Fig.2e). In Fig.6c, a band of high h_1 extends across the Arabian Sea, and a southward Somali Undercurrent joins the westward and eastward currents on either side of this band.

To isolate effects forced during each monsoon season, we carried out two additional tests: one with the Arabian-Sea winds deleted *only* during the Northeast Monsoon, and another when they were dropped *only* during the Southwest Monsoon. Figures 7a and 7b show the January response for the first and second cases, respectively. In Fig. 7a there are still regions of shallow and deep h_1 in the western basin, whereas they are absent in Fig. 6b. It follows that in the main run these features are remnants generated by forcing 6 months earlier during the Southwest Monsoon. A closer comparison of the solution in Fig. 7a with the main run reveals differences that can only result from the absence of Northeast-Monsoon winds. For example, in Fig. 7a the Somali Current north of about 5°N flows strongly to the northeast, whereas in Fig. 2e the countercurrent is weaker and located only north of 8°N . Additionally, in Fig. 7a the h_1 field is somewhat shallower in the region of low h_1 at the mouth of the Gulf of Aden and much deeper offshore of Somalia (near 53°E , 3°N) than in the main run. The solution in Fig. 7b confirms that these differences are caused by local forcing by the Northeast-Monsoon winds, with h_1 deepening in the Gulf of Aden and shallowing off Somalia as a result of Ekman pumping by negative and positive wind curl, respectively. Note also in Fig. 7b that there is cyclonic flow about the region of low h_1 off Somalia, and that no such flow is present in Fig. 7a, confirming that this circulation is locally forced in the main run.

Figure 7c shows v'_1 (left panel) and v'_2 (right panel) in March for the test run without Arabian-Sea winds during the Southwest Monsoon. In contrast to the January flow field in Fig. 7b, the Somali Current is absent or weakly northeastward in the upper layer north of 5°N . This change can only be forced by negative wind curl north of the axis of the Northeast Monsoon winds, as suggested by QUADFASSEL and SCHOTT (1983). Recall that in the main run there is a *strong*, upper-layer countercurrent north of 4°N at this time (Fig. 2f). Its weakness in Fig. 7c demonstrates that remote forcing by Southwest-Monsoon winds is also a significant driving mechanism: essentially, the remotely forced January countercurrent in Fig. 7a is a major contributor to the main-run countercurrent in March. A similar reversal takes place in the lower-layer flow field in Fig. 7c, with the current north of 5°N flowing northeastward at speeds approaching 20 cm s^{-1} . In the main run, the fall Somali Undercurrent (Figs 2d' and 2e') reverses in March, and we conclude from this test that this reversal is a locally forced response to negative wind curl.

Fig. 6c shows the May response for the test without Arabian-Sea winds throughout the year. South of about 10°N the structure of the lower-layer flow field is much like that in the main run (Fig. 2a'). In particular, there is a southward Somali Undercurrent from 7°N to the equator. This flow is clearly associated with a region of high h_1 that extends across the southern Arabian Sea, a feature generated by the propagation of Rossby waves from the coast of India. This region is visible during January both in the test calculation (Fig. 6b) and in the main run (Fig. 2e) when it extends partially across the basin. By April it has propagated to the western boundary, and the Somali Undercurrent is the flow that joins the westward and eastward branches to the north and south of this band. Thus, this test indicates that remote forcing from the Bay of Bengal is an important forcing mechanism of the model's springtime Somali Undercurrent. It should be noted, however, that because the lower-layer current becomes southwestward in March (in the main run, as well as in the test calculation in Fig. 7c) before the arrival of the Rossby wave, the local northeasterly winds must help to establish this flow.

4.1.2. No winds in the Bay of Bengal: Figure 8a shows the July response when the winds in the Bay of Bengal are neglected throughout the year. The striking difference from the main run (Fig. 2b) is that there are no regions of shallow h_1 adjacent to India. Indeed, throughout the Southwest Monsoon h_1 never reaches $h_{\min} = 35\text{ m}$ anywhere along the Indian coasts, so that there is no entrainment of cool water and T_m remains warm. One reason for this difference is that there is no upward tilt of h_1 toward the south along the east coast of India, in the absence of upwelling-

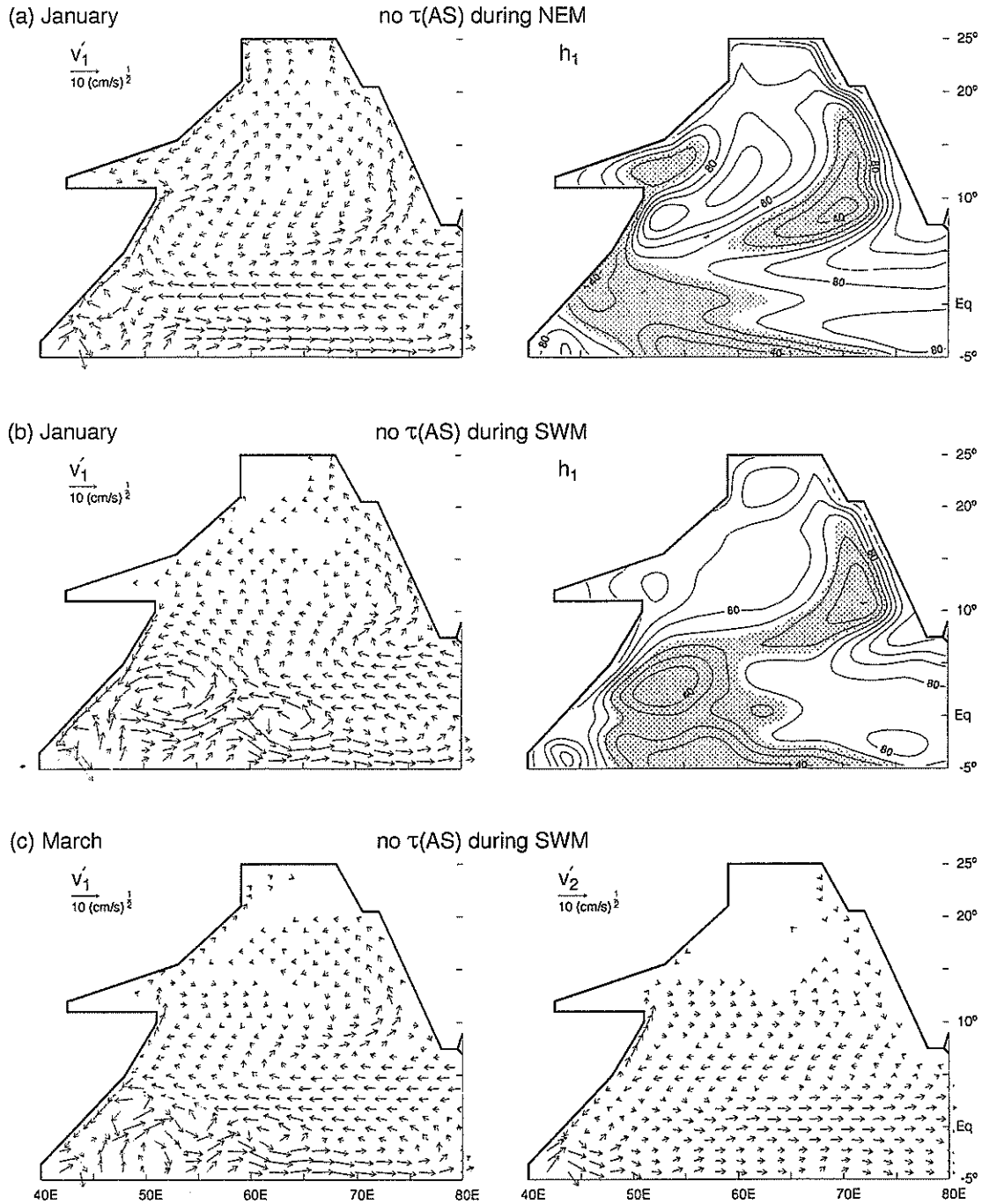


Fig.7. Horizontal distributions of upper-layer current v'_1 , lower-layer current v'_2 (lower-right panel) and upper-layer thickness h_1 fields for two test solutions: when Arabian-Sea winds are neglected only from November through March (upper panels), and when they are neglected only from April through October (middle and lower panels). The first solution is shown during January (Fig.7a), whereas the second is shown during January (Fig.7b) and March (Fig.7c). In Fig.7a, north of about 7°N there are regions of low and high h_1 in the western Arabian Sea very similar to those in the main run (Fig.2e), and there is a strong northward flow along the Somali coast north of 5°N . In Fig.7b, as in the main run h_1 shallows markedly offshore of Somalia, and deepens near the coasts of Somalia and Arabia; there is a strong cyclonic flow about the region of shallow h_1 off Somalia. In Fig.7c, the Somali Current north of 5°N vanishes in the upper layer and reverses in the lower layer.

favorable winds there. Another is the lack of positive wind curl southeast of India, so that there is no shallow region east of Sri Lanka. The absence of shallow regions along the west coast and southwest of India confirms that these features are primarily remotely forced from the Bay of Bengal in the main run.

The circulation is similar to the main run elsewhere in the Bay. The deepening of h_1 in the eastern Bay is still present, demonstrating that it is remotely forced from the equator via the reflection of a downwelling-favorable equatorial Kelvin wave. Note, however, that h_1 does not deepen as much as it does in the main run; this weakening results from the truncation of westerly winds near the equator in the eastern basin, so that the equatorial Kelvin wave has a somewhat smaller amplitude. There is still an eastward current across the southern Bay associated with the Rossby-wave packet reflected from the eastern boundary, but the strong eastward current south of India in the main run is absent in Fig. 8a, demonstrating that this feature is generated primarily by local wind curl, rather than by the reflected Rossby wave.

Fig. 8b shows the January response without Bay-of-Bengal winds, and the circulation differs considerably from the main run almost everywhere. In the southwestern region of the Bay, the region of shallow h_1 and the associated cyclonic flow around it are weak or absent, indicating that that circulation is driven by local Ekman pumping in the interior ocean and the alongshore wind at the coast. [There is still a region of weakly shallow h_1 in Fig. 8b in the southeastern Bay; this feature was generated at the eastern boundary of the Bay during the previous March (Fig. 8c), and subsequently propagated across the Bay as a Rossby wave (Fig. 8a).] All across the southern Bay, there is westward flow in Fig. 8b centered near 2.5°N , whereas in the main run the current is shifted farther north to 5°N ; this difference identifies the source of the main-run current to be Ekman pumping by the local winds, rather than remote forcing by a reflected Rossby wave.

Along the northeast boundary of the Bay there is a weak northwestward flow in Fig. 8b, but a southeastward coastal current in the main run, indicating that the latter current is forced by the upwelling-favorable (northwesterly) component of the alongshore wind there. Similarly, in the main run there are eastward and northeastward currents along the northern and northwestern boundaries, respectively, which are not present in Fig. 8b. Since the wind is not upwelling favorable in either region, it follows that these main-run currents are remotely forced by winds elsewhere in the Bay. Their direct connection with the coastal current along the northeast boundary suggests that remote forcing by the alongshore winds on the northeast coast via the propagation of coastal Kelvin waves is an important process. An alternate possibility is forcing by negative wind curl in the interior of the western Bay, as hypothesized by SHETYE *et al.* (1992); in this scenario, the circulation adjusts toward a Sverdrup-balanced state consisting of southward flow in the interior of the western Bay and a compensating, northward, western-boundary current along the east coast of India (see their Fig. 10). In support of this idea, such an anticyclonic gyre is apparent in the lower-layer flow field of the main run (Fig. 2e') but it is absent in the test (not shown).

The two January solutions (Fig. 8b and 2e) are similar in that both have a region of deep h_1 in the northern ocean. In both solutions, $w_e > 0$ and the mixed-layer thickness h_m is equal to h_1 , confirming that this deepening in the main run is a result of entrainment caused by convective overturning (which still exists in the test run because $V_s \neq 0$). Note in Fig. 8b that the region does not shallow toward the northern coast as it does in the main run, consistent with the absence of the eastward coastal current in the test run.

Figure 8c shows the model response in March without the Bay of Bengal winds. As in the main run, h_1 is shallow along the eastern boundary of the Bay, demonstrating that this feature is remotely forced by the reflection of an upwelling equatorial Kelvin wave; likewise, the current along the northeast coast is southeastward in the test, indicating that equatorial forcing contributes to the

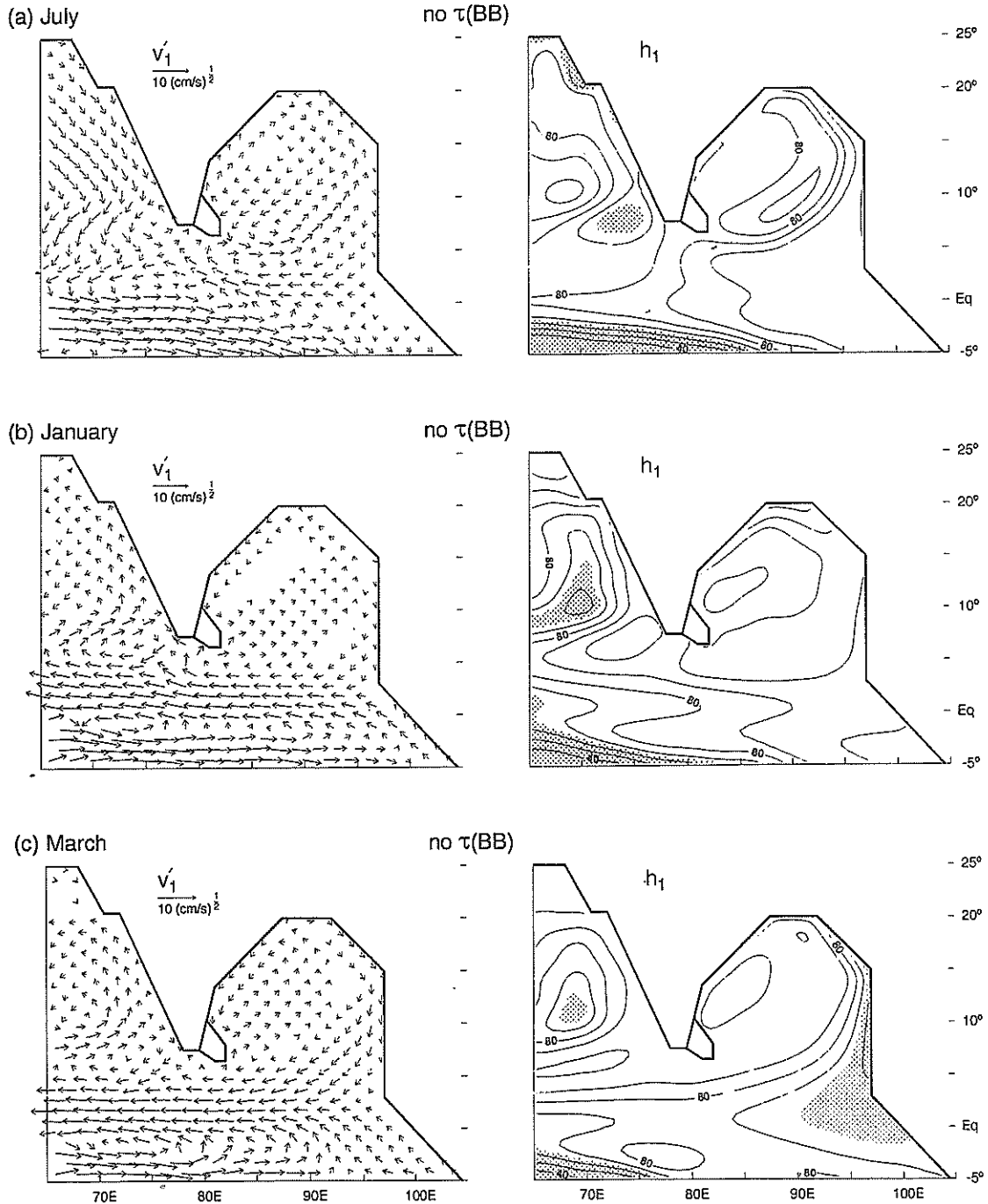


Fig. 8. Horizontal distributions of upper-layer current v'_1 and thickness h_1 fields when forcing by winds in the Bay of Bengal (the region $x > 79^\circ\text{E}$, $y > 0^\circ$) is neglected. The solution is shown in July (upper panels, Fig. 8a), in January (middle panels, Fig. 8b) and in March (lower panels, Fig. 8c). The contour interval for h_1 is 10m, regions where $h_1 \leq 65\text{m}$ are shaded, and current arrows are of the vector field $\mathbf{v}' = \mathbf{v}/|\mathbf{v}|^{1/2}$. In Fig. 8a, unlike the main run (Fig. 2b), h_1 does not shallow anywhere along the east coast of India, it is not nearly as shallow along the west coast of India, and there is no longer a strong eastward current south of India. As in the main run, there still is a region of deep h_1 in the eastern ocean extending northward around the perimeter of the Bay. In Fig. 8b, unlike the main run (Fig. 2e) the region of shallow h_1 and the strong southward coastal current in the southwestern corner of the Bay are absent. Likewise, there is no shallowing of h_1 along the northern and northeastern boundaries of the basin, and the currents there are westward and southwestward, respectively. As in the main run, h_1 deepens in the northern Bay because of entrainment by convective mixing. In Fig. 8c, there is still a region of shallow h_1 in the eastern Bay, but unlike the main run (Fig. 2c) the current along the east coast of India is southwestward.

main-run current there. In contrast, the current along the east coast of India has the same direction that it had in January, whereas in the main run it reverses to flow strongly northward. It follows that the reversal must arise from forcing within the Bay. As noted above for the January situation, one possible cause is the presence of upwelling-favorable winds elsewhere in the Bay, namely, on the northeast boundary of the Bay throughout the Northeast Monsoon and along the northwest boundary beginning in March (upper-left panel of Fig. 2f). A second possibility is forcing by negative wind curl in the interior of the western Bay (SHETYE *et al.*, 1992).

4.1.3. No winds in the equatorial waveguide: We have seen in Fig. 2 that there are two prominent events that affect h_1 in the eastern equatorial ocean. Both are generated by the reflection of equatorial Kelvin waves from the eastern boundary of the ocean: a downwelling event in April and May, and an upwelling one in February and March. There is a third, weaker downwelling event in October and November. It is also apparent in Fig. 2 that these events radiate into, and around the perimeter of, the Bay of Bengal. POTES *et al.* (1991) and YU, O'BRIEN and YANG (1992) have drawn attention to this process, suggesting that it is an important forcing mechanism in their models. To test its importance in our model, we carried out a test calculation without the winds in the equatorial waveguide. As expected, there are no surges of eastward flow along the equator in the spring and fall, no significant westward flow in February and March, and hence the waves reflected from the eastern boundary are weak or absent.

Figure 9a shows the model response in July when there are no winds in the equatorial waveguide. The primary change in the test calculation is that h_1 does not deepen in the eastern basin, as a result of the absence of a downwelling, reflected Rossby wave. Elsewhere the structure of the current and upper-layer thickness fields are similar to those from the main run, verifying that much of the circulation in the Bay is *not* remotely forced from the equator. One consequence along the east coast of India is that the region of shallow h_1 (≤ 65 m) extends farther north to 20°N , as compared to only 17°N in the main run, and this difference points toward the competition between local and equatorial forcing along the east coast of India at this time. Note also that the upper-layer thickness is not as shallow southwest of India as in the main run, a distortion caused by the weakened positive wind curl and Ekman suction south of India. West of 79°E , two prominent differences from the main run are the existence of a westward current near 2.5°N and an eastward flow near 5°N ; these differences are an artifact of erroneous wind curl associated with the truncated wind field, but they do not influence the circulation in the Bay of Bengal.

Figure 9b shows the response in September without equatorial winds. In contrast to the main run (Fig. 2c), the current along much of the east coast of India remains northward, and, consistent with geostrophy, isolines of h_1 shallow everywhere toward the coast. These differences confirm that in the main run the September reversal is caused by remote forcing from the equator. By November (not shown) both the east-coast and west-coast currents have strongly reversed just as in the main run, suggesting that the collapse of the southwesterly winds in the Bay of Bengal is the dominant forcing mechanism at this time.

In January, the response of the test solution (not shown) is very similar to the main run in the Bay of Bengal and Arabian Sea. This close similarity holds throughout most of the Northeast Monsoon, indicating that the circulation is not significantly affected by equatorial processes in this season. Fig. 9c shows the model response in March. As expected, h_1 is deeper in the eastern Bay of Bengal than it is in the main run, because of the absence of equatorial forcing. Although there is still a southeastward current along the northeast coast of the Bay it is weaker than in the main run, showing that equatorial forcing does contribute to the main-run current at this time. As in the main run, the current along the east coast of India reverses its direction from January, confirming that the reversal results from local forcing within the Bay and *not* from equatorial forcing.

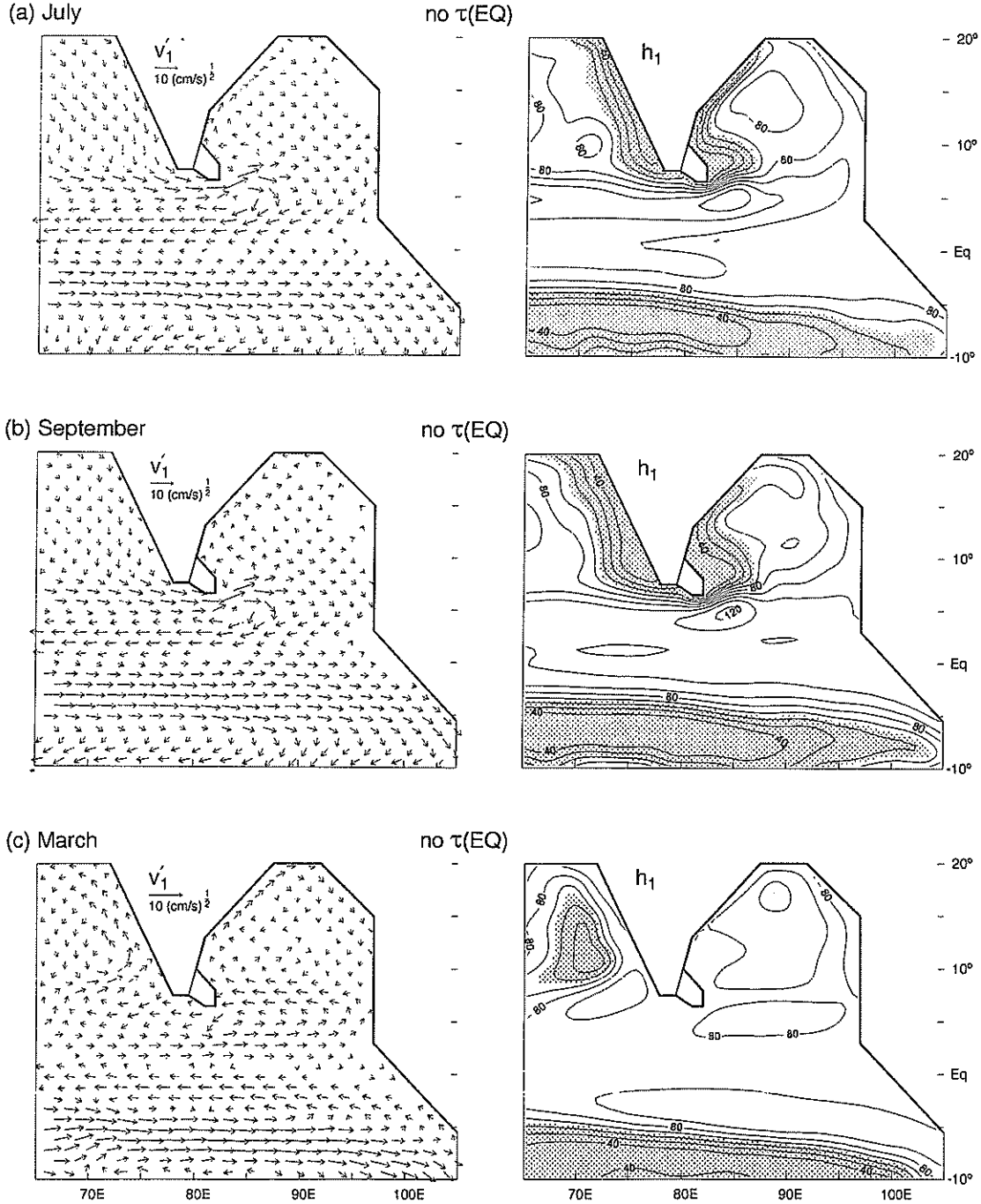


Fig.9. Horizontal distributions of upper-layer current v'_1 and thickness h_1 fields when wind forcing in the equatorial waveguide (the region $5^\circ S < y < 5^\circ N$) is neglected. The solution is shown in July (upper panels, Fig.9a), in September (middle panels, Fig.9b), and in March (lower panels, Fig.9c). The contour interval for h_1 is 10m, regions where $h_1 \leq 65$ m are shaded, and current arrows are of the vector field $v'_1 = v_1 / |v_1|^{1/2}$. In Fig.9a, unlike the main run (Fig.2b), h_1 remains shallow in the eastern basin and the region of shallow h_1 along the east coast of India extends somewhat farther to the north. Likewise, the region of shallow h_1 south of India is more coastally confined, and h_1 never reaches h_{min} along the west coast of India. In Fig.9b, the current remains northward along the east coast of India, and isolines of h_1 continue to shallow toward the coast. In Fig.9c, h_1 does not shallow along the eastern boundary of the Bay, whereas it does in the main run (Fig.2f). As in the main run, the current along the east coast of India reverses from its direction in January.

4.2 Effects of terms in the T_m -equation

As we have seen, model SST is remarkably similar to observed SST, generally differing by less than 0.5–1°C. What processes contribute to the maintenance and accuracy of the T_m field? To investigate this question, we carried out a series of test calculations with various terms in the T_m -equation in (3) being modified or eliminated. Each change degrades T_m in some manner, allowing the influence of a particular process to be assessed.

In a test calculation without the advection term $\mathbf{v}_1 \cdot \nabla T_m$, significant differences from the main run are all located near western-ocean boundaries, since isotherms are no longer being shifted by the swift currents there. The most prominent change occurs in the Arabian Sea during the Southwest Monsoon, where the 26°C isotherm, for example, located well offshore in the main run (Fig.2b) remains within 300km of the Somali coast in the test. There are also slight shifts of isotherms in the interior ocean, not at all obvious in the T_m field, that nevertheless affect the annual-mean surface heat flux into the ocean (see the discussion of Fig.11).

To investigate how T_m is influenced by the horizontal structure of the net solar-radiation field caused by cloudiness, we replaced Q_r with a spatially smoothed version Q'_r as follows: first, the zonal structure of Q_r was eliminated by zonally averaging $Q_r(x, y, t)$ to obtain monthly meridional profiles $Q'_r(y, t)$; then, its meridional structure was removed by replacing Q'_r with its best-fit straight line yielding the smooth, annually varying forcing $Q''_r(y, t) = a(t)y + b(t)$. Surprisingly, model SST in this test is changed by less than 0.5°C almost everywhere in the ocean, in spite of the fact that Q_r does exhibit considerable spatial structure (RAO *et al.*, 1989, 1991). This insensitivity apparently occurs because other processes tend to compensate for the lack of structure in Q''_r ; for example, during the Southwest Monsoon Q_r increases by 100 W m⁻² from the eastern to the western Arabian Sea (RAO *et al.*, 1989, 1991), but at this time upwelling and offshore advection dominate the thermodynamic balance.

Figure 10a shows T_m for four test cases in July at the peak of the Southwest Monsoon. Each panel should be compared to the T_m field from the main run in Fig.2b. Without the entrainment cooling term $w_e \theta(w_e)$ (upper-left panel), T_m remains warm in the intense upwelling regions in the northern ocean, and there is no distortion of isotherms in the southern ocean from 2.5°S to 14°S. Moreover, at most locations south of about 20°S, SST is warmer by about 1°C than in the main run, demonstrating the influence of entrainment cooling associated with the deepening of the mixed layer (upper-right and lower-left panels of Fig.2b').

The remaining panels in Fig.10a illustrate how the forcing fields, T_a and q_a , affect T_m . To investigate the influence of T_a , we set $T_a = T_m$ thereby eliminating Q_s as well as all influence of T_a on the size of the drag coefficient C_L (see Section 2.5 and Table 1). To determine the effect of q_a on the latent heat flux Q_L we set $q_a = 0.8q_s$, where $q_s(T_m)$ is the saturation specific humidity at temperature T_m . (In a test calculation with just $Q_s = 0$ the T_m field was nearly identical to that of the main run. As expected, then, Q_s has little influence in the overall thermodynamic balance.) In the tests with $T_a = T_m$ (upper-right panel) and with $q_a = 0.8q_s$ (lower-left panel), there is little change from the main run except that T_m warms near the southern boundary by about 1°C, showing that in the main run cool, dry wintertime air lowers model SST there by increasing C_L and Q_L . In contrast, in a test with both $T_a = T_m$ and $q_a = 0.8q_s$ (lower-right panel), SST warms considerably in the southern ocean by 3°C, and rises in the central equatorial ocean by 1°C. It is interesting that the degradation of the SST field is disproportionately larger when the forcing fields, T_a and q_a , are simultaneously removed than when they are individually removed. The T_a and q_a fields have very similar spatial structures throughout the year, with warm air being associated with humid air and vice versa, and both patterns also resemble that of SST (RAO *et al.*, 1989, 1991). Apparently, the presence of one of these forcing fields can compensate for the lack of the other, but at least one of them is required to simulate SST accurately.

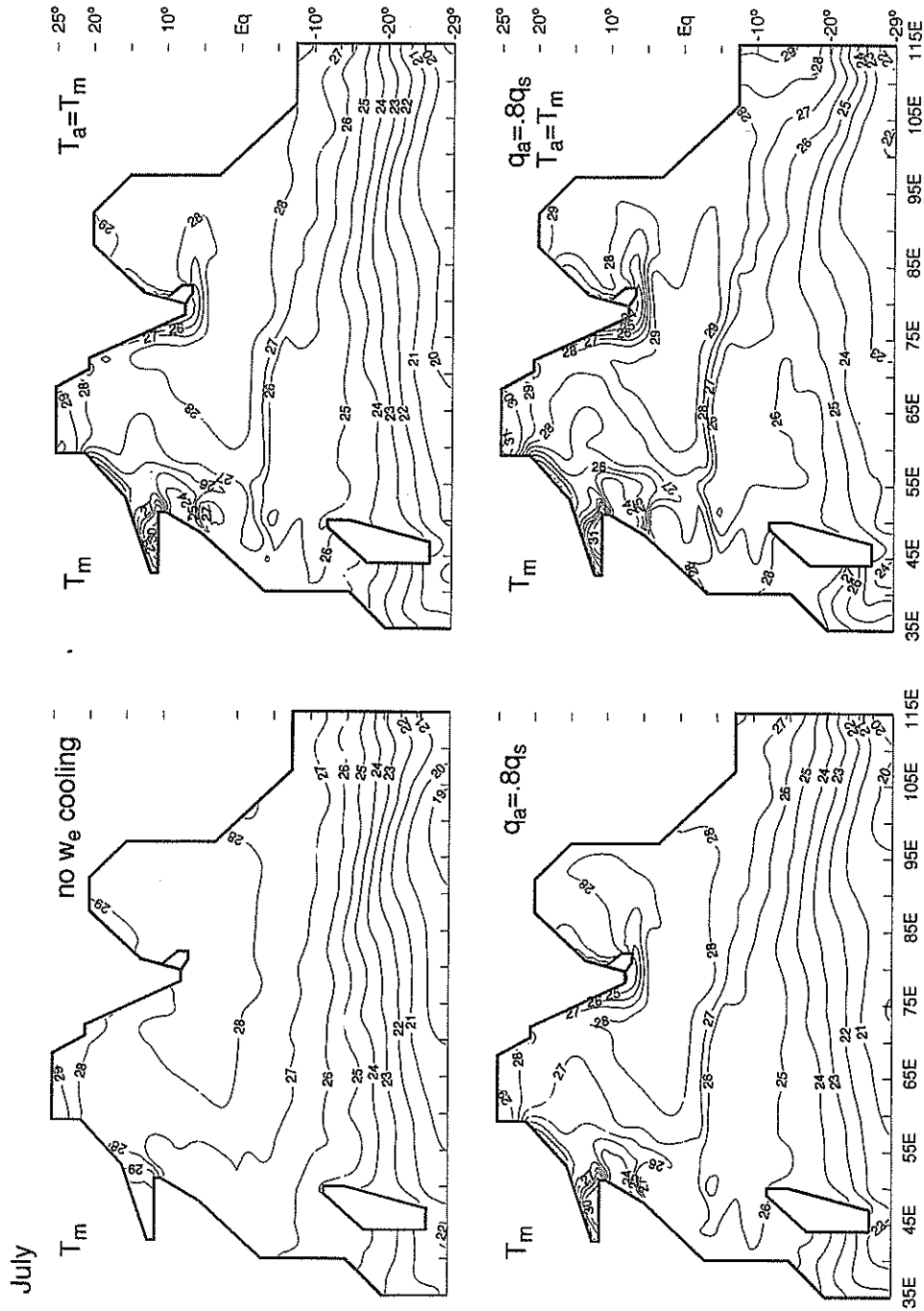


Fig. 10a. Horizontal distributions of model SST in July for four test cases: without entrainment cooling (upper-left panel), with $T_a = T_m$ (upper-right panel), with $q_a = 0.8q_s$ (lower-left panel), and with $T_a = T_m$ and $q_a = 0.8q_s$ (lower-right panel). Compare the plots to the corresponding T_m field in Fig. 2e. Without entrainment cooling T_m remains warm in the upwelling regions in the northern ocean, and warms by about 1°C near the southern boundary. For the tests in the upper-right and lower-left panels, T_m warms near the southern boundary by only about 1°C . In contrast, when both $T_a = T_m$ and $q_a = 0.8q_s$ SST warms by 3°C near the southern boundary and by 1°C in the central, equatorial ocean.

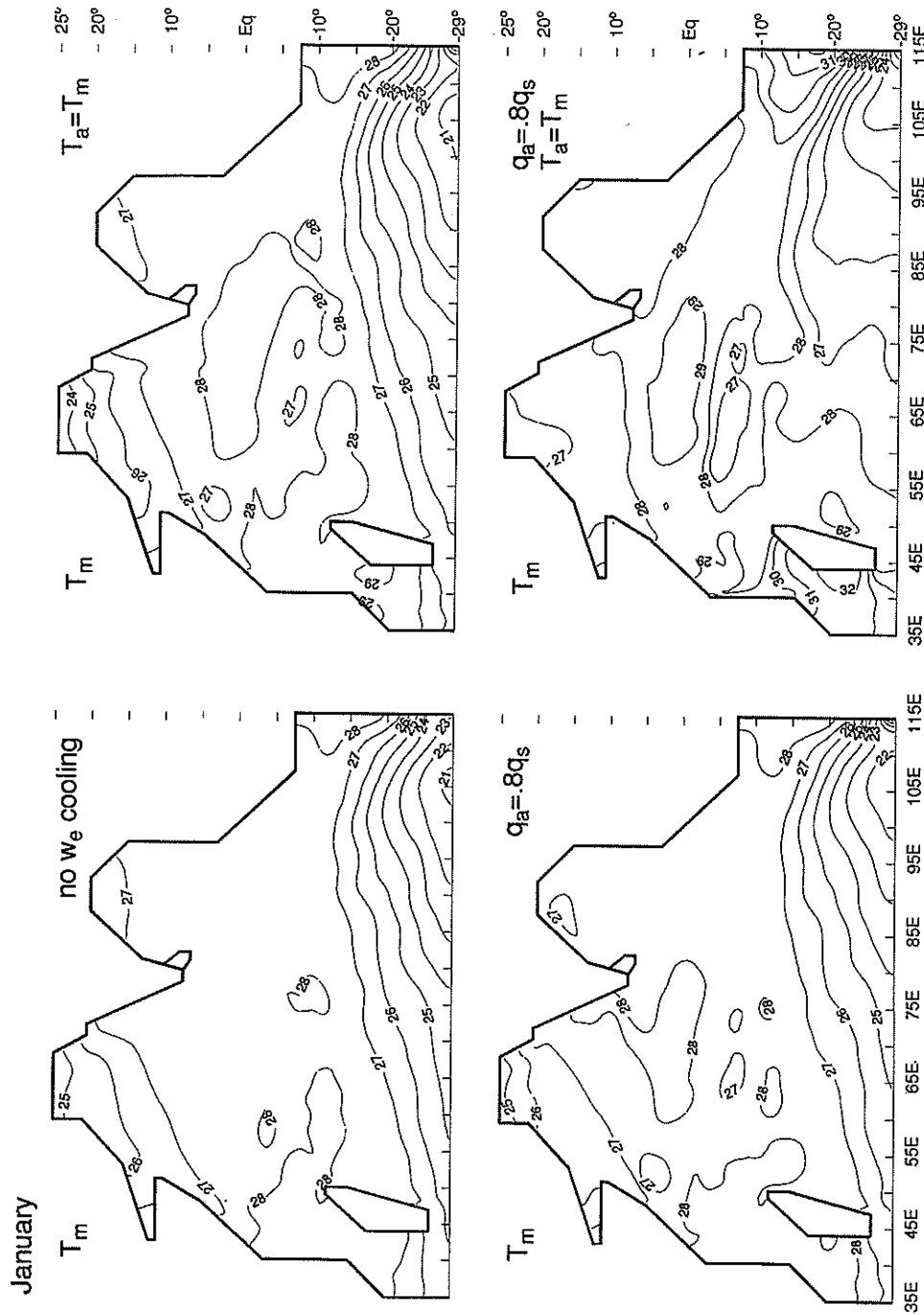


Fig. 10b. As in Fig. 10a, except during January. Compare the plots to the corresponding T_m field in Fig. 2e. Without entrainment cooling SST warms by 1°C or more near the northern-ocean boundaries. There is little change when $T_a \neq T_m$, with SST warming only by about 0.5°C near the northern boundaries. When $q_a = 0.8q_s$ SST warms in the northern Arabian Sea by 1.5°C and there is virtually no cooling in the Bay of Bengal. When $T_a = T_m$ and $q_a = q_s$, the ocean warms considerably near the southern boundary, and SST no longer has a relative minimum near 105°E.

Figure 10b shows T_m for the four test cases of Fig. 10a during January. Without entrainment cooling (upper-left panel), SST is essentially unchanged throughout the southern ocean because upwelling is weak and the mixed layer is shallow; however, it is warmer in the northern Arabian Sea by 1.5°C and in the northern Bay of Bengal by 1°C , indicating the importance of wintertime mixed-layer deepening in cooling these regions (upper-right and lower-left panels of Fig. 2e'). With $T_a = T_m$ (upper-right panel) and with $q_a = 0.8q_s$ (lower-left panel) there is little change from the main run, except that T_m warms near the northern boundary of the basin; in the test with $q_a = 0.8q_s$ there is almost no cooling at all in the northern Bay of Bengal, indicating that the flow of dry continental air over the Bay is the dominant cooling process there during the Northeast Monsoon. When $T_a = T_m$ and $q_a = 0.8q_s$ (lower-right panel), virtually all cooling in the northern ocean vanishes and SST warms considerably in the southern ocean as well; as in July, the simultaneous neglect of both processes has a much larger effect than when they are individually neglected.

A time average of the first of equations (12) shows clearly that the structure of \bar{Q} is determined by the oceanic processes of entrainment, advection and diffusion: without these processes \bar{T}_m must adjust to a state of thermal equilibrium in which $\bar{Q} = 0$. Figure 11 shows \bar{Q} without entrainment cooling (upper panel) and without T_m advection (lower panel), and both panels should be compared to the \bar{Q} panel in Fig. 3'.

Without entrainment cooling, there no longer is strong warming in the upwelling regions in the northern ocean and near 5°S , the cooling region in the southeastern ocean intensifies and broadens westward, and the warming in the southeast corner of the basin vanishes. Interestingly, there is now a band of heating extending along the equator, rather like those in most of the estimates of observed \bar{Q} . Finally, in this test the net integral of \bar{Q} over the basin is *negative* ($-3.0 \times 10^{14}\text{W}$), demonstrating that the net heating in the main run ($34.2 \times 10^{14}\text{W}$) is a *direct consequence of upwelling*. Thus, the \bar{Q} field is very sensitive to the presence or absence of entrainment cooling. It is therefore likely to be sensitive to the model parameters that control the strength of this process (like ΔT and T_e), but we have not explored these dependencies in this study.

Without T_m advection, regions of positive \bar{Q} in the northern ocean are more confined to upwelling regions. In the southern ocean, the patch of warming northeast of Madagascar in the main run is absent in the test, because there is no advection of cool SST into the region by the strong westward current. Likewise, there are no regions of intensified cooling southeast of Madagascar and in the southwest corner of the basin because of the absence of southward advection of warm SST by the East Madagascar and Agulhas Currents. There is also no cooling in the southeastern ocean because there is no southward advection of warm SST in the Tropical Gyre. Finally, it is noteworthy that any cooling regions (where \bar{Q} is negative) remain in this test at all. Since upwelling can only produce anomalously cool SST and hence regions of positive \bar{Q} , the cooling must result entirely from diffusion. The cooling is particularly strong along the southern boundary; it happens because the boundary condition $T_{my} = 0$ ensures that the mixing term $\kappa_T T_{my}$ is large and positive, which tends to warm SST thereby producing the intensified surface cooling there.

4.3 Dependence on w_d

As noted in Section 2.3, there is no firm observational basis to support our specification of detrainment. For this reason we carried out a sequence of test calculations to explore the sensitivity of solutions to the strength and parameterization of w_d .

When detrainment is weakened, by increasing H_d or t_d in equation (7), h_1 will adjust to a new equilibrium state in which h_1 is thicker throughout the basin. As a consequence, there is less entrainment because it is more difficult for h_1 to shallow to the minimum thickness h_{\min} in upwelling regions and for h_m to deepen to h_1 in entraining regions. The upper panels of Fig. 12 show h_1 and

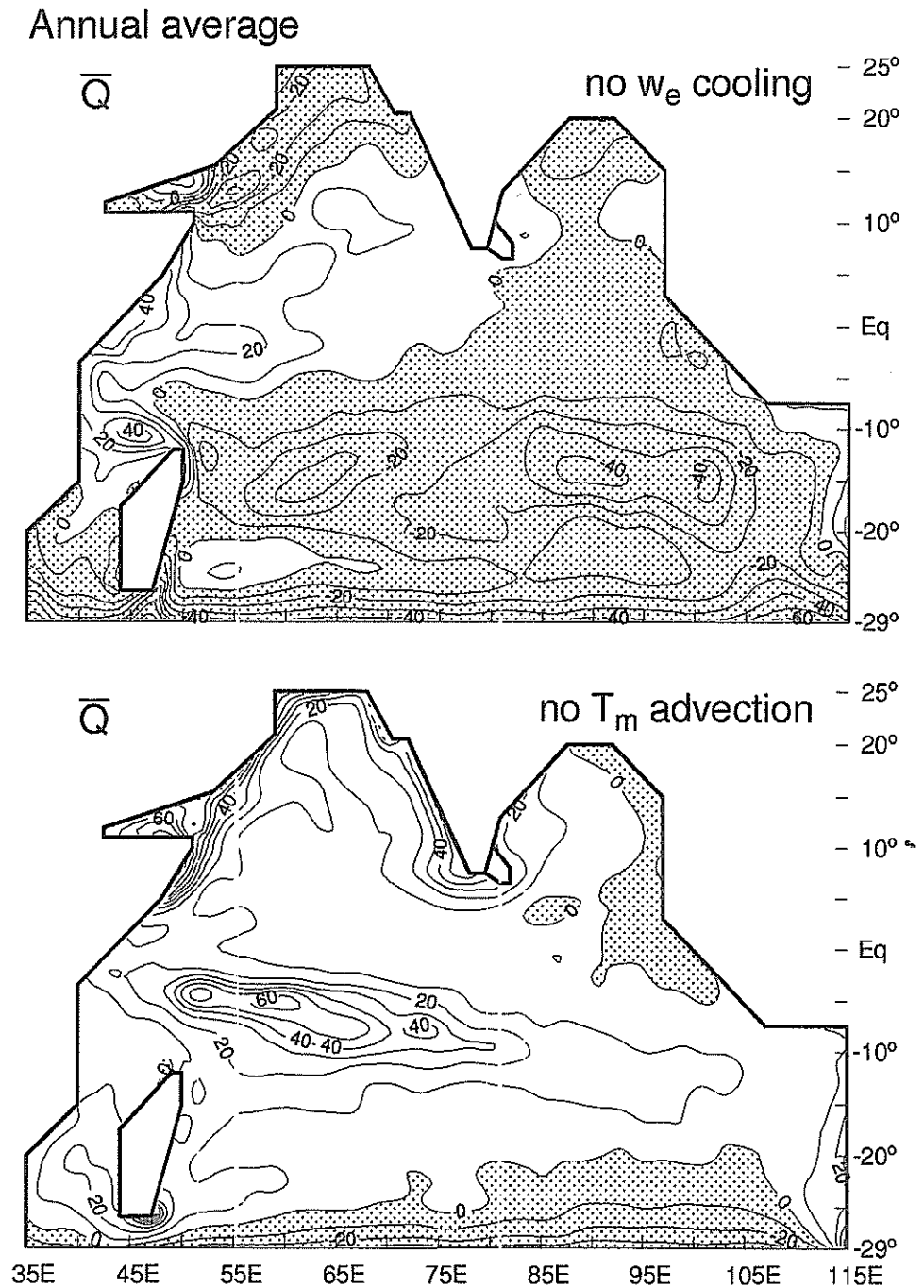


Fig.11. Horizontal distributions of annual-mean, surface heat flux \bar{Q} for two test cases: without entrainment cooling (left panel) and without T_m advection (right panel). The contour interval is 10 W m^{-2} and regions of negative \bar{Q} are shaded. In contrast to the main run (Fig.3'), without entrainment cooling there is a net surface cooling over the basin. Without temperature advection there is no cooling associated with the Agulhas and East Madagascar Currents or in the southeastern ocean, and there is no warming northwest of Madagascar.

\bar{w}_e when H_d is increased to 150m, and these tendencies are apparent (contrast the two panels to their counterparts in Figs 3 and 3'). The \bar{w}_e field shows that there is still a region of strong upwelling off Somalia, with a *well-defined wedge shape* near 5°N. In contrast, there is no upwelling off India because h_1 never reaches h_{\min} . Likewise, there is also no upwelling off Arabia, the weak positive values of w_e there resulting from wintertime entrainment. Figure 13 shows meridional profiles for this test that are analogous to those in Fig. 4. The shape of the profiles demonstrates that the Tropical and Cross-Equatorial Cells still exist, but they are weaker by about a factor of 2. Similar changes occur for other choices of H_d , their magnitude being directly related to the increase in H_d .

To illustrate why \bar{w}_e in Fig. 12 has such a distinctive wedge shape, the lower panels of Fig. 12 show v_1' and T_m in July. In contrast to the main run (Fig. 2b) and in better agreement with the observations, the Southern Gyre is centered farther to the south near 1°N, the Great Whirl spins up strongly and cold SST is confined to the coastal region between these two gyres. This double-gyre system moves slowly northwestward throughout the Southwest Monsoon, with the cold wedge located near 7°N in August, and it collapses in October. It is noteworthy that the strength of w_d has such a great influence on the dynamics of gyre formation and movement. This sensitivity probably occurs because of the effect of w_d on the relative thicknesses of the two layers: with a thicker upper layer, the northward propagation speed of the Southern Gyre along the Somali coast is less, thereby allowing the Great Whirl more time to spin up.

We also obtained solutions for two alternate parameterizations of w_d . One formulation is

$$w_d = - \frac{(H_d - h_1)^2}{t_d H_d} \theta(h_1 - H_d), \quad (13a)$$

just (7) without the factor $Q\theta(Q)/Q_0$. With $t_d=180$ days and $H_d=65$ m, the resulting solution is quite similar to the main run except that there is somewhat more detrainment in the eastern equatorial ocean, a region where \bar{h}_1 is thick (as in the \bar{h}_1 panel of Fig. 3) and the magnitude of Q is small throughout the year. [We note here that, although parameterization (13a) works well in this case, it allows too much detrainment in the other equatorial oceans, which are forced by easterly trades (McCREARY and YU, 1992; McCREARY and LU, 1993).] The other parameterization is

$$w_d = - \frac{(H_f - h_f)^2}{t_d H_f} \theta(h_f - H_f), \quad (13b)$$

which states that there is detrainment only when the fossil layer is thicker than a specified amount H_f . This formulation is physically reasonable since we expect the bottom of the upper layer to be able to erode away only when there is a fossil layer that separates the bottom from active mixing. It acts very much like w_d in (7), since a thick fossil layer tends to be present wherever Q is significantly positive. Indeed, with $H_f=30$ m (so that $H_f+h_{\min}=H_d=65$ m) the solution is virtually unchanged from the main run.

4.4 The effect of throughflow

To explore the influence of the Pacific-Ocean throughflow, we specified a southward upper-layer current across the Indonesian boundary segment, $109^\circ\text{E} \leq x < 112^\circ\text{E}$, $y=7.5^\circ\text{S}$, by replacing the closed condition on v_1 with the open condition $v_1 = -V/(h_1 L)$, where $V=10\text{Sv}$ and $L=3^\circ$. Figures 14 and 14' illustrate the changes caused by the throughflow, showing annual-mean difference fields between the test with throughflow and the main run. We note here that they are remarkably similar to analogous difference fields in the global GCM solutions of HIRST and GODFREY (1993, see their Fig. 14), and are also consistent with the linear solutions of KUNDU and McCREARY (1986).

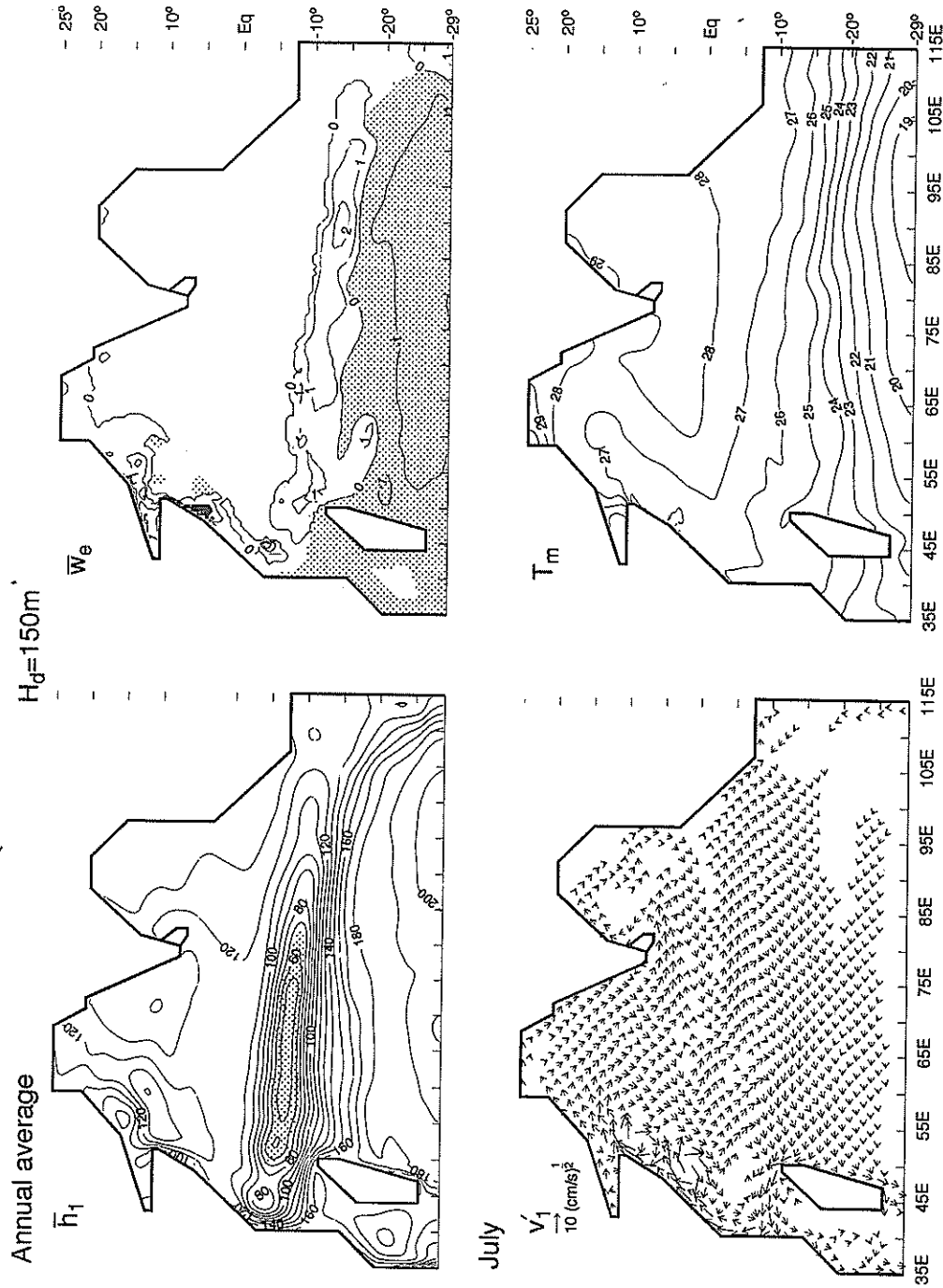


Fig. 12. Horizontal distributions of the annual-mean fields, \bar{h}_1 and \bar{w}_e (upper panels) and the v_1 and T_m fields in July (lower panels) for the test calculation with $H_d=150\text{m}$. Contour intervals for \bar{h}_1 , \bar{w}_e and T_m are 10m , 10^{-4}cm s^{-1} and 1°C , respectively, and current arrows are of the vector field $\mathbf{v}' = \mathbf{v}/v_1^{1/2}$. The near-zero contours and shading of \bar{w}_e are as described in Fig. 2b'. Compare the fields to their counterparts in Figs 3, 3' and 2b. The h_1 field is deeper throughout the basin except in the upwelling regions off Somalia and south of the equator. The w_e field is everywhere weaker than in the main run, and there is no upwelling off Arabia and India. There is a well-developed double-gyre system along the Somali coast in July, and v_1 and T_m are similar to the main run elsewhere in the basin.

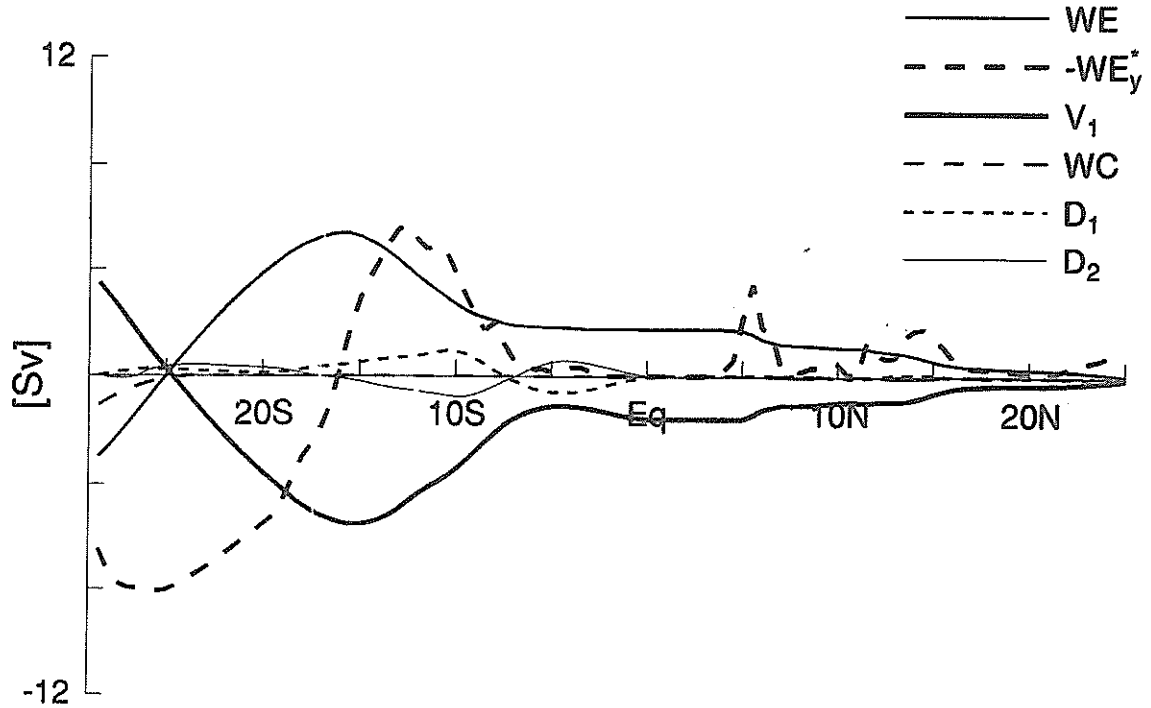


Fig.13. As in Fig.4, except for a test case with $H_d=150\text{m}$. The shapes of the profiles show that the Tropical and Cross-Equatorial Cells still exist. Their strengths are about half of their values in the main run.

The total transport difference field, $\Delta(\overline{h_1 v_1} + \overline{h_2 v_2}) \equiv \Delta V$ (upper-left panel), shows that nearly all of the throughflow moves directly westward across the interior ocean, bends southward at the African coast, and eventually leaves the basin in the Agulhas Current. To understand why this is so, consider the steady-state version of equations (2) without the momentum-flux divergences $\nabla \cdot (\overline{v_i h_i v_i})$, the mixing terms $k_h \nabla^2 h_i$, and the artificial terms, w_e and $\gamma h_i u_i$. It follows that

$$\beta \Psi_x - \nu \nabla^4 \Psi = 0, \quad (14)$$

where Ψ is the transport streamfunction defined by $\Delta(h_1 v_1 + h_2 v_2) = \Psi_x$ and $\Delta(h_1 u_1 + h_2 u_2) = -\Psi_y$. Solutions to this well-known equation are forced by the inflow condition, which specifies Ψ everywhere along the eastern boundary. In the interior ocean the balance is approximately $\Psi_x = 0$ because the influence of mixing is weak, and hence the interior currents are necessarily primarily zonal; the mixing acts to broaden the zonal jet to the west and to allow weak countercurrents on either side. In the western-boundary region the structure of the flow field is a MUNK (1950) layer. The dynamics of the ΔV field in Fig.14 are clearly largely determined by (14).

There are also interesting shear-flow circulations for which $\Delta V = 0$, that are closely related to the structure of $\Delta \overline{h_1}$ (which measures current shear). Because the throughflow adjusts to geostrophic balance and is confined to the upper layer, $\Delta \overline{h_1}$ increases by almost 60m across the inflow region. This increase spreads southward along the Australian coast via Kelvin waves and westward into the ocean interior via Rossby waves, and vanishes in the interior ocean as a result of detrainment (note that $\Delta \overline{h_1}$ quickly approaches zero wherever $\overline{w_e} < 0$ in Fig.3'). The upper-layer shear flow circulates anticyclonically about the region of positive $\Delta \overline{h_1}$ [flowing to the left of $-\nabla(\Delta \overline{h_1})$], and the lower-layer shear flow circulates in the opposite sense. The westward interior

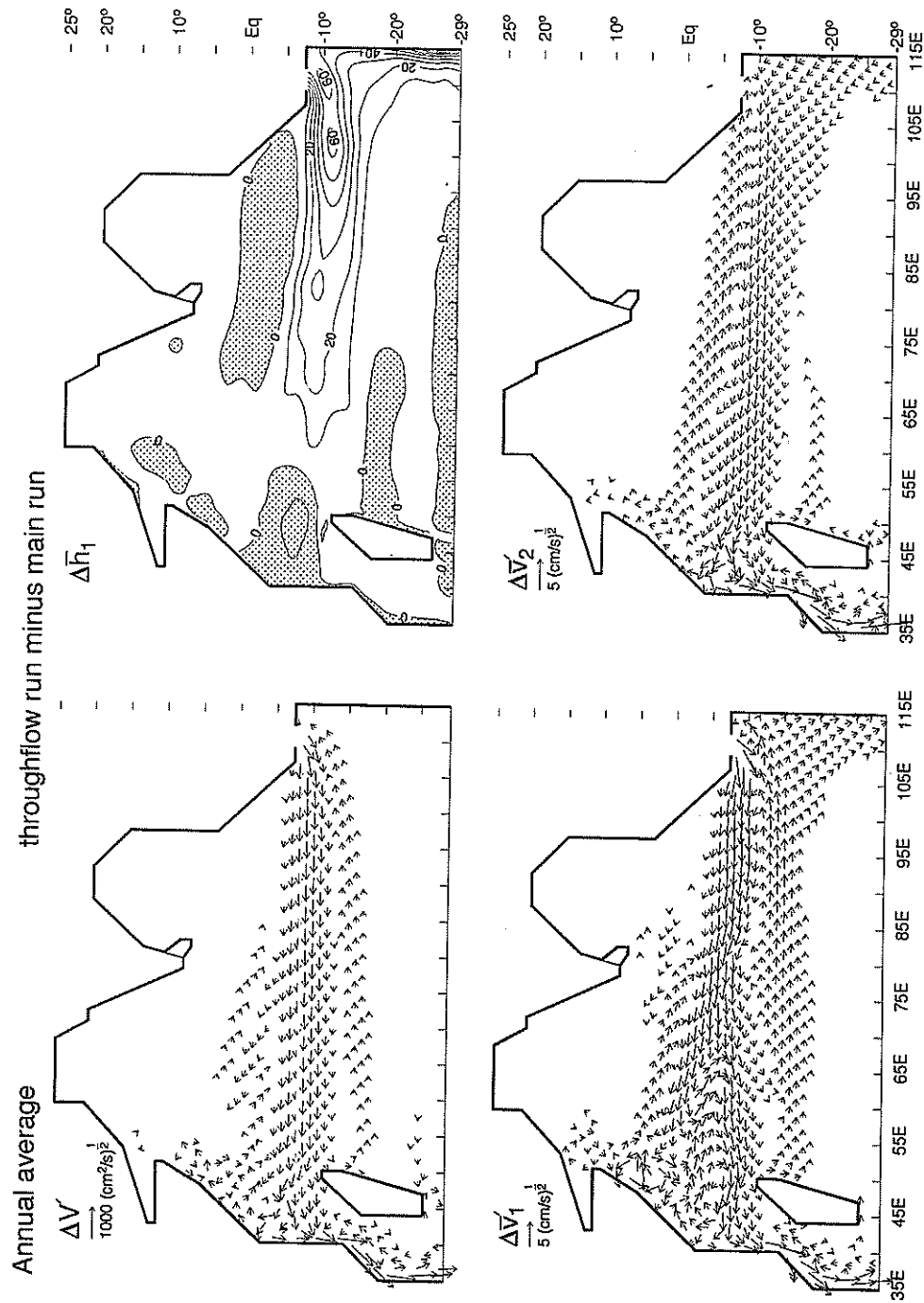


Fig. 14. Horizontal distributions of annual-mean difference fields that illustrate the effect of Pacific-Ocean throughflow. The fields are obtained by subtracting the main-run fields from the corresponding fields in a test calculation with the throughflow. The contour interval for Δh_1 is 10m, and current and transport arrows are of the vector field $\Delta \vec{V} = \Delta \vec{V} / |\Delta \vec{V}|^{1/2}$. The transport field $\Delta \vec{V}$ consists of a westward current across the interior ocean, and a southward flow out of the basin in the Agulhas Current. There are also shear-flow circulations, that are closely tied to the structure of Δh_1 . One of them is the flow field off Australia.

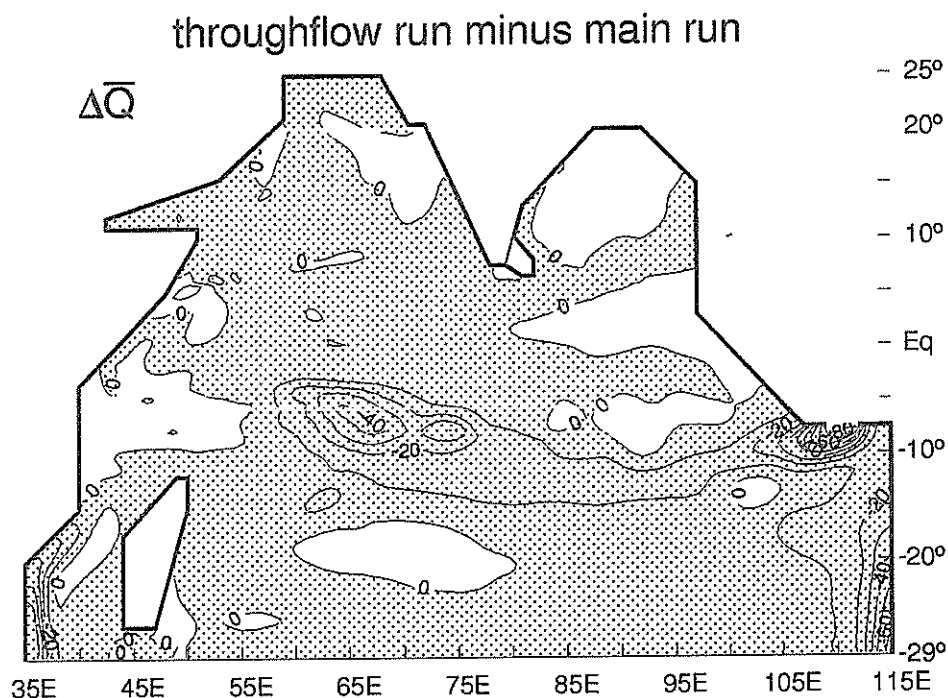


Fig. 14'. As in Fig. 14, except for the difference field $\Delta \bar{Q}$. The contour interval is 10 W m^{-2} . The regions of intensified cooling near Indonesia, along Australia and in the Agulhas Current result from anomalous advection. The cooling in the interior ocean results from weakened entrainment.

current shows the effects of this circulation, being shifted to the north in the upper layer and to the south in the lower layer. The flow field along the coast of Australia is entirely a shear-flow circulation, and does not appear in $\Delta \bar{V}$ at all. The rather complicated $\Delta \bar{V}_1$ field in the western ocean near 5°S is a shear flow associated with the region of low h_1 ; just how this low- h_1 region is generated by the throughflow is unclear.

Figure 14' shows the $\Delta \bar{Q}$ field for this test calculation. It shows that the throughflow strengthens cooling along the Australian coast, across the interior ocean in a band centered about 12°S , and along the western boundary south of 15°S . The magnitude of the cooling is significant, with the net input over the Indian Ocean decreasing to $1.5 \times 10^{14} \text{ W}$ (as compared to $3.2 \times 10^{14} \text{ W}$ for the main run). Part of the cooling results from anomalous advection: the regions adjacent to Indonesia, in the model's Agulhas Current and along Australia. In contrast, cooling in the interior band (and also along Australia) is caused by the anomalous deepening of h_1 : the deepening weakens cooling by entrainment, thereby requiring a compensating increase in surface cooling.

5. SUMMARY AND DISCUSSION

An important part of this research is to identify instances of remotely forced circulations in the solution, and there are three such examples along the Somali coast. During the spring, the model Somali Undercurrent flows southward from about 5°N to the equator (Fig.2b'), and it is largely remotely forced from the Bay of Bengal by a Rossby wave radiating off the west coast of India (Fig.6c). During the fall, a second southward Somali Undercurrent is present from 11°N to 3°N that is predominantly forced by winds during the previous Southwest Monsoon (Figs 2d' and 2e'); it weakens in February and reverses in March in response to local forcing by negative wind curl (Fig.7c). There is a surface countercurrent in November north of 5°N that flows northeastward against the winds; it is the western-boundary current associated with a band of high h_1 in the central Arabian Sea that was generated during the Southwest Monsoon (Fig.2d). This countercurrent weakens in January in response to the strengthened northeasterly winds (Fig.2e), but reappears in March as the Northeast Monsoon weakens (Fig.2f), at which time it is also strengthened locally by negative wind curl (Fig.7c). Another interesting flow in the region is a northward cross-equatorial undercurrent present during January and February (Fig.2e'), but we were not able to determine its cause.

The currents along the west coast of India are strongly affected by remote forcing from the Bay of Bengal throughout the year. From April through October, h_1 is shallow along the coast, the surface current is southward, and there is a northward coastal undercurrent (Figs 2a, 2a', 2b, 2b' and 3c). The local, alongshore wind is upwelling favorable at this time and it does help to intensify this circulation; however, the coastal currents still persist strongly in a test calculation without Arabian-Sea winds (Fig.6a), and they are much weaker in a test without Bay-of-Bengal winds (Fig.8a), demonstrating the dynamical importance of remote forcing by the Bay-of-Bengal winds. From October through February, h_1 deepens along the west coast, the surface current is northward, and there is a southward undercurrent (Figs 2d, 2d', 2e, 2e' and 2f). The local wind field is too weak to force these changes, and Johannessen *et al* (1981) and SHETYE *et al* (1991a) proposed thermohaline driving mechanisms to account for them. In our solution, however, the reversal is entirely remotely forced by the collapse of the Southwest-Monsoon winds in the Bay of Bengal, as confirmed by the test calculations noted above (Figs 6b and 8b).

In contrast, the coastal currents in the Bay of Bengal appear to be predominantly forced by winds within the Bay throughout the year. Remote forcing from the equator, a process emphasized by POTEMRA *et al* (1991) and YU *et al* (1992), does influence the flow field in our solution, primarily along the eastern boundary of the Bay during the spring (Figs 8c and 9c), but only moderately along the east coast of India during the Southwest Monsoon (see the discussion of Figs 9a and 9b). In January, the surface current along the east coast of India north of 17°N begins to flow to the northeast (Fig.2e), and by March there is northeastward flow everywhere along the east coast (Fig.2f). The local alongshore winds are just beginning to become southwesterly in March, and so local forcing is not likely to be a dominant forcing mechanism at this time. One possible cause is the effect of alongshore winds along the northeast and northwest boundaries of the Bay; another possibility is remote forcing by negative wind curl in the western Bay. With the advent of upwelling-favorable winds during the Southwest Monsoon, h_1 develops an upward tilt toward the south along the coast, and the northeastward current strengthens (Figs 2a and 2b). From September through January, there is southward flow along the east coast with its peak strength in November, well before the peak of the Northwest Monsoon. This current is generated by the collapse of the Southwest-Monsoon winds; as a consequence, the upward tilt of h_1 vanishes, h_1 deepens everywhere along the east coast via Kelvin-wave propagation, and a geostrophically balanced

southward current develops (Figs 2c and 2d). This deepening also propagates around the tip of India via Kelvin waves to generate the northward current along the west coast of India.

The zonal currents just north of the equator are affected by several processes. During the Southwest Monsoon a strong eastward current develops south of India that flows across the southern Bay of Bengal at 5°N , the model Indian Monsoon Current (Figs 2b and 2c). South of India the current is primarily locally forced by the wind-curl pattern which tends to shallow h_1 north of 4°N and to deepen it to the south (Section 3.1.1 and Fig. 2a; Fig. 8a). In the central Bay of Bengal it is remotely forced from the equator by a packet of reflected Rossby waves (Fig. 9a). During the Northeast Monsoon there is an eastward flow nearly everywhere north of the equator, the model North Equatorial Current (Figs 2e and 2f). This current is generated by local Ekman pumping in the southern Bay of Bengal (Fig. 8b), and by the radiation of a downwelling Rossby wave from the tip of India into the Arabian Sea (Fig. 2e). It is also enhanced near the equator by the radiation of an upwelling Kelvin wave (Figs 2e and 2e').

There are two prominent surges of the equatorial currents in response to changes in the zonal component of the wind stress there. During the Northeast Monsoon, the equatorial winds have an easterly component that directly forces a westward surface equatorial current, and excites an upwelling Kelvin wave that reflects from the eastern boundary as a packet of Rossby waves (Figs 2e, 2e' and 2f; Fig. 9c). The equatorial winds reverse to have a westerly component during the transition to the Southwest Monsoon, generating a swift eastward current (the spring Wyrtki jet), as well as a downwelling equatorial Kelvin wave and reflected Rossby-wave packet (compare Figs 2f and 2a). The only significant instances in the Bay of Bengal of remote forcing from the equator arise from the reflection of these two surges.

The circulation in the southern Indian Ocean is driven largely by wind curl over the interior ocean. It consists primarily of a Tropical Gyre that remains relatively unchanged throughout the year, except for its northern branch (the Equatorial Countercurrent) which is affected by the highly variable, near-equatorial zonal wind field. This circulation is modified when throughflow from the Pacific Ocean is included. The net transport ΔV of the throughflow flows directly westward across the interior ocean and southward out of the basin in the Agulhas Current (Fig. 14). There are also secondary, shear-flow circulations induced by the throughflow for which $\Delta V=0$. One such circulation is a poleward surface current and equatorward undercurrent along the Australian coast, but these currents are too weak to provide an adequate explanation for the observed Leeuwin Current system.

Although the surface currents present in the main run generally compare favorably with the observations, there are several discrepancies that point toward deficiencies in the model physics. The largest differences occur in the near-equatorial ocean. During the northern-hemisphere summer, ship-drift observations show eastward flow everywhere across the basin near 5°N (the Indian Monsoon Current) and weak flow on and just south of the equator; in contrast, the main run has southward flow across the equator in the central Arabian Sea, an eastward current south of the equator in the eastern basin (the Equatorial Countercurrent), and a westward equatorial current in the western basin (Figs 2b and 2c). During the fall, the main run fails to reproduce a strong Wyrtki jet, particularly in the western basin (Fig. 2d); it also fails to reproduce a summertime deepening of the thermocline in the *western* tropical Indian Ocean (Fig. 2c), a necessary precondition for the fall jet according to QUADFASSEL (1982).

A possible cause for these differences is the lack of vertical shear between the mixed and fossil layers, which may underestimate the importance of wind-drift flows confined to the mixed layer. In support of this idea, HASTENRATH and GREISCHAR (1991) computed geostrophic currents relative to 400db from historical data and Ekman currents from surface wind data for the tropical

Indian Ocean. They concluded that the Equatorial Countercurrent is mainly an *eastward* geostrophic flow that during the summer is virtually eliminated by *westward* Ekman drift; similarly, the Indian Monsoon Current in the Arabian Sea is primarily an eastward Ekman drift. Another possible cause is the limited vertical resolution of the $2\frac{1}{2}$ -layer model, which does not allow sufficient vertical propagation of Rossby waves; in a system with greater resolution, the first-meridional-mode, equatorially trapped Rossby wave, so prominent in Figs 2b, 2c and 2d, should propagate downward out of the surface layer (MCCREARY, 1984; MOORE and MCCREARY, 1990; JENSEN, 1991; KESSLER and MCCREARY, 1992). A third possibility, external to the model physics, is that the near-equatorial wind field is incorrect. To explore this possibility, we carried out a test calculation using the wind stress field obtained by applying a constant drag coefficient of .0028 to the monthly winds of RAO *et al* (1989, 1991). The resulting stresses were considerably stronger than those of HELLERMAN and ROSENSTEIN (1983) off Somalia, but they were *weaker* near the equator by as much as $.1-.2 \text{ dyn cm}^{-2}$. As a consequence, there was no fall Wyrtki jet at all in the test solution, with westward flow everywhere along the equator in October and November! Similar large differences between solutions using different wind products have recently been reported in other studies (REVERDIN and CANE, 1984; ANDERSON and CARRINGTON, 1993; KINDLE, personal communication).

Modelled and observed SST compare well throughout the year. To explore why this is so, the effects of various terms in the T_m -equation were isolated in a series of test runs (Section 4.3). There is little effect on T_m in tests with $Q_s=0$ and when Q_r is replaced by the spatially smoothed field \bar{Q} . In a test without temperature advection, the most obvious effect on T_m occurs near western boundaries because isotherms are not shifted by the swift currents there; the \bar{Q} field is also affected in this test, with the lack of warm currents resulting in regions of more positive \bar{Q} and vice versa (compare the lower panel of Fig. 11 with the lower-right panel of Fig. 3'). Without entrainment cooling, T_m warms considerably in the strong upwelling regions (upper-left panel of Fig. 10a); as a consequence, the net heat input into the Indian Ocean is *negative*, whereas it is *positive* in the main run (upper panel of Fig. 11 and lower-right panel of Fig. 3'), demonstrating that the net heating in the main run is caused by upwelling. In the tests without entrainment cooling, with $T_a=T_m$, and with $q_a=0.8q_s$, T_m warms by about 1°C near the northern and southern boundaries of the basin in their respective winters. It follows that three processes help to cool SST during the winter: mixed-layer deepening driven by convective mixing, the increase of C_L and Q_L resulting from T_a , and the increase of Q_L caused by lower specific humidity q_a . There is no cooling in the northern Bay of Bengal in the test with $q_a=0.8q_s$, showing that the flow of dry air off the Asian continent during the Northwest Monsoon is the primary cooling process there. Model SST is degraded considerably in the southern Indian Ocean in a test with *both* $T_a=T_m$ and $q_a=0.8q_s$, suggesting that one or the other of the external forcing fields, T_a and q_a , must be included to simulate SST accurately.

The major thermodynamic limitation of the model is that the heat input through the surface is removed primarily by the artificial cooling terms, Q_2 and $w_e T_2$ (Figs 3' and 5), not by southward advection of warm tropical waters. This deficiency is likely a consequence of the basin not extending far enough to the south. Another limitation is that T_m does not cool sufficiently in the northern Bay of Bengal during the winter (Fig. 2e; Hastenrath and Lamb, 1979). A possible cause for this discrepancy is that the mixed layer is too thick in the northern Bay, so that it is difficult to cool. There is little indication of this deepening in the real Bay of Bengal, probably because there is a surface layer of fresh water that inhibits entrainment.

The annual-mean circulation (Figs 3 and 3') has two meridional circulation cells (Fig. 4). In both cells nearly all of the water detrains from the upper layer (subducts) in the southern ocean south of 14°S , whereas in the Cross-Equatorial Cell it upwells in the northern ocean primarily along the

coasts of Somalia, Arabia and India. The strength of the cells is directly related to the magnitude of the subduction rate w_d [equation (7)]. For example, when H_d is increased to 150m, h_1 increases, the magnitude of \bar{w}_e decreases, and the strength of the circulation cells weakens by a factor of two (Figs 12 and 13). Interestingly, in this test the Southern Gyre moves northward more slowly, there is a well-developed Great Whirl, and cold SST is confined to a wedge-shaped region between the gyres; thus, the strength of detrainment has a large effect on Somali Current dynamics. The structure of the cells is not particularly sensitive to the two alternate parameterizations of w_d in equations (13a) and (13b).

In conclusion, we have developed a model of Indian-Ocean circulation that is sophisticated enough to simulate the near-surface current and SST fields quite well throughout the year. At the same time, the system is simple enough to be able to isolate the important processes at work in it. We have been able to determine the relative importance of local and remote forcing by the wind, to investigate the thermodynamic processes that maintain model SST, and to study the mixed-layer processes that allow the existence of meridional circulation cells. Discrepancies between the observed and modelled fields point toward several model deficiencies. These deficiencies are: the lack of shear between the mixed and fossil layers, limited vertical resolution, limited basin size, and the absence of salinity effects. We plan to improve the model to overcome these limitations in the next several years.

6. ACKNOWLEDGEMENTS

This work was sponsored by ONR contract N00014-90-J-1054, and by NSF grants OCE-89-12015 and OCE-88-17026. Robert Molinari was supported in part by grant R1A, 8R1AC1 from NOAA's Office of Climate and Atmospheric Research. During the course of this research, Julian McCreary visited the National Institute of Oceanography in Goa, India; our discussion of the circulations in the Bay of Bengal and along the Indian coast was enhanced due to his interaction with scientists there (notably L.V.G. Rao, M.K. Antony, V.S.N. Murty, M.T. Babu, and especially Satish Shetye). The comments of Stuart Godfrey on a draft of the manuscript, particularly concerning the model's surface heat-flux field, are greatly appreciated. As always, this research would not have been possible without the programming assistance of Kevin Kohler.

7. REFERENCES

- ANDERSON, D.L.T. and D.J. CARRINGTON (1993) Modelling interannual variability in the Indian Ocean using momentum fluxes from the UKMO and ECMWF operational weather analyses. *Journal of Geophysical Research*, (in press).
- ANDERSON, D.L.T., D.J. CARRINGTON, R. CORRY and C. GORDON (1991) Modelling the variability of the Somali Current. *Journal of Marine Research*, **49**, 659-696.
- ANTONY, M.K. (1990) Northward undercurrent along west coast of India during upwelling - Some inferences. *Indian Journal of Marine Science*, **19**, 95-101.
- ANTONY, M.K. and A.S. UNNIKRISHNAN (1992) On an upwelling front, propagation of upwelling and vertical velocity in the eastern Arabian Sea during monsoon, 1987. In: *PORSEC-92 in Okinawa: Conference for Pacific Ocean Environments and Probing Proceedings Vol.1*, 527-532.
- ANTONY, M.K., S.S.C. SHENOI, V.V.G. KRISHNA, C.S. MURTY, D.P. RAO, V.S.N. MURTY and J.S. SASTRY (1992) Seasonally reversing current bands across 15°N in the Arabian Sea and their implications. *Indian Journal of Marine Science*, **21**, 46-51.
- BAUER, S., G.L. HITCHCOCK and D.B. OLSON (1991) Influence of monsoonally-forced Ekman Dynamics upon surface layer depth and plankton biomass distribution in the Arabian Sea. *Deep-Sea Research*, **38**(5), 531-553.
- BRUCE, J.G. (1973) Large-scale variations of the Somali Current during the southwest monsoon, 1970. *Deep-Sea Research*, **20**, 837-846.

- BUNKER, A.E. (1976) Computations of surface energy flux and annual air-sea interaction cycles of the North Atlantic Indian Ocean. *Monthly Weather Review*, **104**, 1122-1140.
- CUTLER, A.N. and J.C. SWALLOW (1984) Surface currents of the Indian Ocean (To 25°S, 100°E). *IOS Technical Report*, 187pp.
- DUING, W. and A. LEETMAA (1980) Arabian Sea cooling: A preliminary heat budget. *Journal of Physical Oceanography*, **10**, 307-312.
- ESBENSEN, S.K. and Y. KUSHMIR (1981) The heat budget of the global ocean: An atlas based on estimates from surface marine observations. *Climatic Research Institute Report*. No.29, Oregon State University, Corvallis.
- EVANS, R.M. and O.B. BROWN (1981) Propagation of thermal fronts in the Somali Current system. *Deep-Sea Research*, **28**, 521-527.
- FINE, R.A. (1985) Direct evidence for throughflow from the Pacific into the Indian Ocean using tritium data. *Nature*, **315**, 478-480.
- GODFREY, J.S. (1989) A Sverdrup model of the depth-independent flow for the world ocean allowing for island circulations. *Geophysical and Astrophysical Fluid Mechanics*, **45**, 89-112.
- GODFREY, J.S. and K.R. RIDGWAY (1985) The large scale environment of the poleward flowing Leeuwin Current, western Australia: Longshore steric height gradients, wind stresses and geostrophic flow. *Journal of Physical Oceanography*, **15**, 481-495.
- GODFREY, J.S. and A.J. WEAVER (1991) Is the Leeuwin Current driven by Pacific heating and winds? *Progress in Oceanography*, **27**, 225-272.
- HASTENRATH, S. (1982) On meridional heat transports in the world ocean. *Journal of Physical Oceanography*, **12**, 922-927.
- HASTENRATH, S. and L. GREISCHAR (1989) *Climatic Atlas of the Indian Ocean, Part III: Upper-ocean structure*. University of Wisconsin Press, Madison, 273pp.
- HASTENRATH, S. and L. GREISCHAR (1991) The monsoonal current regimes of the tropical Indian Ocean: observed surface flow fields and their geostrophic and wind-driven components. *Journal of Geophysical Research*, **96**(C7), 12,619-12,633.
- HASTENRATH, S. and P.J. LAMB (1979) *Climatic Atlas of the Indian Ocean*. University of Wisconsin Press, Madison.
- HELLERMAN, S. and M. ROSENSTEIN (1983) Normal monthly wind stress over the world ocean with error estimates. *Journal of Physical Oceanography*, **13**, 1093-1104.
- HIRST, A.C. and J.S. GODFREY (1993) The role of the Indonesian Throughflow in a global ocean GCM. *Journal of Physical Oceanography*, **23**, 1057-1086.
- HSUING, J. (1985) Estimates of global oceanic meridional heat transport. *Journal of Physical Oceanography*, **15**, 1405-1413.
- JENSEN, T.G. (1991) Modelling the seasonal undercurrents in the Somali Current system. *Journal of Geophysical Research*, **96**, 22,151-22,167.
- JOHANNESSEN, O.M., G. SUBBARAJU and J. BLINDHEIM (1982) Seasonal variation of the oceanographic conditions off the southwest coast of India during 1971-1975. *Fiskeridirektoratets Skrifter. Serie Havundersokelser*, **18**, 247-261.
- KESSLER, W. and J.P. McCREARY (1992) The annual wind-driven Rossby wave in the subthermocline equatorial Pacific. *Journal of Physical Oceanography*, **23**(6), 1192-1207.
- KINDLE, J.C. and J.D. THOMPSON (1989) The 26- and 50-day oscillations in the western Indian Ocean: Model results. *Journal of Geophysical Research*, **94**(C4), 4721-4736.
- KINDLE, J.C., H.E. HURLBURT, E.J. METZGER and A. WALLCRAFT (1989) On the seasonal and interannual variability of the Pacific to Indian Ocean throughflow. In: *Western Pacific International Meeting and Workshop on TOGA COARE, held at Noumea, New Caledonia, May 24-30, 1989: Proceedings*. J. PICAUT, R. LUKAS and T. DELCROIX, editors, Centre ORSTOM de Noumea, 343-354.
- KNOX, R.A. (1976) On a long series of measurements of Indian Ocean equatorial currents near Addu Atoll. *Deep-Sea Research*, **23**, 211-221.
- KRAUX, E.B. and J.S. TURNER (1967) A one-dimensional model of the seasonal thermocline. II: The general theory and its consequences. *Tellus*, **119**, 98-106.
- KUNDU, P.K. and J.P. McCREARY (1986) On the dynamics of the throughflow from the Pacific to the Indian Ocean. *Journal of Physical Oceanography*, **16**, 2191-2198.
- LEETMAA, A., D.R. QUADFASSEL and D. WILSON (1982) Development of the flow field during the onset of the Somali Current, 1979. *Journal of Physical Oceanography*, **12**, 1325-1342.

- LEGECKIS, R. (1987) Satellite observations of a western boundary current in the Bay of Bengal. *Journal of Geophysical Research*, **92**(C12), 12,974-12,978.
- LUTHER, M.E. and J.J. O'BRIEN (1985) Modelling the variability of the Somali Current. In: *Coherent Structures in Geophysical Turbulence*, J.C. NIHOUL, editor, Elsevier, New York. 405-436.
- LUYTEN, J.R. and D.H. ROEMMICH (1982) Equatorial currents at semi-annual period in the Indian Ocean. *Journal of Physical Oceanography*, **12**, 406-413.
- MCCREARY, J.P. (1984) Equatorial beams. *Journal of Marine Research*, **42**, 395-430.
- MCCREARY, J.P. and P.K. KUNDU (1988) A numerical investigation of the Somali Current during the Southwest Monsoon. *Journal of Marine Research*, **46**, 25-58.
- MCCREARY, J.P. and P.K. KUNDU (1989) A numerical investigation of sea surface temperature variability in the Arabian Sea. *Journal of Geophysical Research*, **94**, 16,097-16,114.
- MCCREARY, J.P. and P. LU (1993) On the interaction between the subtropical and equatorial ocean circulations: the Subtropical Cell. *Journal of Physical Oceanography*, (in press).
- MCCREARY, J.P. and Z. YU (1992) Equatorial dynamics in a 2½-layer model. *Progress in Oceanography*, **29**, 61-132.
- MCCREARY, J.P., S.R. SHETYE and P.K. KUNDU (1986) Thermohaline forcing of eastern boundary currents: with application to the circulation off the west coast of Australia. *Journal of Marine Research*, **44**, 71-92.
- MCPHADEN, M.J. (1982) Variability in the central equatorial Indian Ocean. Part I: Ocean dynamics. *Journal of Marine Research*, **40**, 157-176.
- MOLINARI, R.L., D. OLSON and G. REVERDIN (1990) Surface current distributions in the tropical Indian Ocean derived from compilations of surface buoy trajectories. *Journal of Geophysical Research*, **95**, 7217-7238.
- MOORE, D.W. and J.P. MCCREARY (1990) Excitation of intermediate-frequency equatorial waves at a western ocean boundary: with application to observations from the Indian Ocean. *Journal of Geophysical Research*, **95**, 5129-5231.
- MUNK, W.H. (1950) On the wind-driven ocean circulation. *Journal of Meteorology*, **7**, 79-93.
- NURSER, A.J.G. and J.C. MARSHALL (1991) On the relationship between subduction rates and diabatic forcing of the mixed layer. *Journal of Physical Oceanography*, **21**, 1793-1802.
- OBERHUBER, J.M. (1988) An atlas based on the "COADS" data set: The budgets of heat, buoyancy and turbulent kinetic energy at the surface of the global ocean. *Max Planck Institut fur Meteorologie Report No. 15*.
- PERIGAUD, C. and P. DELECLUSE (1989) Simulations of dynamic topography in the northwestern Indian Ocean with input of SEASAT altimeter and scatterometer data. *Ocean-Air Interactions*, **1**, 289-309.
- PERIGAUD, C. and P. DELECLUSE (1992) Annual sea level variations in the southern tropical Indian Ocean from GEOSAT and shallow-water simulations. *Journal of Geophysical Research*, **97**, 20169-20178.
- PHILANDER, S.G.H., W.J. HURLIN and A.D. SIEGEL (1987) Simulation of the seasonal cycle of the tropical Pacific Ocean. *Journal of Physical Oceanography*, **16**, 1986-2002.
- POTEMRA, J.T., M.E. LUTHER and J.J. O'BRIEN (1991) The seasonal circulation of the upper ocean in the Bay of Bengal. *Journal of Geophysical Research*, **96**(C7), 12,667-12,683.
- QUADFASSEL, D.R. (1982) Low frequency variability of the 20°C isotherm topography in the western equatorial Indian Ocean. *Journal of Geophysical Research*, **87**(C3), 1990-1996.
- QUADFASSEL, D.R. and F. SCHOTT (1983) Southward subsurface flow below the Somali current. *Journal of Geophysical Research*, **88**(C10), 5973-5979.
- RAO, L.V.G., T. CHERIAN, K.K. VARMA and V.V.R. VARADACHARI (1974) Hydrographical features of the inner shelf waters along the central west coast of India during winter, spring and summer. *Mahasagar - Bulletin of the National Institute of Oceanography*, **7**, 15-26.
- RAO, R.R., R.L. MOLINARI and J.F. FESTA (1989) Evolution of the climatological near-surface thermal structure of the tropical Indian Ocean. Part 1: Description of mean monthly mixed-layer depth and sea-surface temperature, surface current and surface meteorological fields. *Journal of Geophysical Research*, **94**(C8), 10,801-10,815.
- RAO, R.R., R.L. MOLINARI and J.F. FESTA (1991) Surface meteorological and near surface oceanographic atlas of the tropical Indian Ocean. *NOAA Technical Memorandum ERL AOML-69*.
- REVERDIN, G. and M.A. CANE (1984) The near surface equatorial Indian Ocean in 1979. Part I: Linear dynamics. *Journal of Physical Oceanography*, **14**, 1817-1828.
- SCHOTT, F. (1986) Seasonal variation of cross-equatorial flow in the Somali Current. *Journal of Geophysical Research*, **91C**, 10,581-10,584.

- SCHOTT, F. and M. FIEUX (1985) The Somali Current in autumn 1984, before the onset of the northeast monsoon. *Nature*, **315**, 50-52.
- SCHOTT, F. and D.R. QUADFASSEL (1980) Development of the subsurface currents of the northern Somali Current Gyre from March to July 1979. *Science*, **209**, 593-595.
- SCHOTT, F., J.C. SWALLOW and M. FIEUX (1990) The Somali Current at the equator: Annual cycle of currents and transports in the upper 1000m, and connection to neighboring latitudes. *Deep-Sea Research*, **37**, 1825-1848.
- SCHOTT, F., M. FIEUX, J. KINDLE, J. SWALLOW and R. ZANTOPP (1988) The boundary currents east and north of Madagascar. Part 2: Direct measurements and model comparisons. *Journal of Geophysical Research*, **93**, 4963-4974.
- SEMTNER, A.J. and R.M. CHERVIN (1992) Ocean general circulation from a global eddy resolving model *Journal of Geophysical Research*, **97**(C4), 5493-5550.
- SHENOI, S.S.C., A.D. GOUVEIA, S.R. SHETYE and L.V.G. RAO (1992) Satellite observations of the northeast monsoon coastal current. In: *PORSEC-92 in Okinawa: Conference for Pacific Ocean Environments and Probing Proceedings Vol.2*, 796-801.
- SHETYE, S.R. (1984) Seasonal variability of the temperature field off the southwest coast of India. *Proceedings of the Indian Academy of Sciences (Earth and Planetary Sciences)*, **93**(4), 399-411.
- SHETYE, S.R. and S.S.C. SHENOI (1988) The seasonal cycle of surface circulation in the coastal North Indian Ocean. *Proceedings of the Indian Academy of Sciences (Earth and Planetary Sciences)*, **97**, 53-62.
- SHETYE, S.R., A.D. GOUVEIA, S.S.C. SHENOI, D. SUNDAR, G.S. MICHAEL, A.M. ALMEIDA and K. SANTANAM (1990) Hydrography and circulation off the west coast of India during the Southwest Monsoon 1987. *Journal of Marine Research*, **48**, 359-378.
- SHETYE, S.R., A.D. GOUVEIA, S.S.C. SHENOI, G.S. MICHAEL, D. SUNDAR, A.M. ALMEIDA and K. SANTANAM (1991a) The coastal current off western India during northeast monsoon. *Deep-Sea Research*, **38**, 1517-1529.
- SHETYE, S.R., S.S.C. SHENOI, A.D. GOUVEIA, G.S. MICHAEL, D. SUNDAR and G. NAMPOOTHORI (1991b) Wind-driven coastal upwelling along the western boundary of the Bay of Bengal during the Southwest Monsoon. *Continental Shelf Research*, **11**, 1397-1408.
- SHETYE, S.R., A.D. GOUVEIA, S.S.C. SHENOI, D. SUNDAR, G.S. MICHAEL and G. NAMPOOTHORI (1992) The western boundary current of the seasonal subtropical gyre in the Bay of Bengal. *Journal of Geophysical Research*, **98**(C1), 945-954.
- SMITH, R.L. and J.S. BOTTERO (1977) On upwelling in the Arabian Sea. In: *A Voyage of Discovery*, M. ANGEL, editor, Pergamon, New York, 291-304.
- SPRINTALL, J. and M. TOMCZAK (1992) Evidence of the barrier layer in the surface layer of the tropics. *Journal of Geophysical Research*, **97**, 7305-7316.
- SWALLOW, J.C. (1967) The equatorial undercurrent in the western Indian Ocean in 1964. In: *Studies in Tropical Oceanography*, Miami, No. 5, 15-36.
- SWALLOW, J.C., M. FIEUX and F. SCHOTT (1988) The boundary currents east and south of Madagascar. Part 1: Geostrophic currents and transports. *Journal of Geophysical Research*, **93**, 4951-4962.
- SWALLOW, J.C., R.L. MOLINARI, J.G. BRUCE, O.B. BROWN and R.H. EVANS (1983) Development of near-surface flow patterns and water-mass distributions in the Somali Basin in response to the Southwest Monsoon of 1979. *Journal of Physical Oceanography*, **13**, 1398-1415.
- TOOLE, J.M. and M.E. RAYMER (1985) Heat and fresh-water budgets of the Indian Ocean - revisited. *Deep-Sea Research*, **32**, 917-928.
- TSAI, P.T.H., J.J. O'BRIEN and M.E. LUTHER (1992) The 26-day oscillation observed in the satellite SST measurements. *Journal of Geophysical Research*, **XX**, 000-000.
- WOODBURY, K.E., M.E. LUTHER and J.J. O'BRIEN (1989) The wind-driven seasonal circulation in the southern tropical Indian Ocean. *Journal of Geophysical Research*, **94**, 17,985-18,002.
- WOODS, J.D. and W. BARKMANN (1986) A Lagrangian mixed-layer model of Atlantic 18°C water formation. *Nature*, **319**, 574-576.
- WYRTKI, K. (1961) Physical oceanography of the Southeast Asian waters. NAGA Rep.2, Scripps Institution of Oceanography, 195pp.
- WYRTKI, K. (1973) An equatorial jet in the Indian Ocean. *Science*, **181**, 262-264.
- YU, L., J.J. O'BRIEN and J. YANG (1992) On the remote forcing of the circulation in the Bay of Bengal. *Journal of Geophysical Research*, **96**(C11), 20,449-20,454.

ERRATUM

Progress in Oceanography
Volume 31, Number 4, pp. 181-244

A numerical investigation of dynamics, thermodynamics and mixed-layer processes in the
Indian Ocean

JULIAN P. MCCREARY, JR., PIJUSH K. KUNDU and ROBERT L. MOLINARI

1. Page 187, equation (5): The symbol T_3 should be T_e
2. Page 188, second line after equation (8a): The equation $\Delta v = \Delta V$ should be $\Delta v = -\Delta V$
3. Page 191, second line after equation (10): The equation $\rho_i = \bar{\rho} - (1-\alpha)gT_i$ should read $\rho_i = \bar{\rho} (1-\alpha T_i)$
4. Page 191, equation (11): The symbol c_n in the numerator of the fraction should be c_n^2
5. Page 231, third paragraph, sixth line: The quantity $34.2 \times 10^{14}W$ should be $3.2 \times 10^{14}W$
6. Pages 204, 209 and 219 should be replaced by the following pages.

